Supporting Information

Lessons Learnt in Photocatalysis - the Influence of Solvent Polarity and the Photostability of the Photocatalyst

Megan Amy Bryden,[a] Francis Millward,[a] Oliver S. Lee,[a] Lauren Cork,[a] Malte C. Gather,[b] Andreas Steffen[c] and Eli Zysman-Colman[a]*

[a]Organic Semiconductor Centre, EaStCHEM School of Chemistry, University of St Andrews, St Andrews, Fife, U.K., KY16 9ST, Fax: +44-1334 463808; Tel: +44-1334 463826;
E-mail: eli.zysman-colman@st-andrews.ac.uk;
URL: http://www.zysman-colman.com
[b]Humboldt Centre for Nano- and Biophotonics, Department of Chemistry, University of Cologne, Greinstr. 4-6, 50939 Cologne, Germany
[c]Technische Universität Dortumund, Fakultät für Chemie und Chemische Biologie, Anorganische Chemie, Otto-Hahn-Str., 644227, Dortmund, Germany.

Table of Contents

Experimental Section

General Synthetic Procedures. The following starting materials were synthesised according to literature procedures: **[Ru(bpy)₃](PF₆)₂**,[1] **[Ir(ppy)₂(dtbbpy)]PF₆**,[2] **[Ir(dF(CF₃)ppy)₂(dtbbpy)]PF₆**,[3] **[Cu(dmp)(xantphos)]PF₆**,[4] **4CzIPN**,[5] **2CzPN**,[6] **pDTCz-DPmS**[7] and *N*-Cbz-Pro.[8] All other reagents and solvents were obtained from commercial sources and used as received. Air-sensitive reactions were performed under a nitrogen atmosphere using Schlenk techniques, no special precautions were taken to exclude air or moisture during work-up and crystallisation. Anhydrous THF, DCM and acetonitrile were obtained from a MBraun SPS5 solvent purification system. Flash column chromatography was carried out using silica gel (Silia-P from Silicycle, 60 Å, 40-63 μm). Analytical thin-layer-chromatography (TLC) was performed with silica plates with aluminum backings (250 μm with F-254 indicator). TLC visualization was accomplished by 254/365 nm UV lamp. ^{1}H and ^{19}F NMR spectra were recorded on a Bruker Advance spectrometer (500 or 400 MHz for ^{1}H and 471 MHz for ^{19}F). The following abbreviations have been used for multiplicity assignments: "s" for singlet, "d" for doublet, "t" for triplet, "q" for quartet and "m" for multiplet. ^{19}F NMR spectra were recorded with proton decoupling. ^{1}H NMR spectra were referenced residual solvent peaks with respect to TMS (δ = 0 ppm).

Photophysical measurements. Optically dilute solutions of concentrations on the order of 10^{-5} or 10^{-6} M were prepared in spectroscopic or HPLC grade solvents for absorption and emission analysis. Absorption spectra were recorded at room temperature on a Shimadzu UV-2600 double beam spectrophotometer with a 1 cm quartz cuvette. Molar absorptivity determination was verified by linear regression analysis of values obtained from at least five independent solutions at varying concentrations with absorbance ranging from 6.88×10^{-1} to 3.19×10^2 μM.

For emission studies, aerated solutions were bubbled with compressed air for 5 minutes and spectra were taken using the cuvette for absorption analysis. Degassed solutions were prepared via three freeze-pump-thaw cycles and spectra were taken using home-made Schlenk quartz cuvette. Steady-state emission, excitation spectra and time-resolved emission spectra were recorded at 298 K using either an Edinburgh Instruments F980 or

FS5. For steady-state measurements, samples were excited at 450 nm for $[Ru(bpy)_3](PF_6)_2$, 390 nm for $[Ir(ppy)_2(dtbbpy)]PF_6$, 380 nm for $[Ir(dF(CF_3)ppy)_2(dtbbpy)]PF_6$, $[Cu(dmp)(xantphos)]PF_6$ and **2CzPN**, 520 nm for **Eosin Y**, 420 nm for **4CzIPN**, and 360 nm for **pDTCz-DPmS**. For time-resolved measurements, samples were excited at 378 nm.

Fitting of time-resolved luminescence measurements. Time-resolved PL measurements were fitted to a sum of exponentials decay model, with chi-squared (χ^2) values between 0.9 and 2, using the FS5 software. Each component of the decay is assigned a weight, (w_i), which is the contribution of the emission from each component to the total emission.

Stern-Volmer quenching studies. Optically dilute solutions of the photocatalyst with concentrations on the order of 10^{-5} to 10^{-6} M were prepared in spectroscopic or HPLC grade solvents for steady-state emission analysis. Degassed solutions were prepared by sparging with solvent saturated N_2 gas for 20 minutes prior to measurements. Aliquots of quencher solution were added to the cuvette, equipped with a septum, using a microsyringe. The cuvette was shaken briefly to ensure mixing of the quencher with the PC solution before the emission was recorded.

Electrochemistry measurements. Cyclic Voltammetry (CV) analysis was performed on an Electrochemical Analyzer potentiostat model 620E from CH Instruments at a sweep rate of 100 mV/s. Differential pulse voltammetry (DPV) was conducted with an increment potential of 0.004 V and a pulse amplitude, width, and period of 50 mV, 0.05, and 0.5 s, respectively. Samples were prepared as tetrahydrofuran (THF), dichloromethane (DCM), *N,N*-dimethylformamide (DMF) or acetonitrile (MeCN), solutions, which were degassed by sparging with solvent-saturated N_2 gas for 5 minutes prior to measurements. All measurements were performed using 0.1 M solution of tetra-*n*-butylammonium hexafluorophosphate ($[^nBu_4N]PF_6$). An Ag/Ag^+ electrode was used as the reference electrode while a glassy carbon electrode and a platinum wire were used as the working electrode and counter electrode, respectively. The redox potentials are reported relative to a saturated calomel electrode (SCE) with a ferrocenium/ferrocene (Fc/Fc^+) redox couple

as the internal standard (0.38 V vs SCE for MeCN, 0.46 V vs SCE for DCM, 0.56 V vs SCE for THF and 0.45 V vs SCE for DMF).[9,10]

Theoretical Calculations. Density functional theory (DFT) calculations were performed on each of the eight photocatalysts. First, the structure of the photocatalyst in the singlet ground state was optimized. This was followed by two single point calculations, at the same geometry, of the radical cation and radical anion species, with a charge of +1 and -1 compared to the neutral form, respectively. The neutral form refers to the charge of the PC in its ground state; for the organic PCs, the neutral form has charge of 0, for the organometallic PCs, the neutral form refers to the +1 or +2 charge of the PC (depending on the PC in question). The difference in the total energy of the radical cation and radical anion of each PC compared to its neutral state was used to calculate the ionisation energy and electron affinity of each PC, respectively. Time-dependent density functional theory (TD-DFT)[11] was then used to calculate the 10 lowest energy vertical electronic excited states of both singlet and triplet multiplicity, again at the same geometry, from which the energies of S_1 and T_1 were obtained. The geometry of the triplet state of each PC was then optimized at the same level of theory using an unrestricted wavefunction, followed by a singlet single point calculation at the same triplet geometry. The difference in total energy between these two calculations was used to estimate the phosphorescence emission energy. Calculations of the organic PCs employed the PBE0 functional,[12] GD3BJ empirical dispersion,[13] and the 6-31G** basis set,[14–16] while the organometallic PCs utilised the B3LYP functional,[17] GD3BJ empirical dispersion and the SBKJC-VDZ basis set (with effective core potentials)[18–21] for metal elements and the 6-31+G**[14–16,22] basis set for light elements. [23]The radical calculations were performed in the doublet state using unrestricted orbitals, while the single point, ground-state optimisation and excited-state calculations were performed in the singlet state using restricted orbitals. The optimised triplet state calculations were performed using unrestricted orbitals in the triplet state. Cationic organometallic complexes were considered as single species without outer-sphere counter-ions (i.e., as charged molecules). Both organic and organometallic PCs used the same functional and basis set(s) for the excited-state calculations as for the ground state, radical and optimised triplet calculations. Each of the six calculations for each PC were repeated using four different solvents, THF, DCM, DMF, and MeCN, using the implicit solvation

polarizable continuum model (IEFPCM).[24–26] TD-DFT excited state calculations were performed using the state specific correction procedure of Scalmani[27] and co-workers for the S_1 state, and using a non-equilibriated solvent environment. All calculations were performed using Gaussian 16, revision C.01,[28] and all program defaults, except those noted above, were left as default for that program. All calculations were submitted and processed using in-house developed software, Silico ver 2.1, which incorporates a number of publicly available software libraries, including: cclib[29] for parsing of result files, VMD/Tachyon[30,31] for 3D rendering, Matplotlib[32] for drawing of graphs and Open Babel/Pybel[33,34] for file interconversion.

The electronic distribution and localization of the singlet excited states were visualized using the electron density difference maps (ED-DMs).[35] *GaussSum 2.2*[29] and *Chemissian* v4.67[36] were employed to visualize the absorption spectra (simulated with Gaussian distribution with a full-width at half maximum (fwhm) set to 3000 cm^{-1}) and to calculate the fractional contributions of various groups to each molecular orbital. All calculated structures and Kohn-Sham orbitals were visualized with Gaussview v5.0.[37]

DFT calculations

HOMO energies, LUMO energies and the ground-state dipole moment magnitude were calculated at the ground-state optimised geometry. S_1 and T_1 are the vertical electronic excited-state energies of the lowest energy singlet and triplet excited states, respectively, at the ground state geometry. ΔE_{ST} is the difference between them. Density plots of the HOMO and LUMO are taken from the ground-state optimised calculation in MeCN.

The S_1 energies were calculated using time-dependent DFT at the S_0 ground state geometry, using the state specific solvent correction of Scalmani *et al.*[27] and non-equilibrium solvation, thus modelling a vertical absorption process. Meanwhile, the T_1 energies were calculated *via* the delta-SCF approach comparing the optimised T_1 geometry calculated using unrestricted DFT and the S_0 energy at the same geometry, thus modelling a vertical, de-excitation (or emission) process. For **[Ru(bpy)₃]²⁺**, **[Cu(dmp)(xantphos)]⁺**, **Eosin Y**, **4CzIPN**, **2CzPN** and **pDTCz-DPmS**, both excited-state energies remained essentially constant across the four solvents, varying only between 0-0.04 eV. The excited-state energies of the iridium complexes, by comparison, show a greater degree of solvent dependency, with the excited states increasing in energy (up to 0.16 eV) in more polar solvents. For example, the T_1 state of **[Ir(dF(CF₃)ppy)₂(dtbbpy)]⁺** increases in energy from 2.42 eV in THF to 2.58 eV in MeCN. This is in direct contrast to what is observed experimentally (Table **1** in the main manuscript), whereby the $E_{0,0}(T_1)$ remains essentially constant, suggesting that *in silico* modelling is not appropriate to predict excited state energies.

[Ru(bpy)₃]²⁺

Table **S1**. Selected data from DFT calculations for **[Ru(bpy)₃]²⁺** in the four solvents.

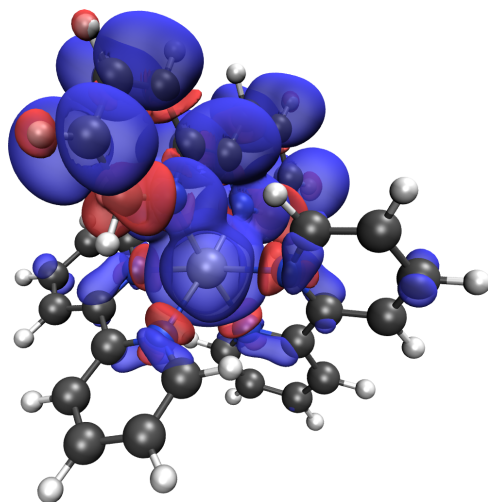|	THF	DCM	DMF	MeCN
HOMO / eV	-6.77	-6.66	-6.24	-6.24
LUMO / eV	-3.30	-3.19	-2.78	-2.78
$\Delta E_{HOMO-LUMO}$ / eV	3.47	3.47	3.46	3.46
Ground-state dipole moment magnitude / D	0.03	0.03	0.02	0.02
S_1 / eV	2.63	2.64	2.63	2.63
T_1 / eV	1.95	1.95	1.92	1.92
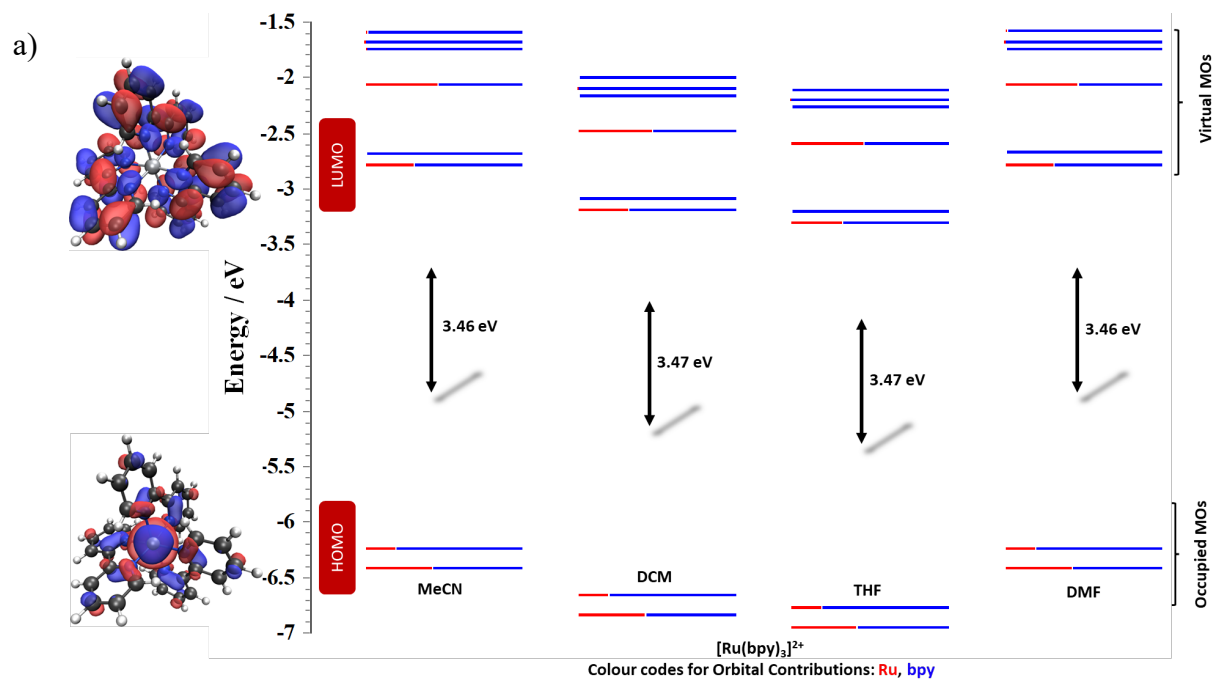
Figure **S1**. a) Orbital contributions for **[Ru(bpy)₃]²⁺** in the four solvents and b) total spin density in the optimized triplet state in MeCN.

[Ir(ppy)$_2$(dtbbpy)]$^+$

Table **S2**. Selected data from DFT calculations for **[Ir(ppy)$_2$(dtbbpy)]$^+$** in the four solvents.

	THF	DCM	DMF	MeCN
HOMO / eV	-6.01	-5.96	-5.81	-5.82
LUMO / eV	-2.76	-2.71	-2.48	-2.49
$\Delta E_{HOMO-LUMO}$ / eV	3.24	3.26	3.33	3.33
Ground state dipole moment magnitude / D	8.76	8.89	9.51	9.50
S_1 / eV	2.56	2.58	2.65	2.65
T_1 / eV	2.13	2.13	2.15	2.15
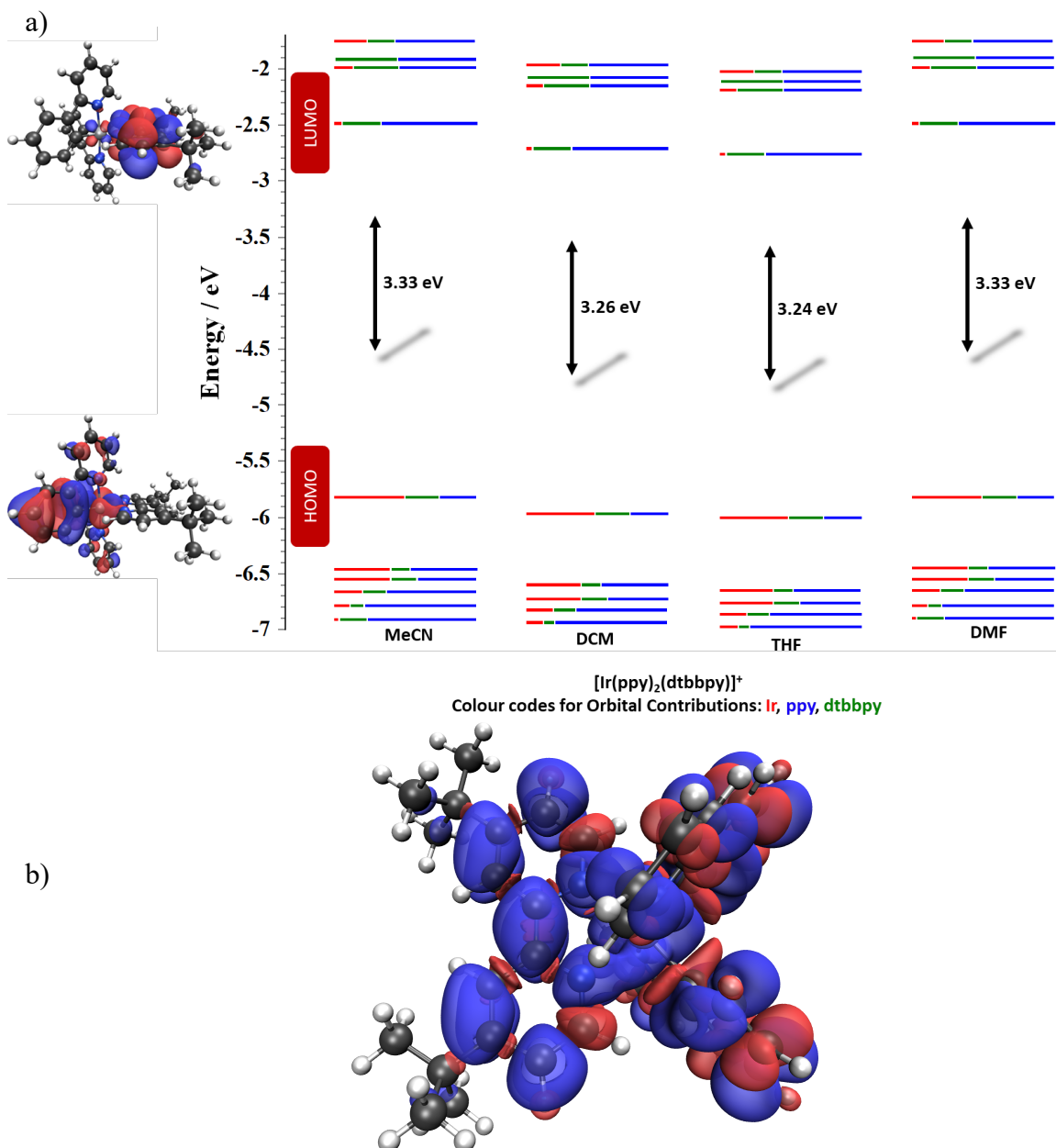
Figure **S2**. a) Orbital contributions for **[Ir(ppy)₂(dtbbpy)]⁺** in the four solvents and b) total spin density in the optimized triplet state in MeCN.

[Ir(dF(CF₃)ppy)₂(dtbbpy)]⁺

Table **S3**. Selected data from DFT calculations for **[Ir(dF(CF₃)ppy)₂(dtbbpy)]⁺** in the four solvents.[a]

	THF	DCM	DMF	MeCN
HOMO / eV	-6.64	-6.59	-6.38	-6.39
LUMO / eV	-2.97	-2.91	-2.65	-2.65
$\Delta E_{HOMO-LUMO}$ / eV	3.67	3.68	3.73	3.74
Ground state dipole moment magnitude / D	9.42	9.58	9.94	9.96
S_1 / eV	2.99	3.00	3.06	3.06
T_1 / eV	2.42	2.43	2.42	2.58

[a] Ground-state optimisation for DCM and DMF each had 1 small negative frequency each (-5.04 cm⁻¹ and -17.22 cm⁻¹, respectively).

a)
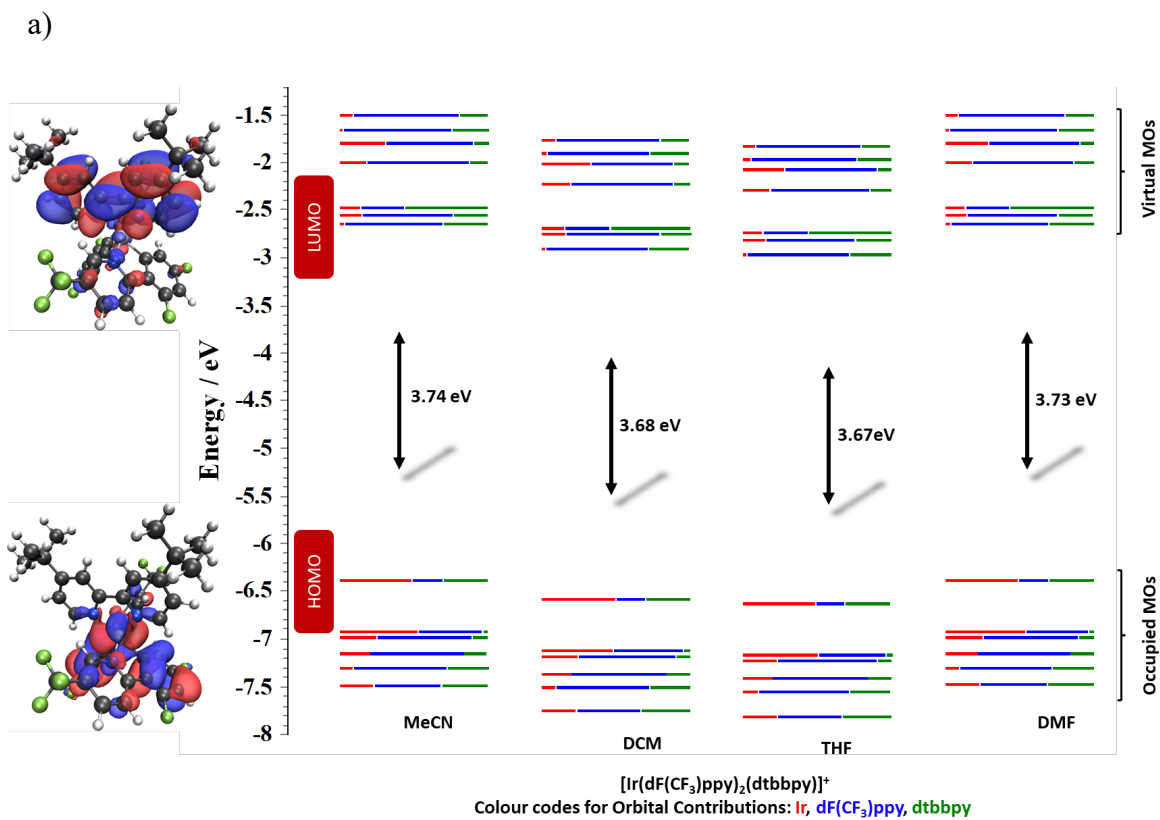
b)
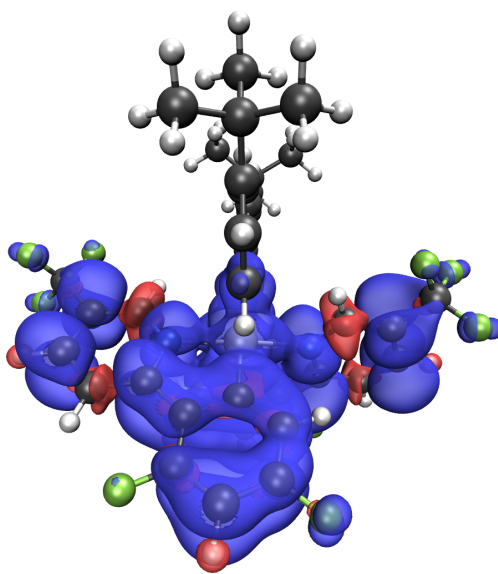
Figure **S3**. a) Orbital contributions for **[Ir(dF(CF₃)ppy)₂(dtbbpy)]**⁺ in the four solvents and b) total spin density in the optimized triplet state in MeCN.

[Cu(dmp)(xantphos)]⁺

Table **S4.** Selected data from DFT calculations for **[Cu(dmp)(xantphos)]⁺** in the four solvents.

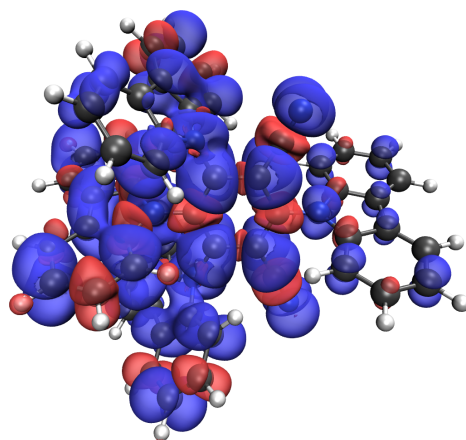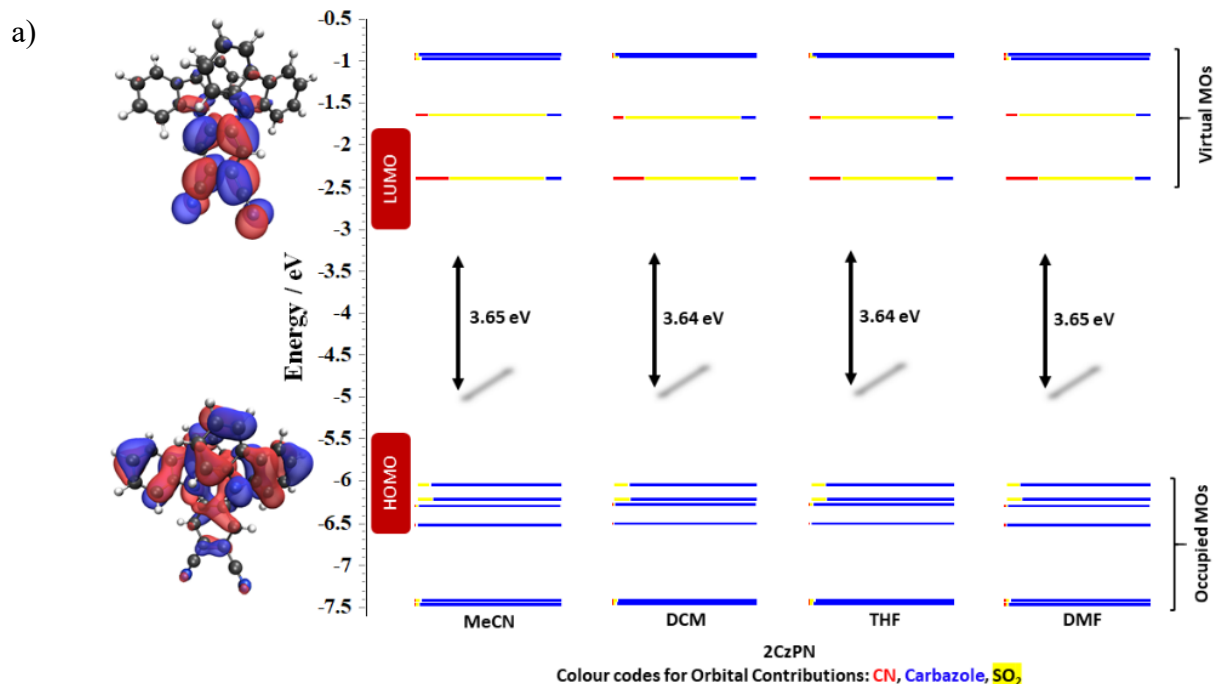|	THF	DCM	DMF	MeCN
HOMO / eV	-6.06	-6.02	-5.86	-5.86
LUMO / eV	-2.53	-2.48	-2.29	-2.29
$\Delta E_{HOMO\text{-}LUMO}$ / eV	3.53	3.54	3.57	3.57
Ground state dipole moment magnitude / D	5.76	5.82	6.10	6.10
S_1 / eV	2.90	2.90	2.93	2.93
T_1 / eV	1.72	1.80	1.79	1.79
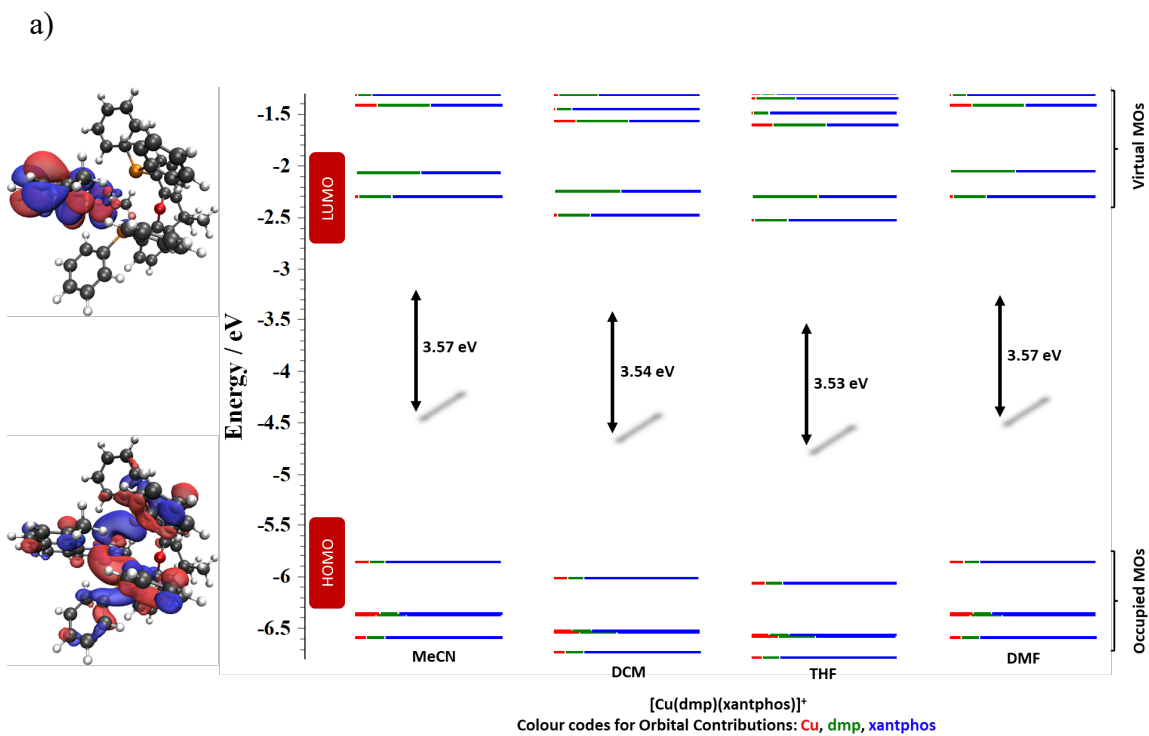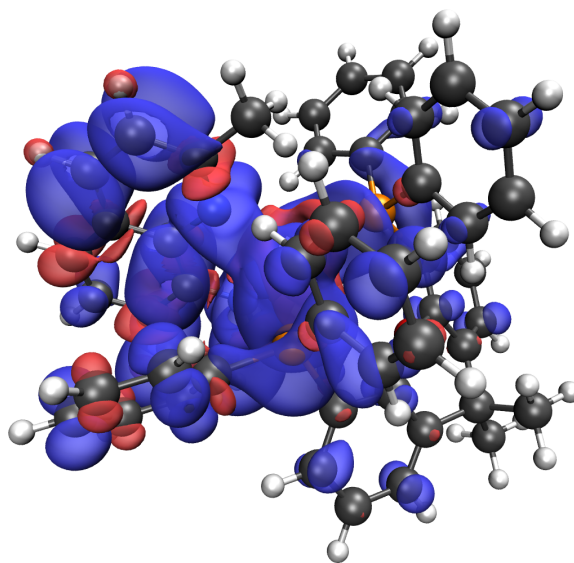
Figure **S4**. a) Orbital contributions for **[Cu(dmp)(xantphos)]**[+] in the four solvents and b) total spin density in the optimized triplet state in MeCN.

Eosin Y

Table **S5**. Selected data from DFT calculations for **Eosin Y** in the four solvents.

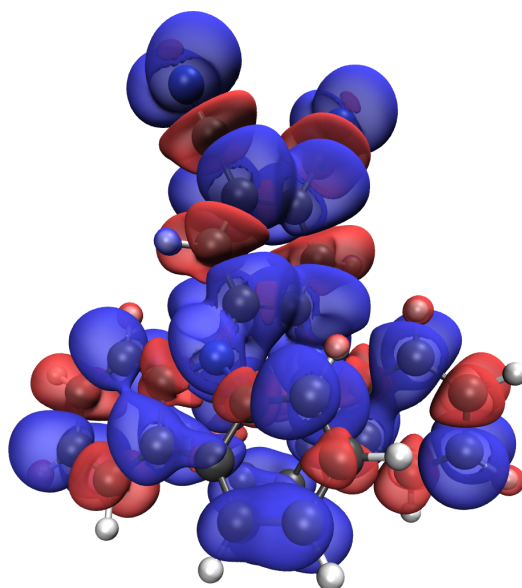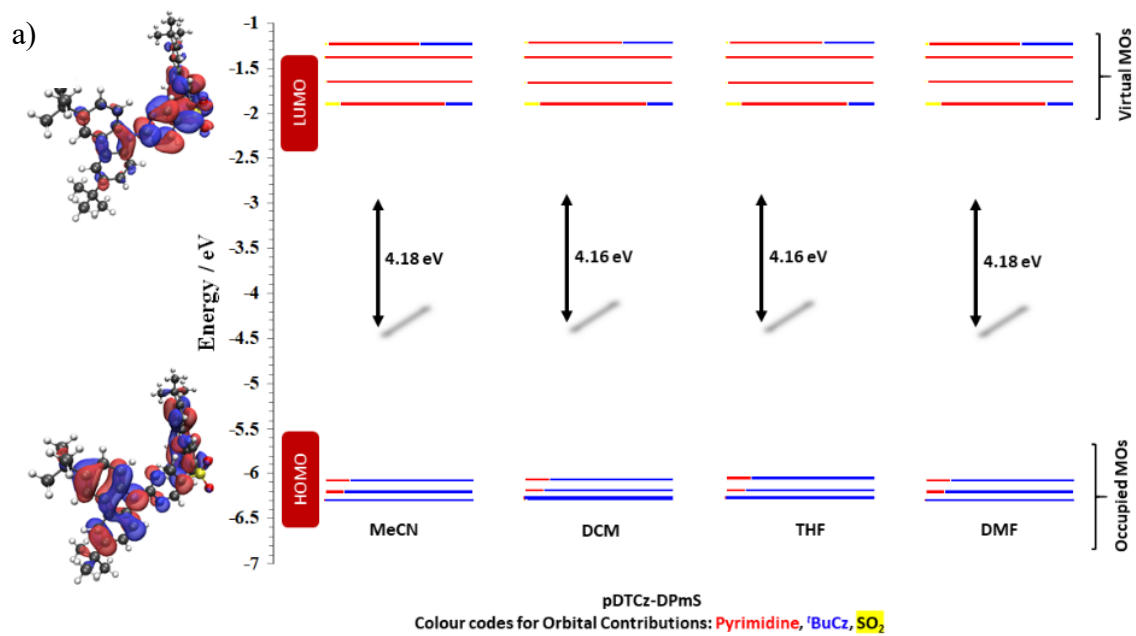| Select data from DFT calculations:	THF	DCM	DMF	MeCN
HOMO / eV	-6.61	-6.61	-6.62	-6.62
LUMO / eV	-1.50	-1.50	-1.50	-1.50
$\Delta E_{HOMO\text{-}LUMO}$ / eV	5.11	5.11	5.12	5.12
Ground state dipole moment magnitude / D	6.47	6.54	6.83	6.82
S_1 / eV	4.35	4.35	4.35	4.35
T_1 / eV	3.07	3.07	3.06	3.06

a)
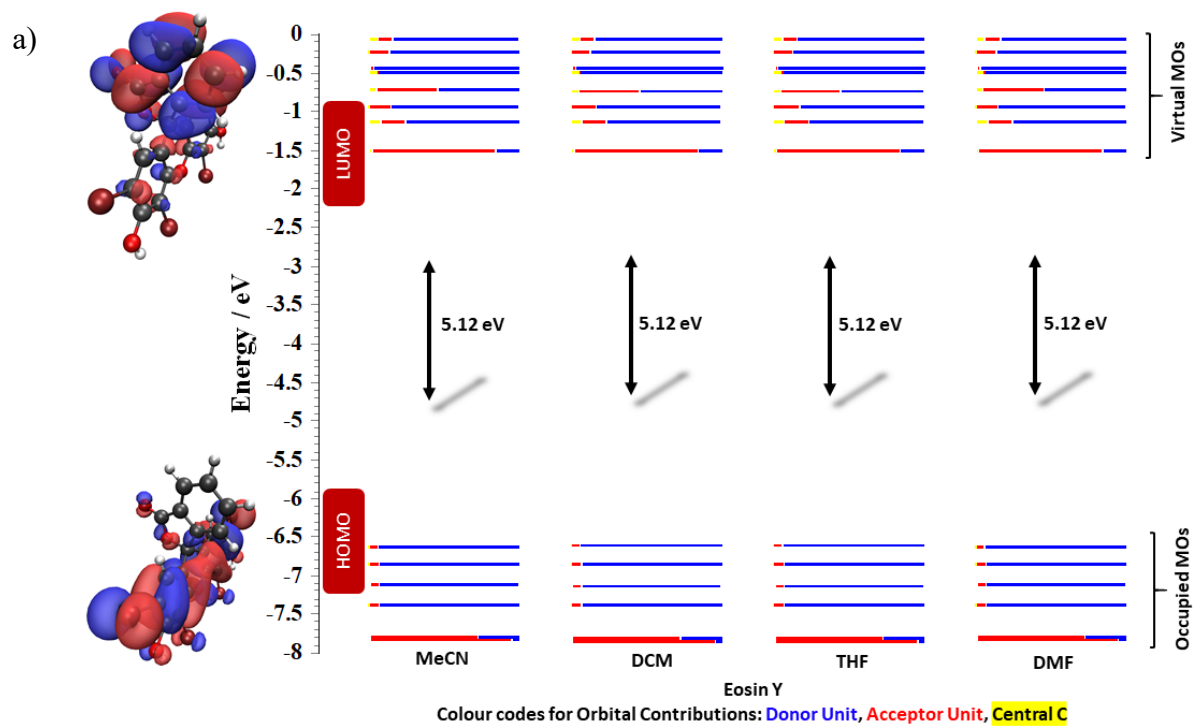
b)
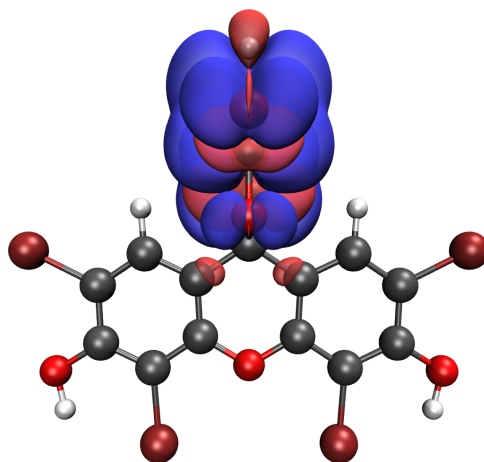
Figure **S5**. a) Orbital contributions for **Eosin Y** in the four solvents and b) total spin density in the optimized triplet state in MeCN.

4CzIPN

Table **S6**. Selected data from DFT calculations for **4CzIPN** in the four solvents.[a]

	THF	DCM	DMF	MeCN
HOMO / eV	-5.98	-5.99	-6.02	-6.02
LUMO / eV	-2.51	-2.54	-2.54	-2.54
$\Delta E_{HOMO-LUMO}$ / eV	3.47	3.47	3.48	3.48
Ground state dipole moment magnitude / D	5.35	5.36	5.32	5.31
S_1 / eV	2.66	2.66	2.66	2.66
T_1 / eV	2.15	2.11	2.09	2.11

[a] Triplet optimisation for MeCN and THF had 1 small negative frequency each (-19.80 cm^{-1} and -13.61 cm^{-1} respectively).

a)

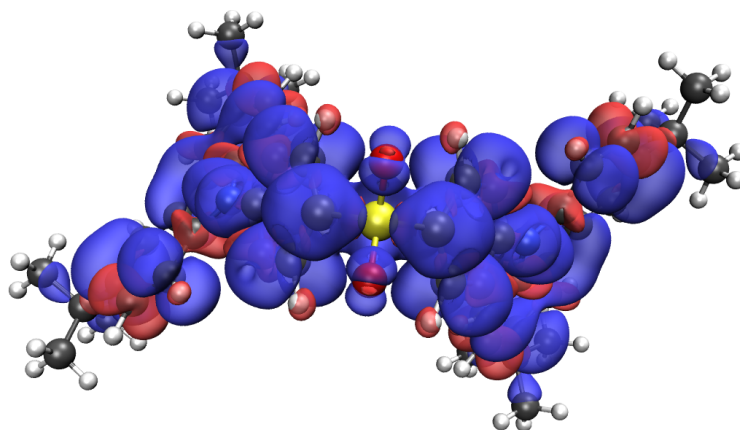Colour codes for Orbital Contributions: Carbazole donor groups, benzene core, CN
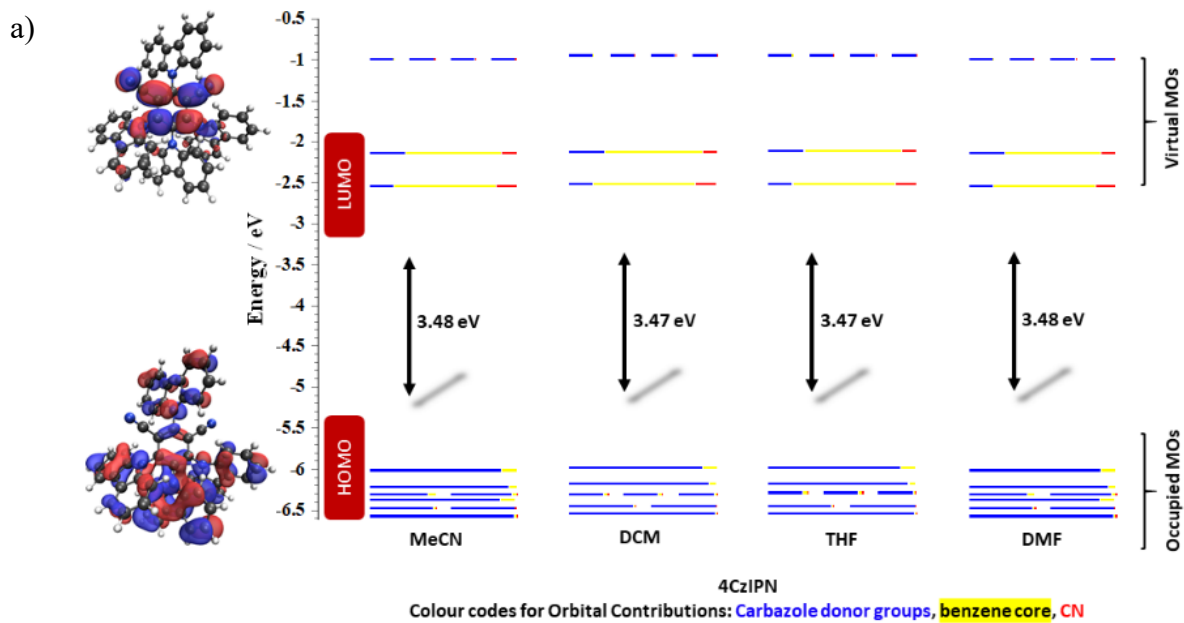
b)

Figure **S6**. a) Orbital contributions for **4CzIPN** in the four solvents and b) total spin density in the optimized triplet state in MeCN.

2CzPN

Table **S7**. Selected data from DFT calculations for **2CzPN** in the four solvents.

	THF	DCM	DMF	MeCN
HOMO / eV	-6.04	-6.04	-6.04	-6.04
LUMO / eV	2.40	-2.40	-2.39	-2.40
$\Delta E_{HOMO\text{-}LUMO}$ / eV	3.64	3.64	3.65	3.64
Ground state dipole moment magnitude / D	8.41	8.41	8.35	8.35
S_1 / eV	2.90	2.90	2.90	2.90
T_1 / eV	2.18	2.18	2.14	2.14

a)

Colour codes for Orbital Contributions: CN, Carbazole, SO₂

b)

Figure **S7**. a) Orbital contributions for **2CzPN** in the four solvents and b) total spin density in the optimized triplet state in MeCN.

pDTCz-DPmS

Table **S8**. Selected data from DFT calculations for **pDTCz-DPmS** in the four solvents.

	THF	DCM	DMF	MeCN
HOMO / eV	-6.05	-6.06	-6.08	-6.08
LUMO / eV	-1.89	-1.89	-1.90	-1.90
$\Delta E_{HOMO-LUMO}$ / eV	4.16	4.17	4.18	4.18
Ground state dipole moment magnitude / D	5.72	5.75	5.91	5.91
S_1 / eV	3.47	3.47	3.47	3.47
T_1 / eV	2.75	2.51	2.71	2.71

a)

Energy / eV

Virtual MOs

4.18 eV   4.16 eV   4.16 eV   4.18 eV

Occupied MOs

MeCN   DCM   THF   DMF

pDTCz-DPmS
Colour codes for Orbital Contributions: Pyrimidine, ᵗBuCz, SO₂

b)

Figure **S8**. a) Orbital contributions for **pDTCz-DPmS** in the four solvents and b) total spin density in the optimized triplet state in MeCN.

Table **S9**. Calculated ionization potentials and electron affinities for the eight PCs in the four different solvents.[a]

		THF	DCM	DMF	MeCN
[Ru(bpy)$_3$]$^{2+}$	IP/ eV	-6.58	-6.59	-7.12	-7.11
	EA / eV	-3.31	-3.23	-2.93	-2.93
[Ir(ppy)$_2$(dtbbpy)]$^+$	IP / eV	-5.99	-5.92	-5.65	-5.65
	EA / eV	-2.71	-2.69	-2.60	-2.60
[Ir(dF(CF$_3$)ppy)$_2$(dtbbpy)]$^+$	IP / eV	-6.64	-6.56	-6.23	-6.24
	EA / eV	-2.93	-2.90	-2.77	-2.78
[Cu(dmp)(xantphos)]$^+$	IP / eV	-6.03	-5.96	-5.70	-5.70
	EA / eV	-2.24	-2.23	-2.18	-2.18
Eosin Y	IP / eV	-6.57	-6.54	-6.41	-6.41
	EA / eV	-1.50	-1.53	-1.69	-1.69
4CzIPN	IP / eV	-5.89	-5.87	-5.79	-5.79
	EA / eV	-2.61	-2.65	-2.79	-2.79
2CzPN	IP / eV	-5.95	-5.92	-5.80	-5.80
	EA / eV	-2.44	-2.47	-2.61	-2.61
pDTCz-DPmS	IP / eV	-5.98	-5.96	-5.88	-5.89
	EA / eV	-1.98	-2.01	-2.14	-2.14

[a] The level of theory used was PBE0/6-31G**/GD3BJ for organic PCs and B3LYP/6-31+G**/SBKJC-VDZ-ECP/GD3BJ for organometallic PCs.

Electrochemistry
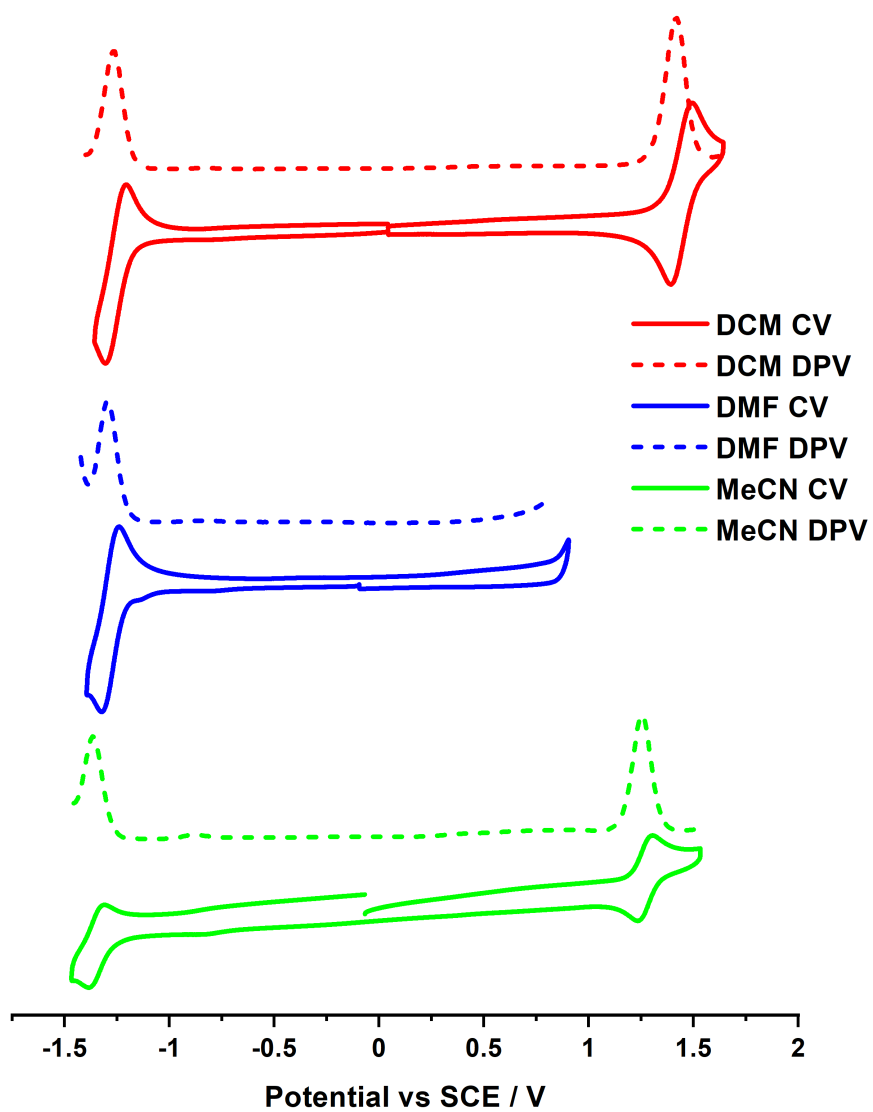
Figure **S9**. CV and DPV obtained for **[Ru(bpy)₃](PF₆)₂** in the various solvents at scan rate of 0.1 V s^{-1}.
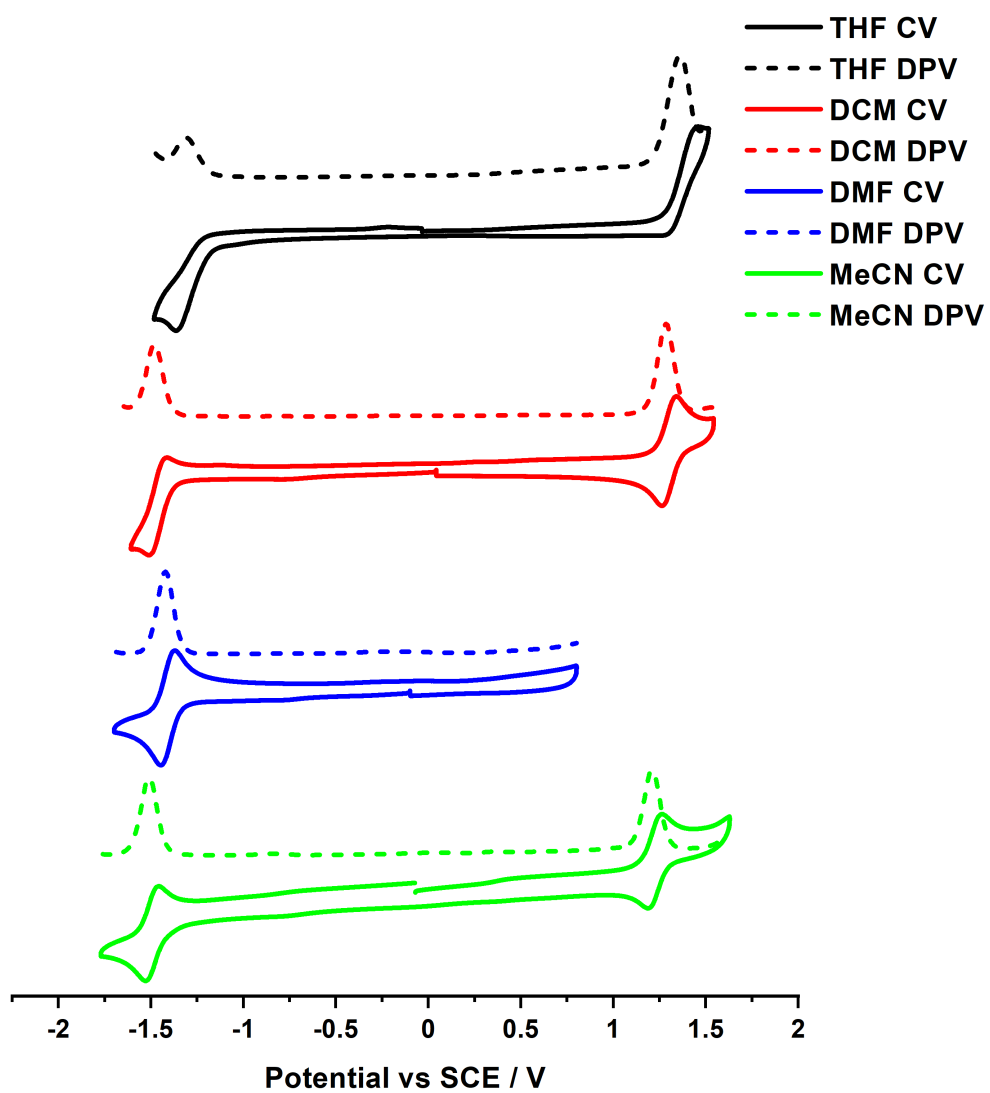
Figure **S10**. CV and DPV obtained for **[Ir(ppy)₂(dtbbpy)]PF₆** in the various solvents at scan rate of 0.1 V s^{-1}.
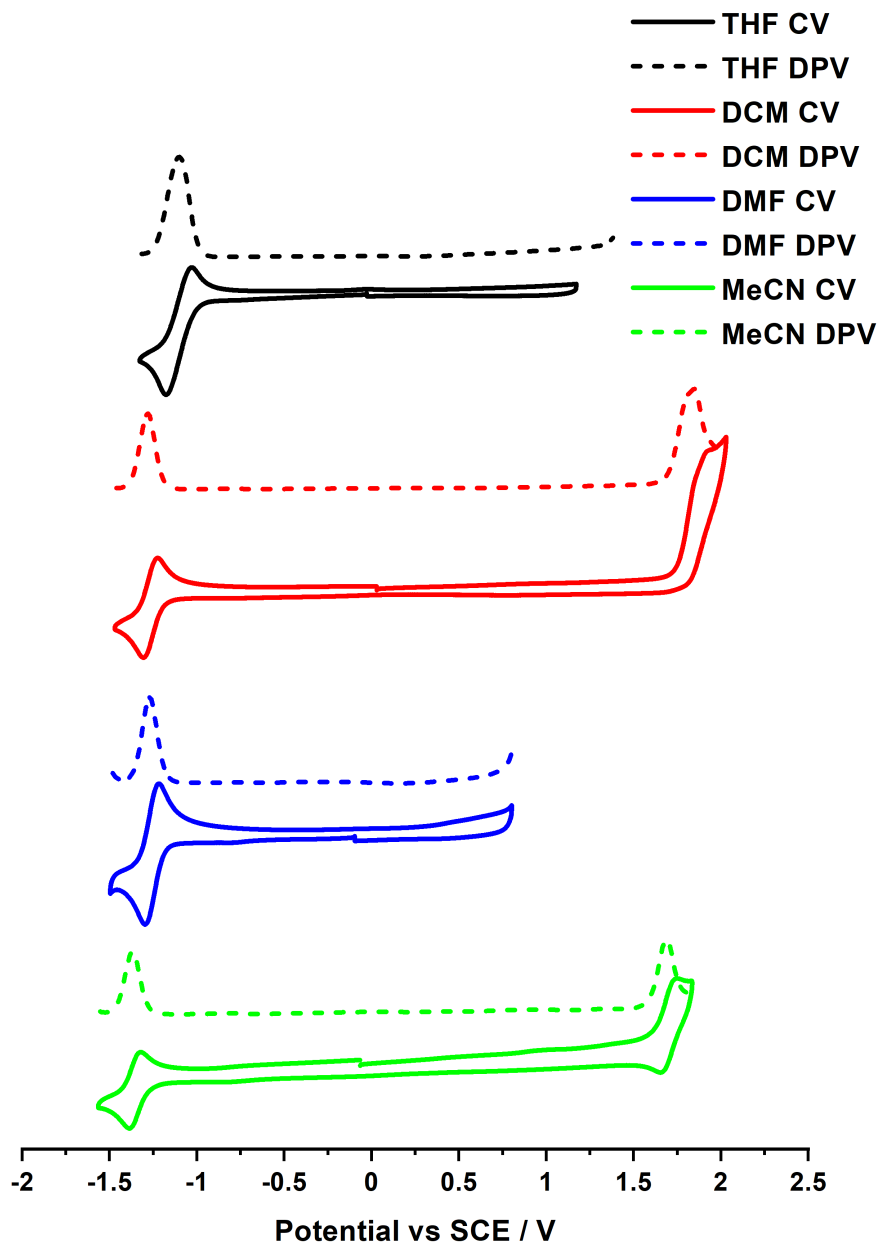
Figure **S11**. CV and DPV obtained for **[Ir(dF(CF₃)ppy)₂(dtbbpy)]PF₆** in the various solvents at scan rate of 0.1 V s⁻¹.
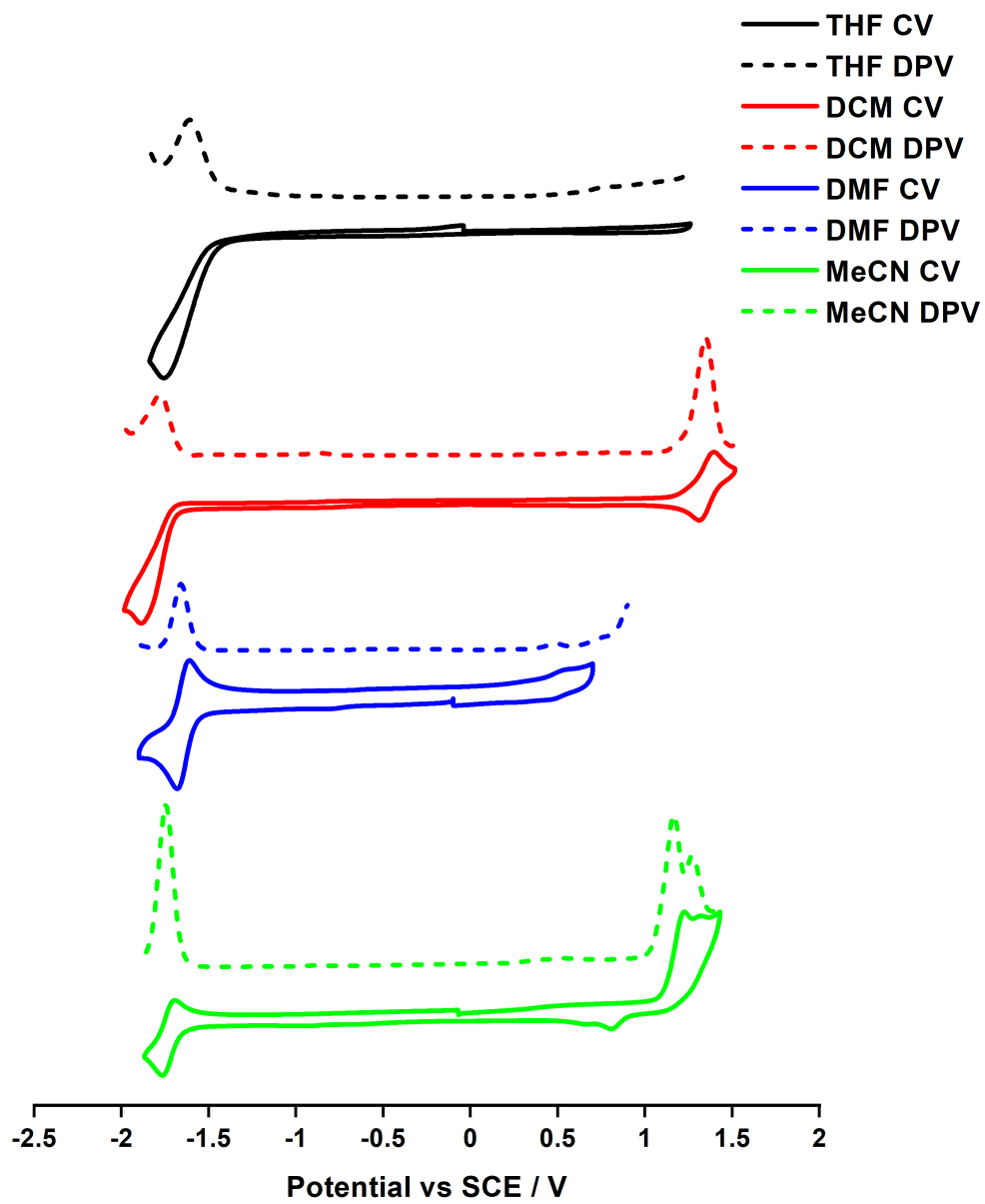
Figure **S12**. CV and DPV obtained for **[Cu(dmp)(xantphos)]PF$_6$** in the various solvents at scan rate of 0.1 V s^{-1}.
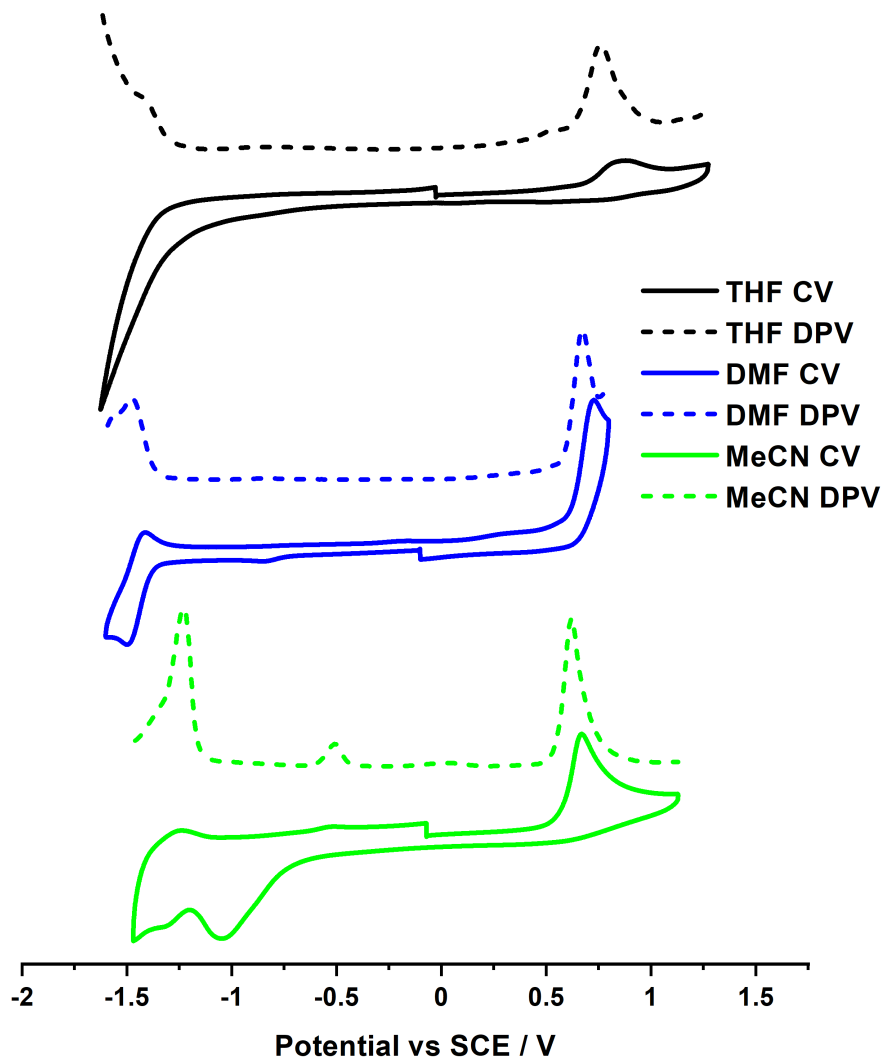
Figure **S13**. CV and DPV obtained for **Eosin Y** in the various solvents at scan rate of 0.1 V s^{-1}.
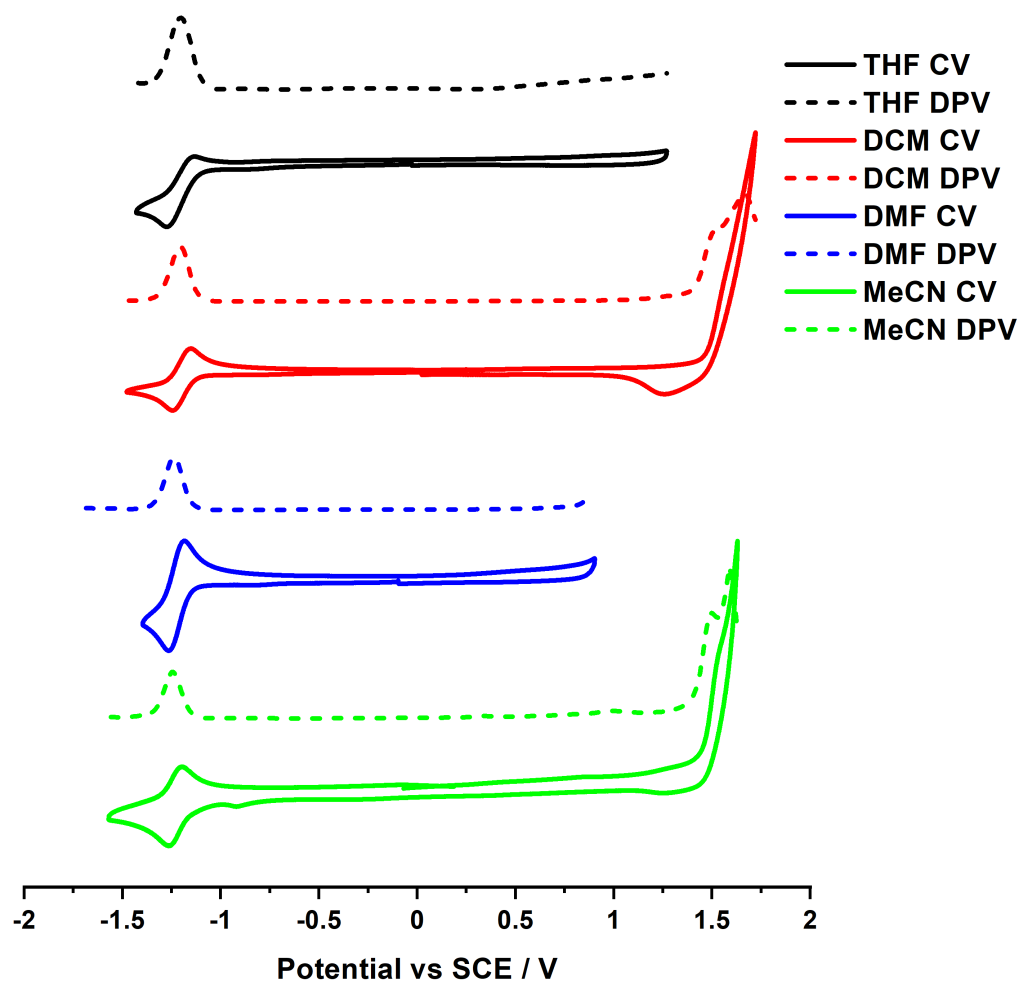
Figure **S14**. CV and DPV obtained for **4CzIPN** in the various solvents at scan rate of 0.1 V s^{-1}. Spectra taken from Ref [7].
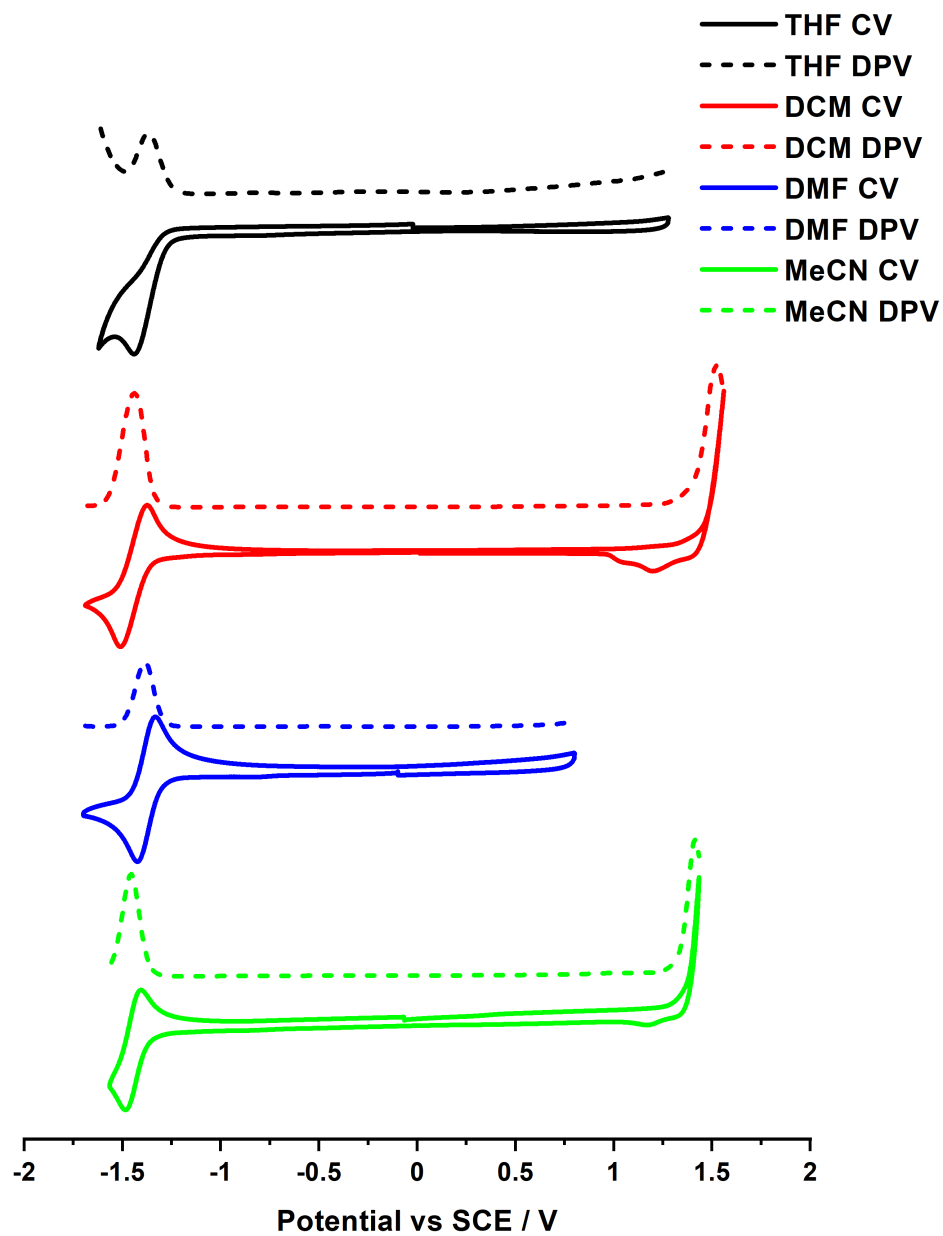
Figure **S15**. CV and DPV obtained for **2CzPN** in the various solvents at scan rate of 0.1 V s^{-1}.
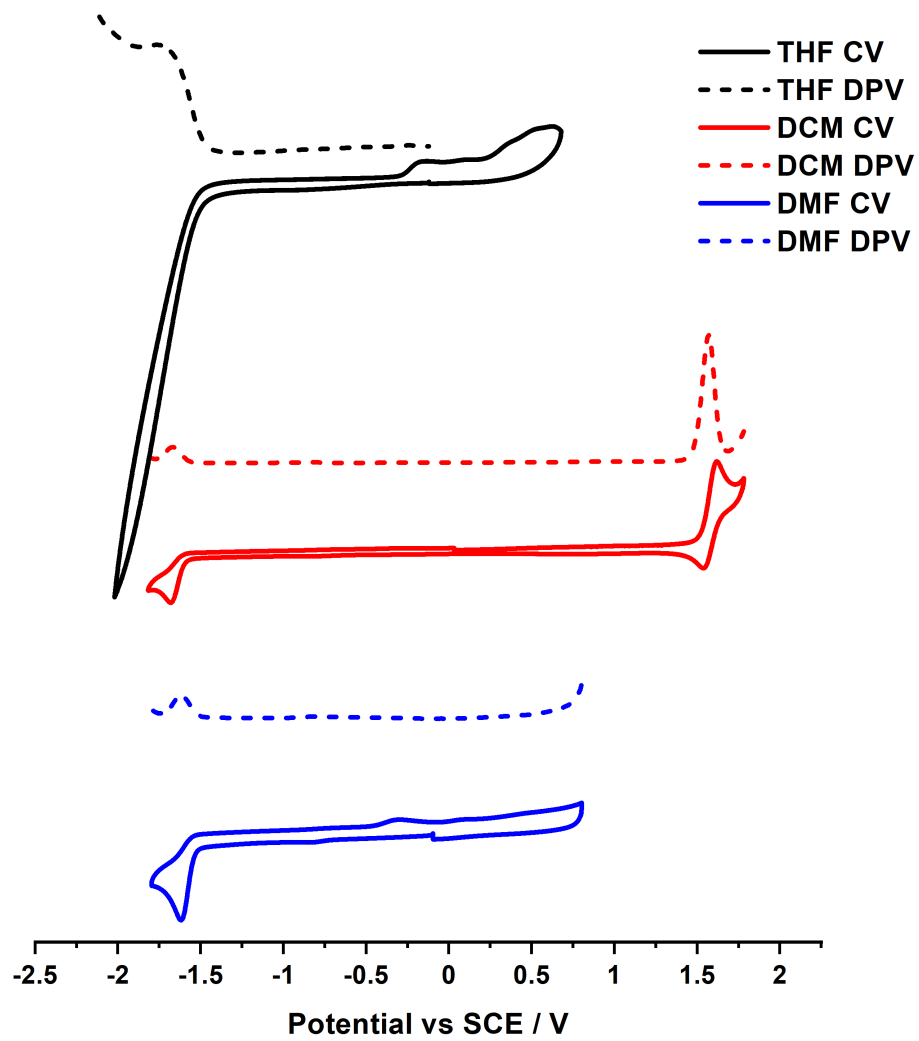
Figure **S16**. CV and DPV obtained for **pDTCz-DPmS** in the various solvents at scan rate of 0.1 V s^{-1}. Spectra taken from Ref [7].

Table **S10**. Ground-state redox potentials of the eight PCs in the four solvents.[a]

		THF	DCM	DMF	MeCN
[Ru(bpy)₃](PF₆)₂	E_{ox} / V		1.42		1.25 (1.29) [b]
	E_{red} / V		-1.27	-1.29	-1.37 (-1.33) [b]
	ΔE / V		2.69		2.62
[Ir(ppy)₂(dtbbpy)]PF₆	E_{ox} / V	1.36	1.28		1.21 (1.21) [c]
	E_{red} / V	-1.31	-1.48	-1.42	-1.51 (-1.51) [c]
	ΔE / V	2.67	2.76		2.72
[Ir(dF(CF₃)ppy)₂(dtbbpy)]PF₆	E_{ox} / V		1.85		1.69 (1.69) [c]
	E_{red} / V	-1.10	-1.28	-1.27	-1.37 (-1.37) [c]
	ΔE / V		3.13		3.06
[Cu(dmp)(xantphos)]PF₆	E_{ox} / V		1.35		1.16 /1.27 (1.20) [d]
	E_{red} / V	-1.61	-1.77	-1.66	-1.75 (-1.73) [d]
	ΔE / V		3.12		2.91/3.02
Eosin Y	E_{ox} / V	0.76		0.67	0.62 (0.78) [e]
	E_{red} / V	-1.43		-1.47	-1.23 (-1.06) [e]
	ΔE / V	2.19		2.14	1.85
4CzIPN	E_{ox} / V		1.51		1.50 (1.49) [f]
	E_{red} / V	-1.20	-1.21	-1.24	-1.24 (-1.24) [f]
	ΔE / V		2.72		2.74
2CzPN	E_{ox} / V		1.53		1.41 (1.47) [g]
	E_{red} / V	-1.37	-1.44	-1.39	-1.46 (-1.45) [g]
	ΔE / V		2.97		2.87
pDTCz-DPmS [h]	E_{ox} / V		1.57		
	E_{red} / V	-1.77	-1.67	-1.62	
	ΔE / V		3.24		

[a] Values are reported vs SCE. Ground state redox potentials are obtained from DPV under N_2. ΔE = E_{red} - E_{ox}. When no value is reported, this is due to poor solubility of the PC in that solvent or no redox wave was detected within the electrochemical window of the solvent. Values in parentheses are taken from the literature. [b] Value taken from Ref [38]. [c] Value taken from Ref [39]. [d] Value taken from Ref [40] and the original values were converted from NHE to SCE using SCE = NHE - 0.25 V.[10] [e] Values taken from Ref [41] which were obtained in a 1:1 MeCN:H_2O co-solvent. [f] Value taken from Ref [42]. [g] Value taken from Ref [43]. [h] Values taken from Ref [7].

Table **S11**. Ground and excited state redox potentials and optical gaps of the eight PCs in the four solvents.[a]

		THF	DCM	DMF	MeCN
[Ru(bpy)₃](PF₆)₂	E^*_{ox} / V		-0.83		-0.96 (-0.81) [b]
	E^*_{red} / V		0.98	0.90	0.84 (0.77) [b]
[Ir(ppy)₂(dtbbpy)]PF₆	E^*_{ox} / V	-1.06	-1.18		-1.23 (-0.96) [c]
	E^*_{red} / V	1.11	0.98	1.01	0.93 (0.66) [c]
[Ir(dF(CF₃)ppy)₂(dtbbpy)]PF₆	E^*_{ox} / V		-0.90		-1.05 (-0.89) [c]
	E^*_{red} / V	1.64	1.47	1.46	1.37 (1.21) [c]
[Cu(dmp)(xantphos)]PF₆	E^*_{ox} / V		-1.32		-1.53/-1.42
	E^*_{red} / V	0.98	0.90	1.04	0.94
Eosin Y	E^*_{ox} / V			-1.62	-1.68 (-1.11) [d]
	E^*_{red} / V			0.82	1.07 (0.83) [d]
4CzIPN	E^*_{ox} / V		-1.09		-1.15 (-1.18) [e]
	E^*_{red} / V	1.46	1.39	1.40	1.41 (1.43) [e]
2CzPN	E^*_{ox} / V		-1.29		-1.38 (-1.30) [f]
	E^*_{red} / V	1.51	1.38	1.39	1.33 (1.32) [f]
pDTCz-DPmS [g]	E^*_{ox} / V		-1.44		
	E^*_{red} / V	1.32	1.34	1.48	

[a] Values are reported vs SCE. $E^*_{ox} = E_{ox} - E_{0,0}$ and $E^*_{red} = E_{red} + E_{0,0}$. When no value is reported, this is due to poor solubility of the PC in that solvent or no redox wave was detected within the electrochemical window of the solvent. Values in parentheses are taken from the literature. [b] Value taken from Ref [38]. [c] Value taken from Ref [39]. [d] Values taken from Ref [41] which were obtained in a 1:1 MeCN:H₂O co-solvent. [e] Value taken from Ref [42]. [f] Value taken from Ref [43]. [g] Values taken from Ref [7].
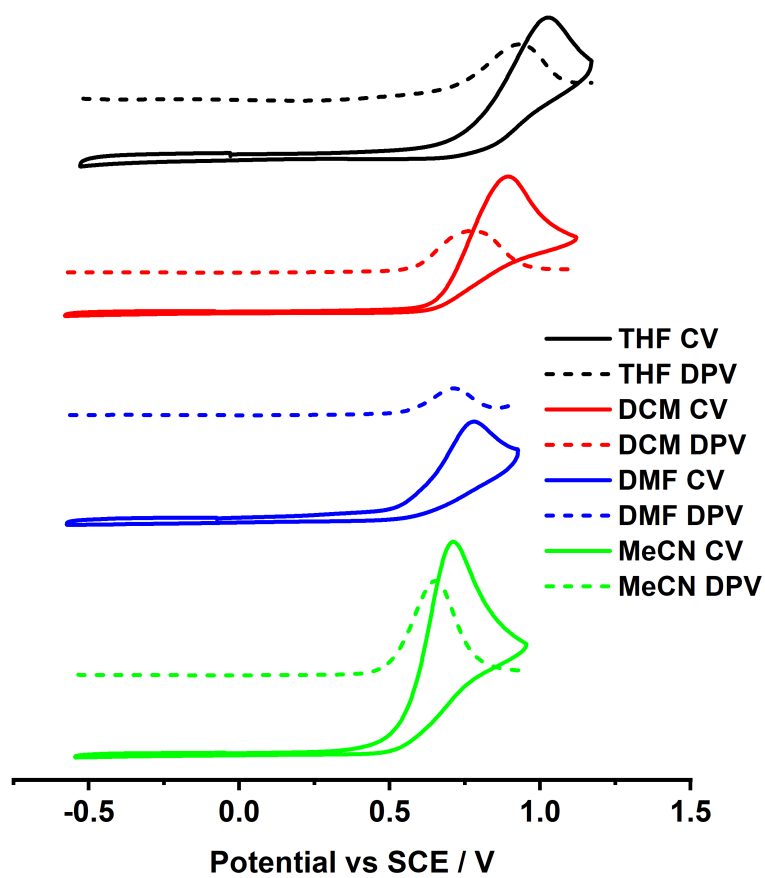
Figure **S17**. CV and DPV obtained for DIPEA in the various solvents at scan rate of 0.1 V s^{-1}.

Table **S12**. Redox potentials obtained in the various solvents for DIPEA.

	THF	DCM	DMF	MeCN
E_{ox} / V	0.93	0.77	0.72	0.65

UV-Vis absorption spectra
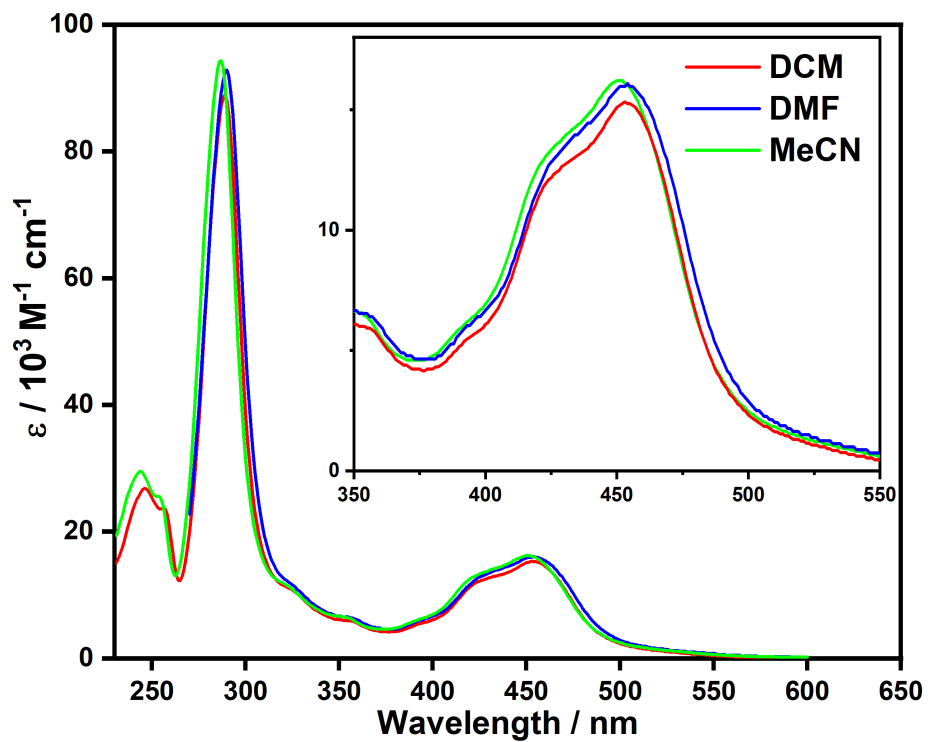
Figure **S18**. UV-vis absorption spectra of **[Ru(bpy)₃](PF₆)₂** in the various solvents.
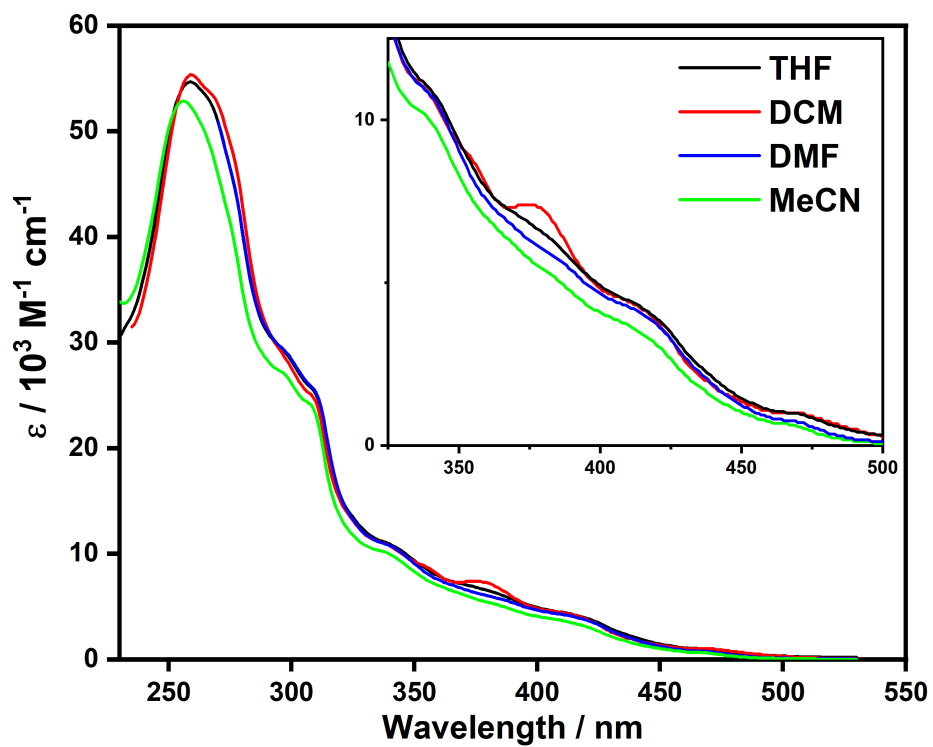
Figure **S19**. UV-vis absorption spectra of **[Ir(ppy)₂(dtbbpy)]PF₆** in the various solvents.
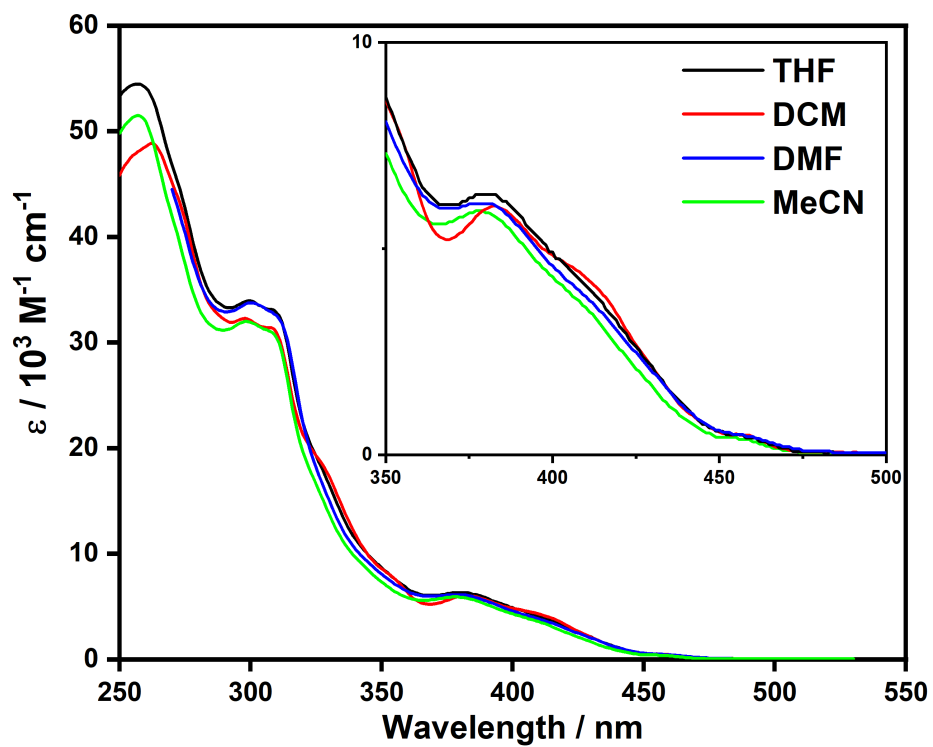
Figure **S20**. UV-vis absorption spectra of **[Ir(dF(CF₃)ppy)₂(dtbbpy)]PF₆** in the various solvents.
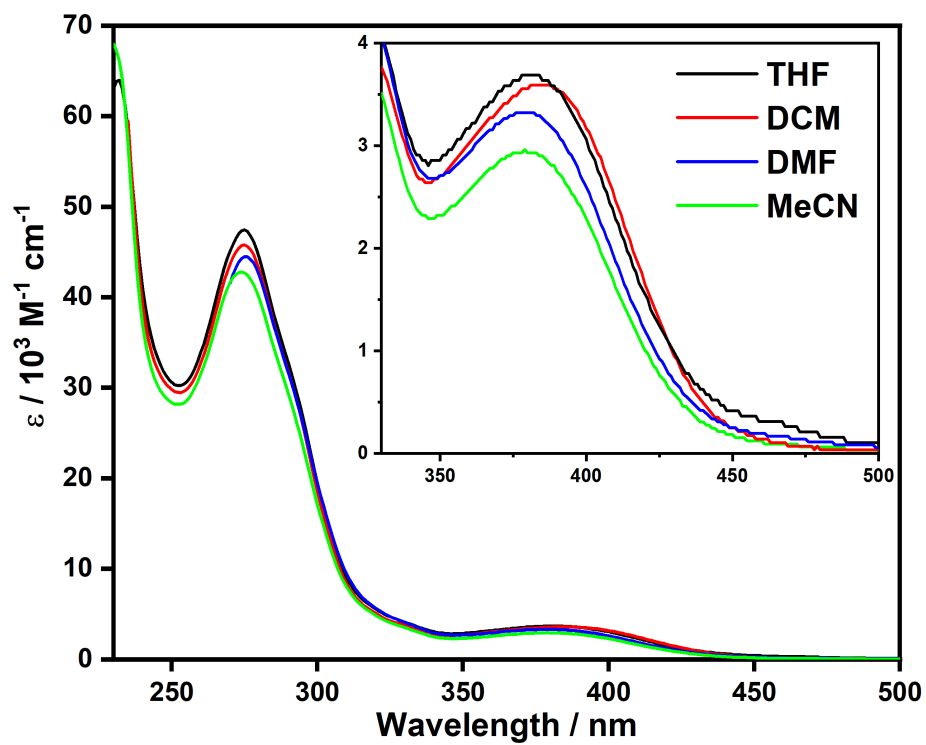
Figure **S21**. UV-vis absorption spectra of **[Cu(dmp)(xantphos)PF₆]** in the various solvents.
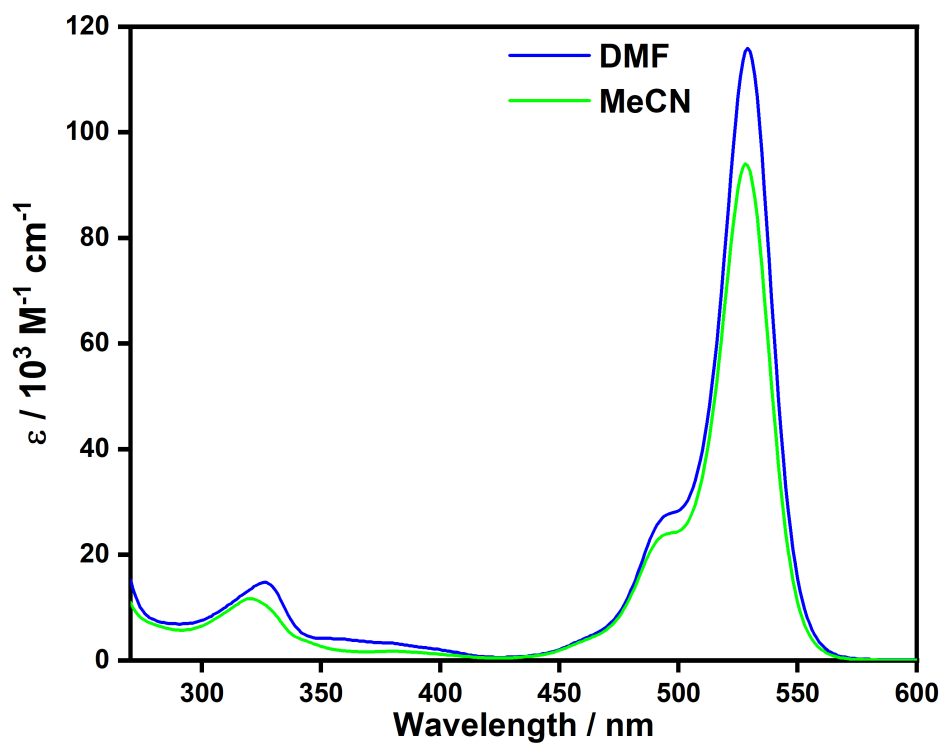
Figure **S22**. UV-vis absorption spectra of **Eosin Y** in the various solvents.
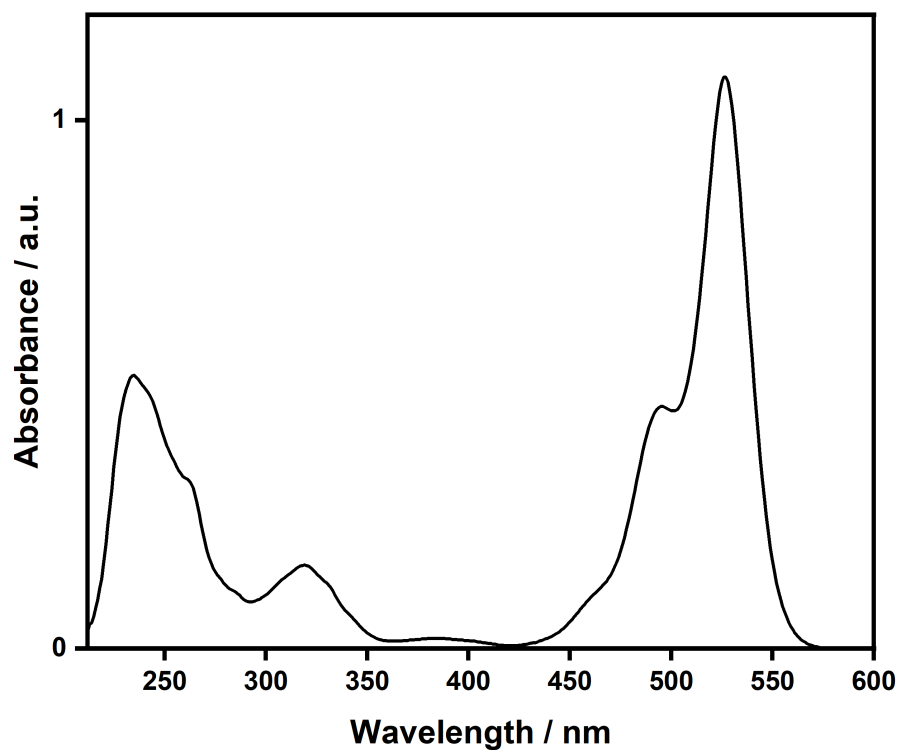
Figure **S23**. UV-vis absorption spectrum of **Eosin Y** in THF.

Due to poor solubility of **Eosin Y** in THF, accurate concentrations could not be determined. As such, ε values are unknown. The UV-vis absorption spectrum of **Eosin Y** was measured in THF simply to confirm the presence of the same structural form of **Eosin Y** in each of THF, DMF and MeCN when comparing redox potentials (see main paper for further discussion).
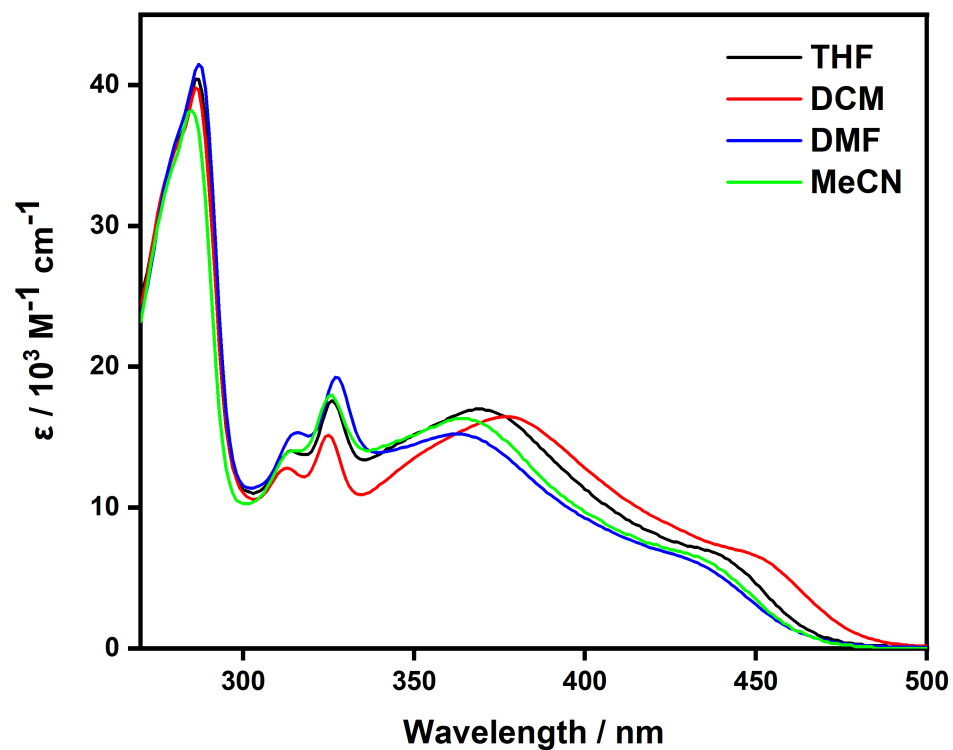
Figure **S24**. UV-vis absorption spectra of **4CzIPN** in the various solvents. Spectra taken from Ref [7].
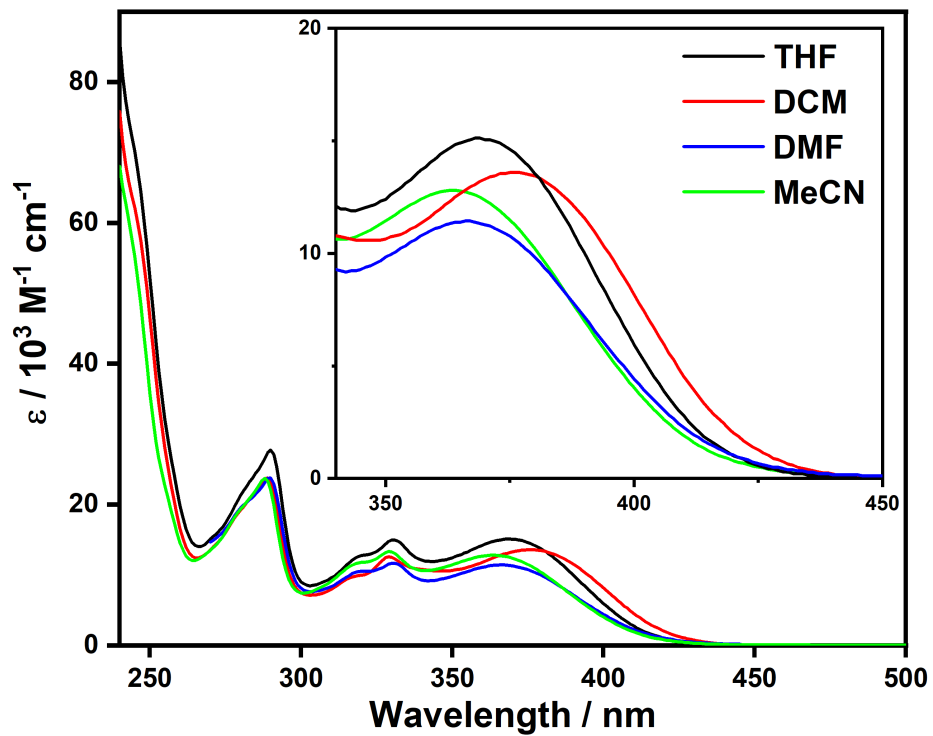
Figure **S25**. UV-vis absorption spectra of **2CzPN** in the various solvents.
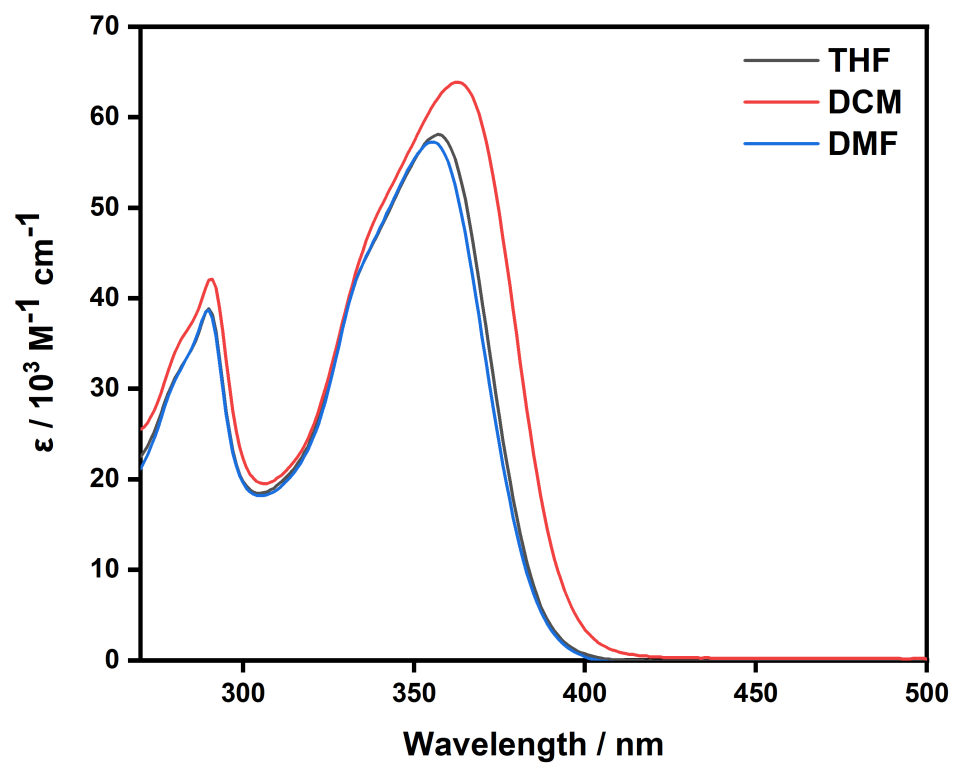
Figure **S26**. UV-vis absorption spectra of **pDTCz-DPmS** in the various solvents. Spectra taken from Ref[7].

Table **S13**. Molar absorptivity values for some of the photocatalysts at 456 nm in the four solvents.[a]

	ε at 456 nm / 10^3 M^{-1} cm^{-1}			
	THF	DCM	DMF	MeCN
[Ru(bpy)$_3$](PF$_6$)$_2$		15.17	15.96	15.72
[Ir(ppy)$_2$(dtbbpy)]PF$_6$	1.22	1.16	0.99	0.80
[Ir(dF(CF$_3$)ppy)$_2$(dtbbpy)]PF$_6$	0.49	0.48	0.50	0.37
[Cu(dmp)(xantphos)]PF$_6$	0.36	0.18	0.20	0.12
Eosin Y			3.28	2.98
4CzIPN	3.06	5.71	1.99	2.18
2CzPN	0	0	0.11	0.07

[a] Measurements performed at room temperature under air. When no value is reported, this is due to poor solubility of the PC in that solvent.

Table **S14**. Molar absorptivity values for some of the photocatalysts at 390 nm in the four solvents.[a]

	ε at 390 nm / 10^3 M^{-1} cm^{-1}			
	THF	DCM	DMF	MeCN
[Ru(bpy)$_3$](PF$_6$)$_2$		5.16	5.65	5.89
[Ir(dF(CF$_3$)ppy)$_2$(dtbbpy)]PF$_6$	5.82	5.63	5.54	5.18
[Cu(dmp)(xantphos)]PF$_6$	3.53	3.55	3.13	2.75
4CzIPN	13.57	14.90	10.90	11.48

[a] Measurements performed at room temperature under air. When no value is reported, this is due to poor solubility of the PC in that solvent.

Steady-state emission spectra
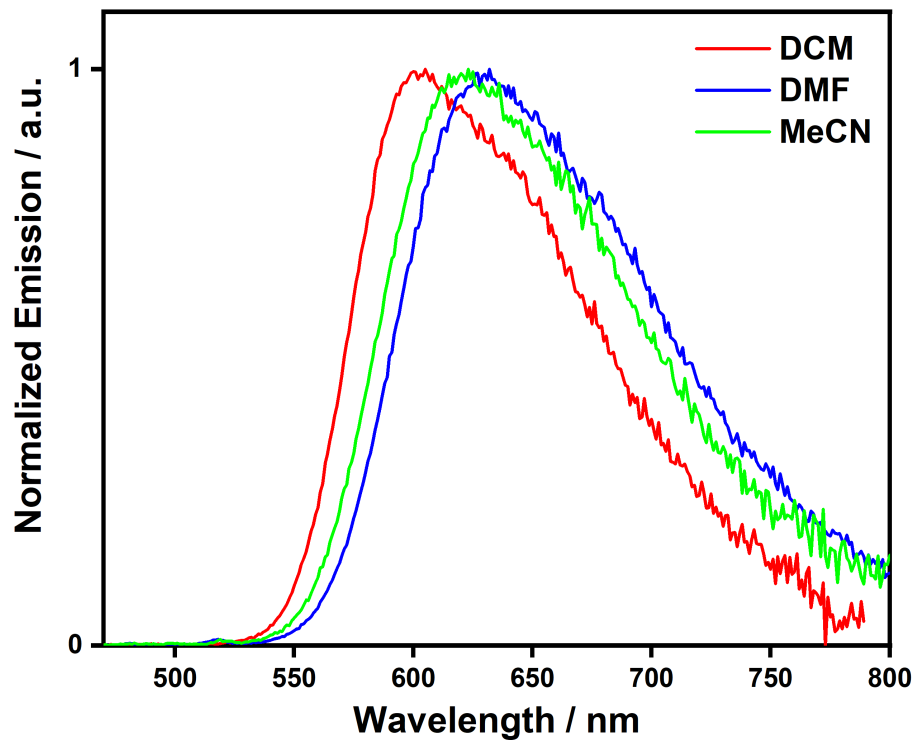
Figure **S27**. Steady-state emission spectra of **[Ru(bpy)₃](PF₆)₂** obtained in the various solvents, where λ_{exc} = 450 nm.
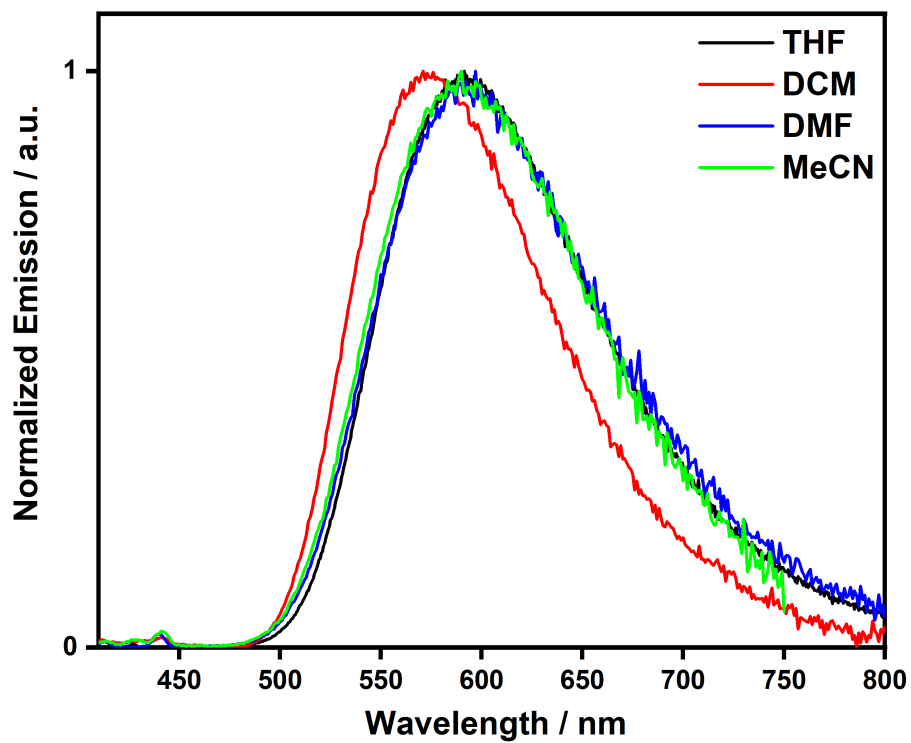
Figure **S28**. Steady-state emission spectra of **[Ir(ppy)₂(dtbbpy)]PF₆** obtained in the various solvents, where λ_{exc} = 380 nm.

Figure **S29**. Steady-state emission spectra of **[Ir(dF(CF$_3$)ppy)$_2$(dtbbpy)]PF$_6$** obtained in the various solvents, where $\lambda_{exc} = 380$ nm.
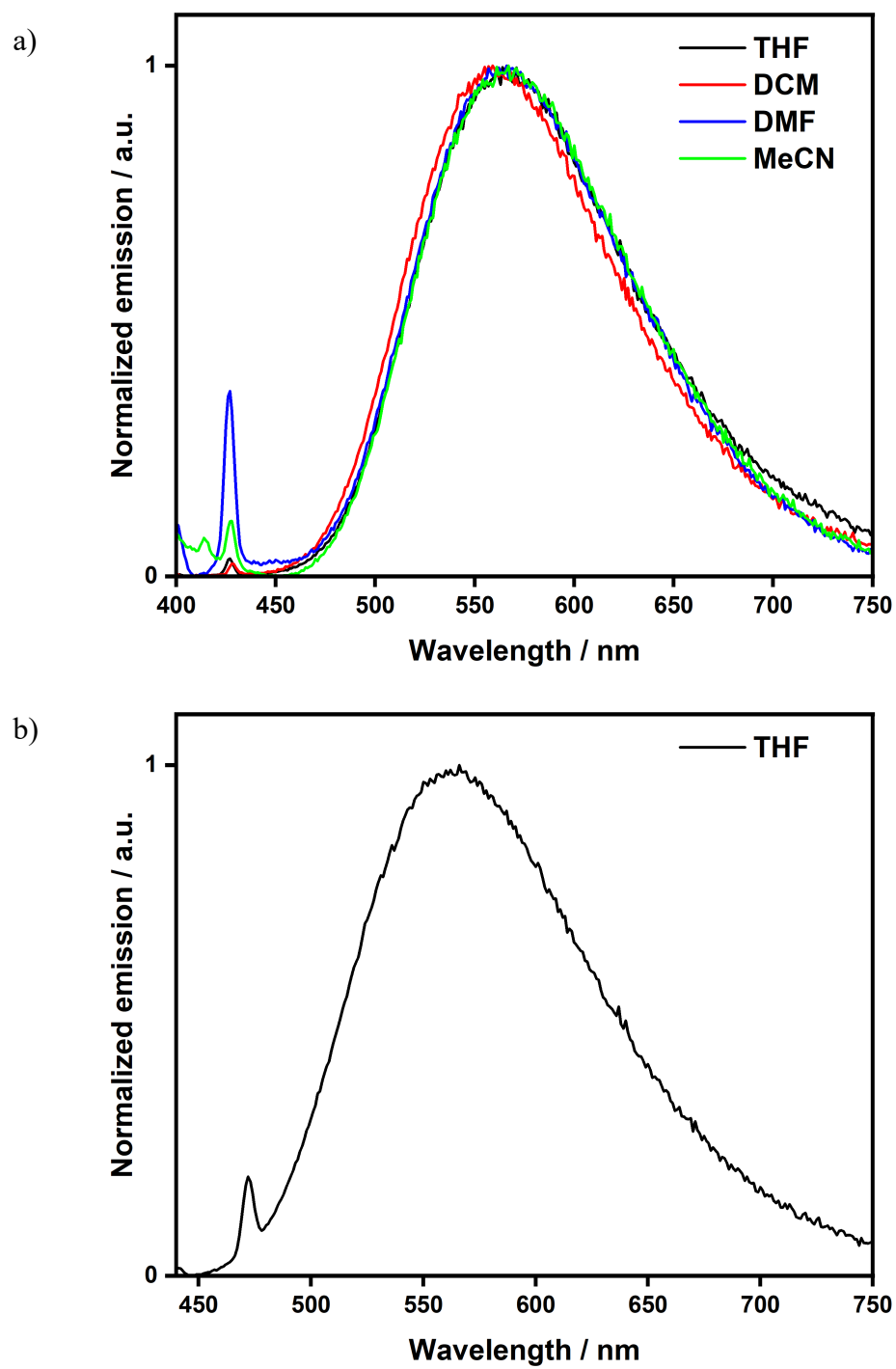
Figure **S30**. Steady-state emission spectra of **[Cu(dmp)(xantphos)]PF$_6$** a) obtained in the various solvents, where λ_{exc} = 380 nm and b) obtained in THF, where λ_{exc} = 415 nm.
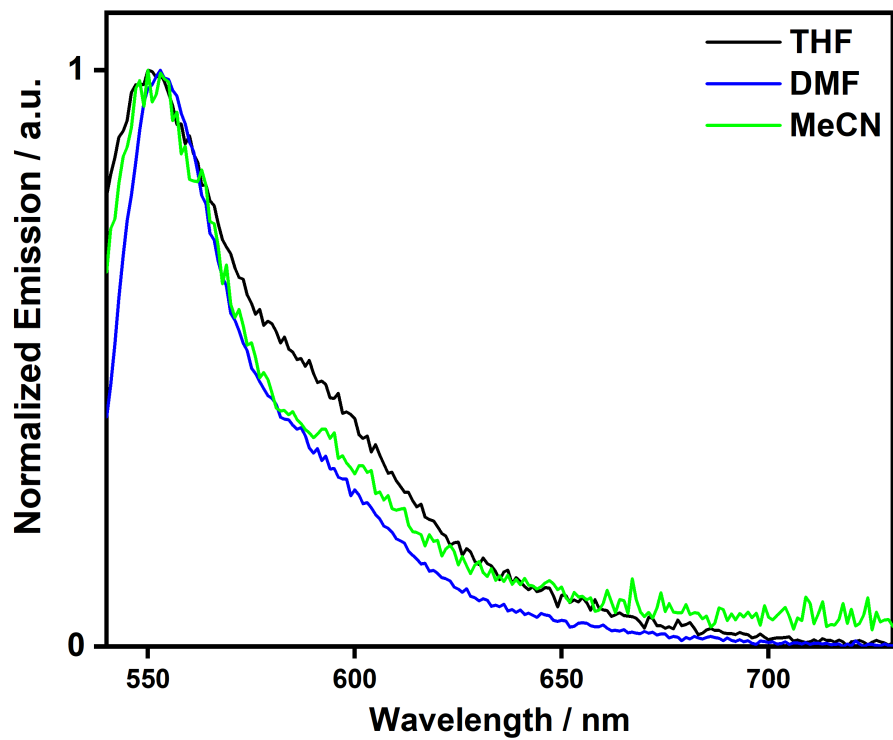
Figure **S31**. Steady-state emission spectra of **Eosin Y** obtained in the various solvents, where λ_{exc} = 520 nm.
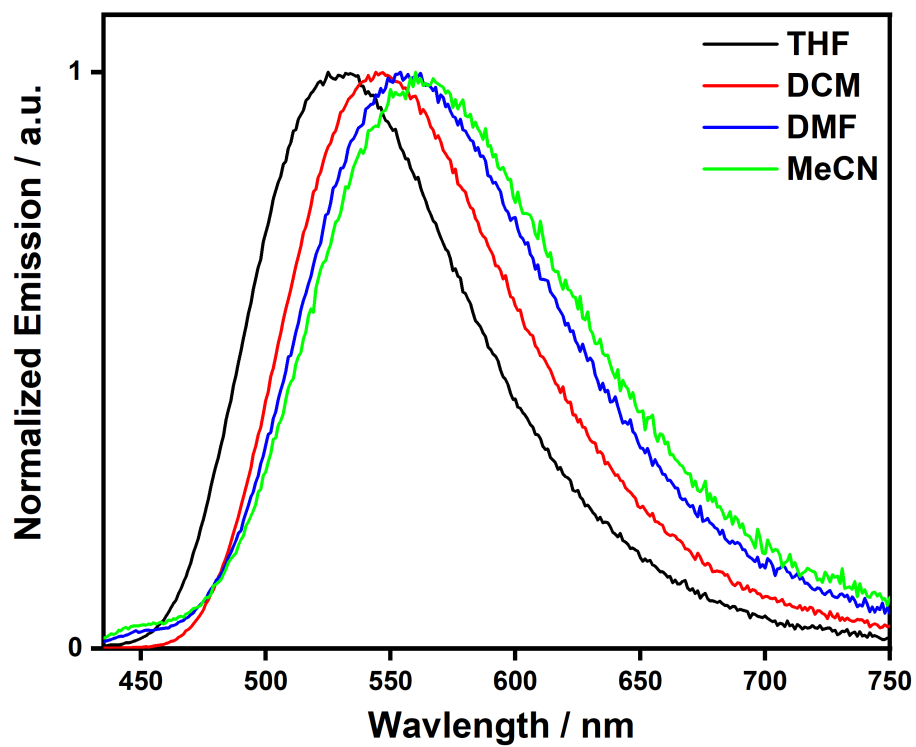
Figure **S32**. Steady-state emission spectra of **4CzIPN** obtained in the various solvents, where λ_{exc} = 420 nm. Spectra taken from Ref [7].
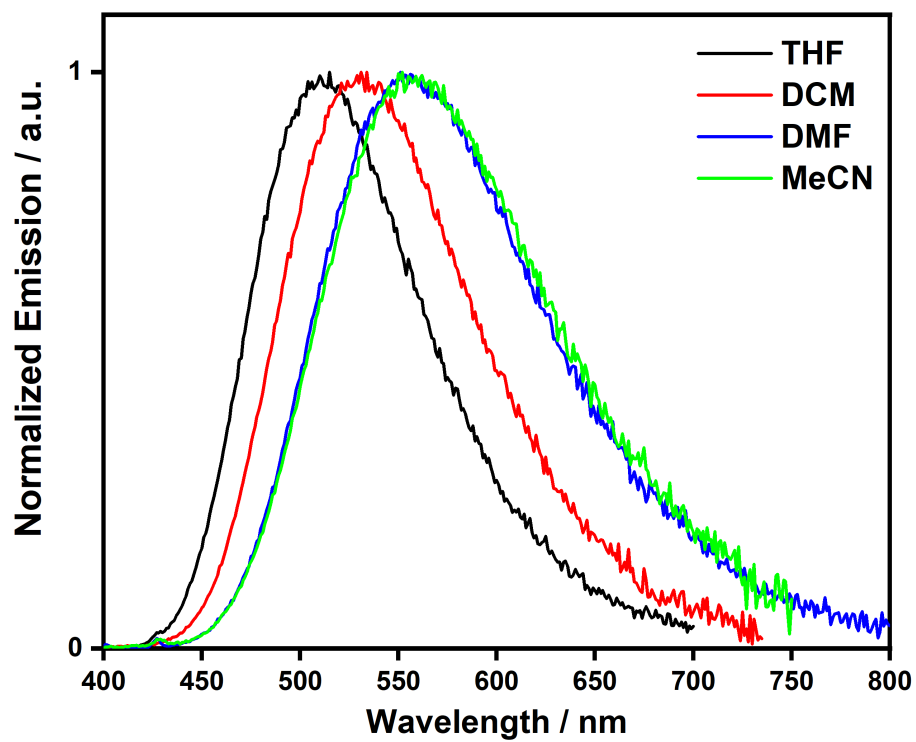
Figure **S33**. Steady-state emission spectra of **2CzPN** obtained in the various solvents, where λ_{exc} = 380 nm.

Figure **S34**. Steady-state emission spectra of **pDTCz-DPmS** obtained in the various solvents, where λ_{exc} = 360 nm. Spectra taken from Ref [7].

Table **S15**. Absorption and emission maxima for the eight PCs across the four solvents.[a]

		THF	DCM	DMF	MeCN
[Ru(bpy)₃][(PF₆)₂]	λ_{abs} [ε] / nm [/10⁻³ M⁻¹ cm⁻¹]		453 [16]	454 [16]	450 [16]
	λ_{PL} / nm		605	632	623 (615)[c]
[Ir(ppy)₂(dtbbpy)]PF₆	λ_{abs} [ε] / nm [/10⁻³ M⁻¹ cm⁻¹]	470 [0.84], 417 [4.1]	470 [0.87], 417 [3.9]	469 [0.67], 417 [3.7]	466 [0.63], 417 [3.2]
	λ_{PL} / nm	592	571	597	590 (591)[e]
[Ir(dF(CF₃)ppy)₂(dtbbpy)]PF₆	λ_{abs} [ε] / nm [/10⁻³ M⁻¹ cm⁻¹]	379 [6.7]	415 [3.9], 382 [6.0]	378 [6.0]	379 [5.6]
	λ_{PL} / nm	472	466	480	475 (470)[f]
[Cu(dmp)(xantphos)]PF₆	λ_{abs} [ε] / nm [/10⁻³ M⁻¹ cm⁻¹]	382 [3.8]	383 [3.4]	379 [3.3]	379 [3.2]
	λ_{PL} / nm	567	559	566	567 (545)[h]
Eosin Y	λ_{abs} [ε] / nm [/10⁻³ M⁻¹ cm⁻¹]			529 [110]	528 [97]
	λ_{PL} / nm	550		553	550 (537)[g]
4CzIPN	λ_{abs} [ε] / nm [/10⁻³ M⁻¹ cm⁻¹]	438 [6.8]	448 [5.9-6.5]	428 [6.2]	434 [6.8]
	λ_{PL} / nm	525	544	554	560 (565)[d]
2CzPN	λ_{abs} [ε] / nm [/10⁻³ M⁻¹ cm⁻¹]	368 [15]	376 [14-16]	366 [11]	363 [13-15]
	λ_{PL} / nm	515	531	551	552 (560)[d]
pDTCz-DPmS [b]	λ_{abs} [ε] / nm [/10⁻³ M⁻¹ cm⁻¹]	357 [62]	363 [60]	355 [56]	
	λ_{PL} / nm	505	524	535	546

[a] Measurements performed at room temperature under air. Absorption maxima reported for the lowest energy absorption band. When no value is reported, this is due to poor solubility of the PC in that solvent. λ_{exc} = 450 nm for **[Ru(bpy)₃](PF₆)₂**, 390 nm for **[Ir(ppy)₂(dtbbpy)]PF₆**, 380 nm for **[Ir(dF(CF₃)ppy)₂(dtbbpy)]PF₆** and **[Cu(dmp)(xantphos)]PF₆** and **2CzPN**, 520 nm for **Eosin Y**, 420 nm for **4CzIPN** and 360 nm for **pDTCz-DPmS**. [b] Values taken from Ref [7]. [c] Value taken from Ref [44]. [d] Value taken from Ref [45]. [e] Value taken from Ref [46]. [f] Value taken from Ref [39]. [g] Value taken from Ref [47] which was obtained in H₂O. [h] Value taken from Ref [40].

Optical gap determination
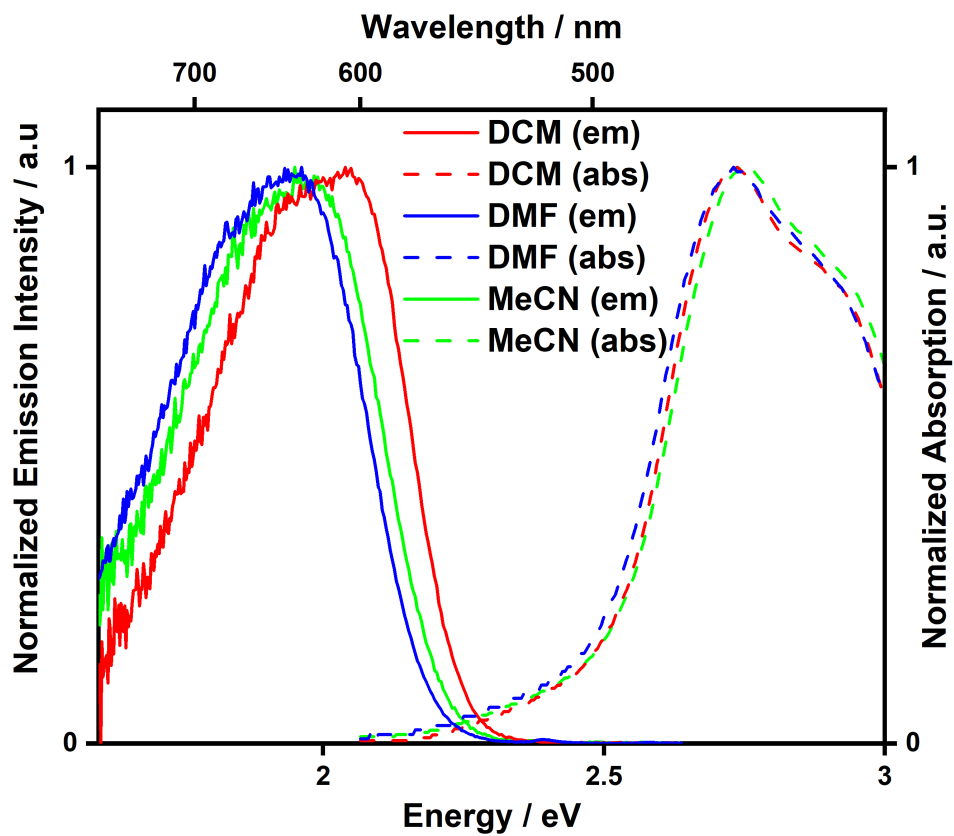
Figure **S35**. Optical gap determination for **[Ru(bpy)₃](PF₆)₂** in various solvents.
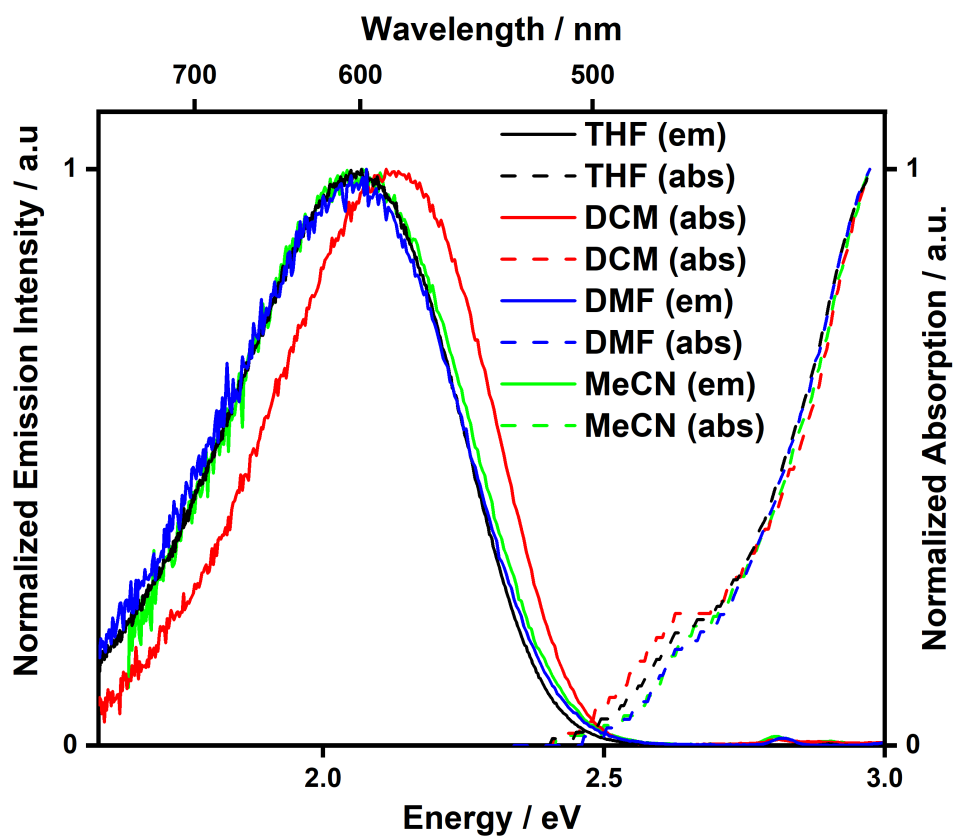
Figure **S36**. Optical gap determination for **[Ir(ppy)₂(dtbbpy)]PF₆** in various solvents.
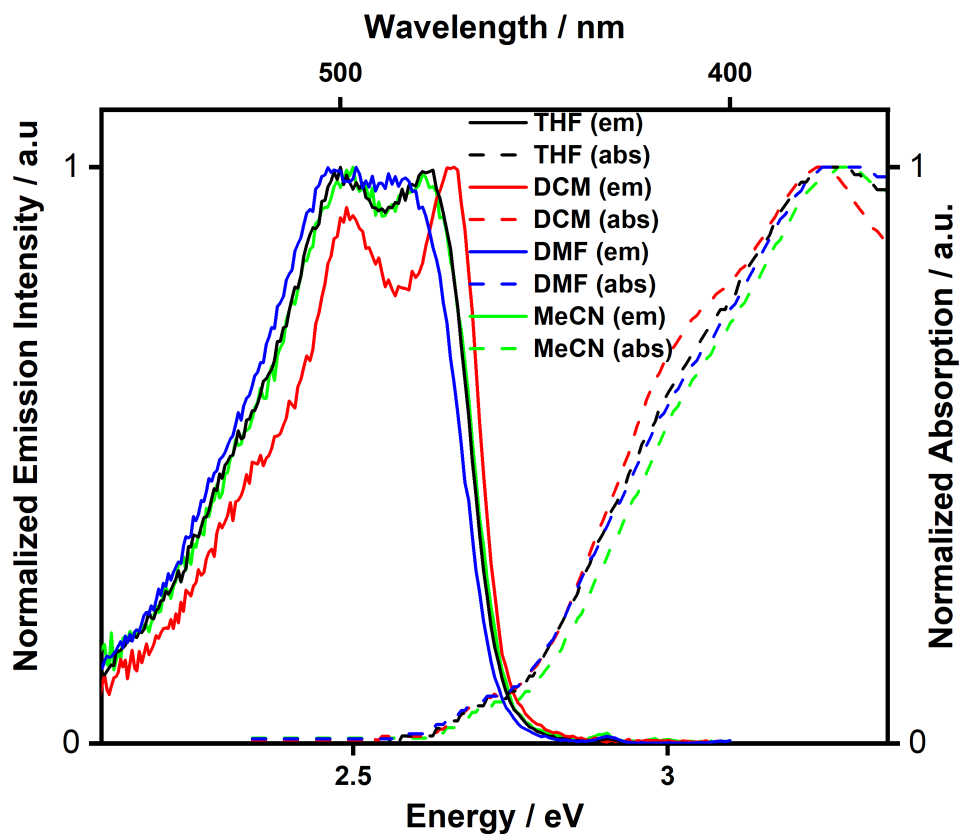
Figure **S37**. Optical gap determination for **[Ir(dF(CF₃)ppy)₂(dtbbpy)]PF₆** in various solvents.
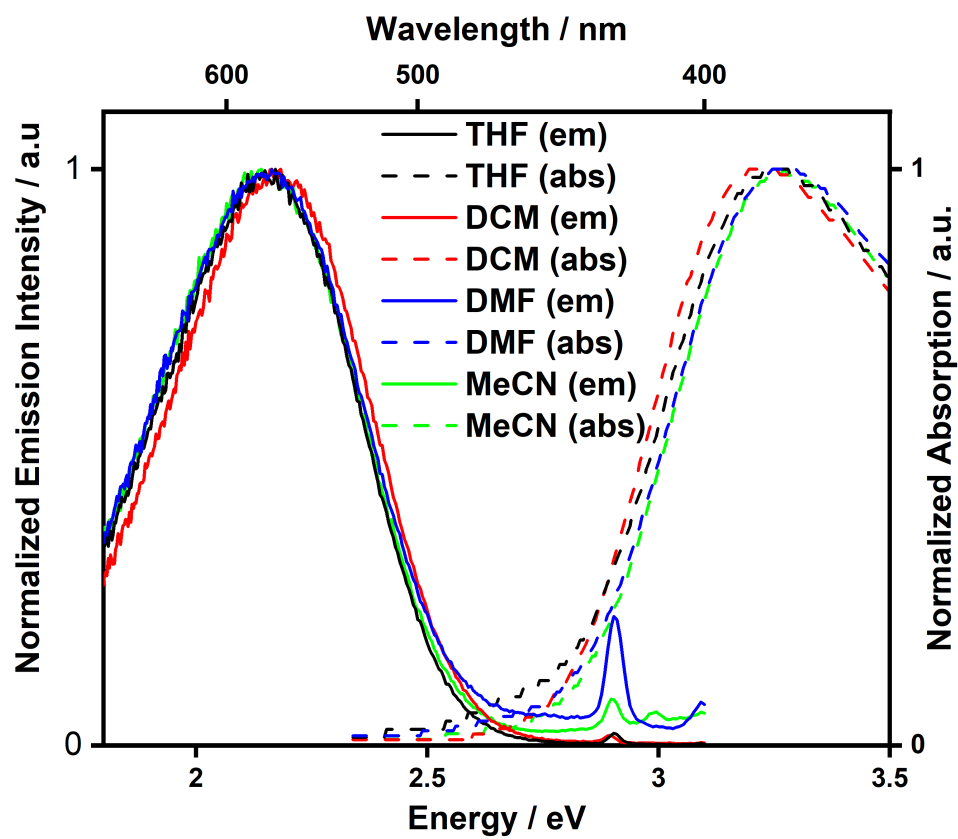
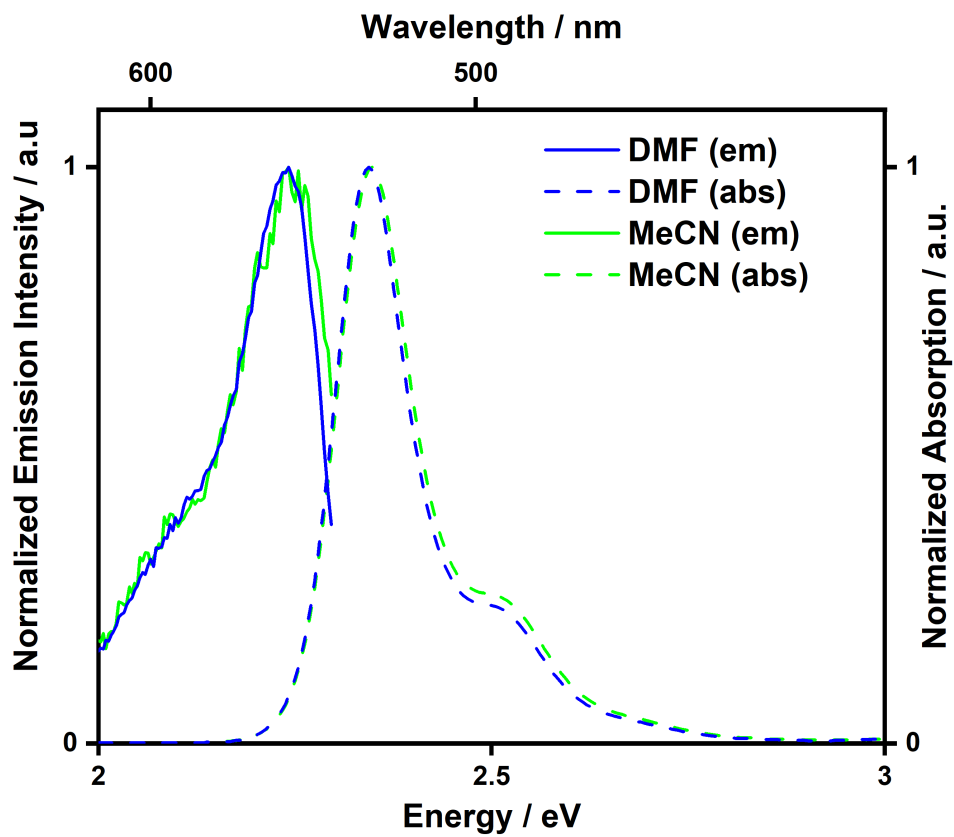Figure **S38**. Optical gap determination for **[Cu(dmp)(xantphos)]PF₆** in various solvents.

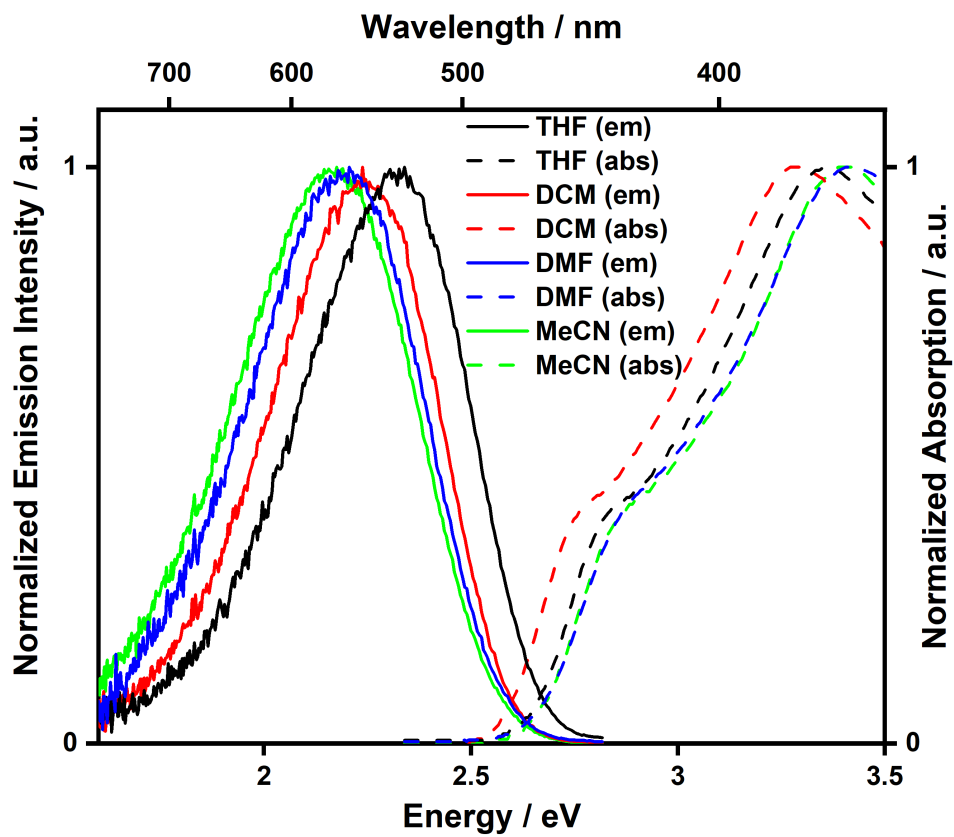Figure **S39**. Optical gap determination for **Eosin Y** in various solvents.

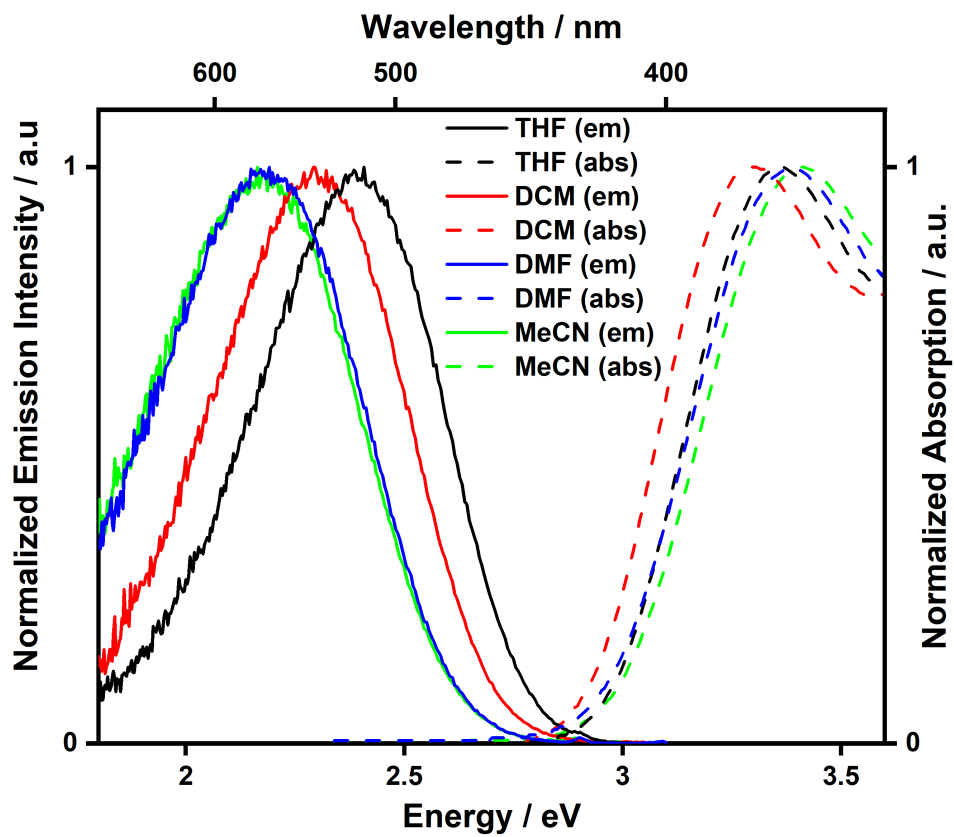Figure **S40**. Optical gap determination for **4CzIPN** in various solvents.

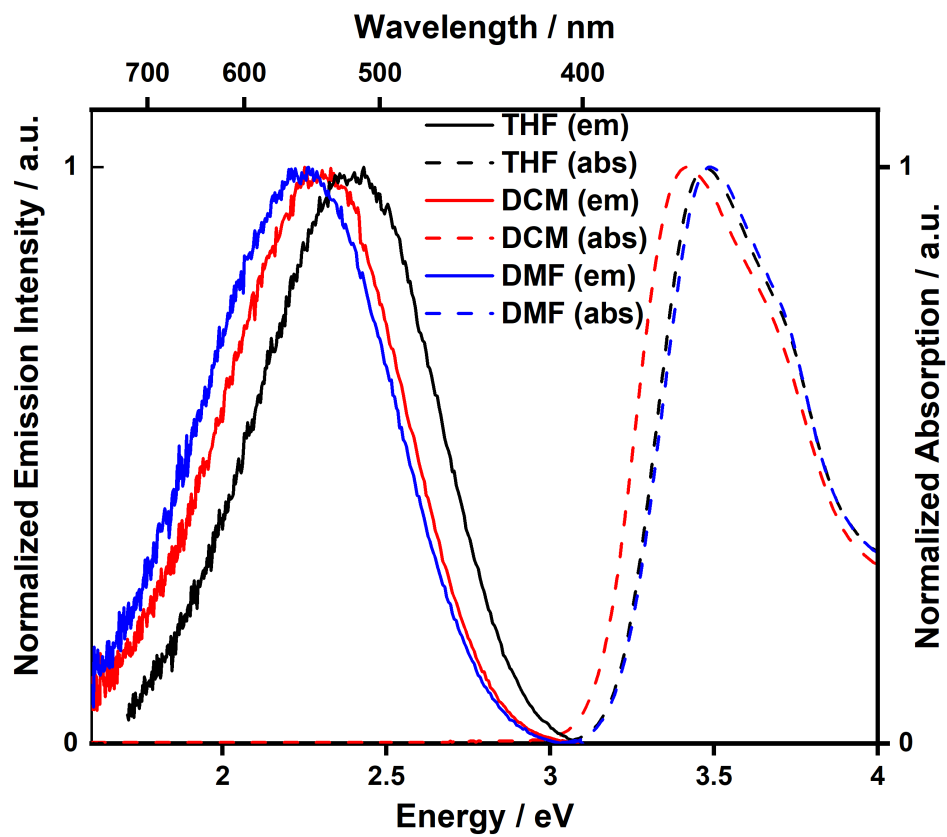Figure **S41**. Optical gap determination for **2CzPN** in various solvents.

Figure **S42**. Optical gap determination for **pDTCz-DPmS** in various solvents.
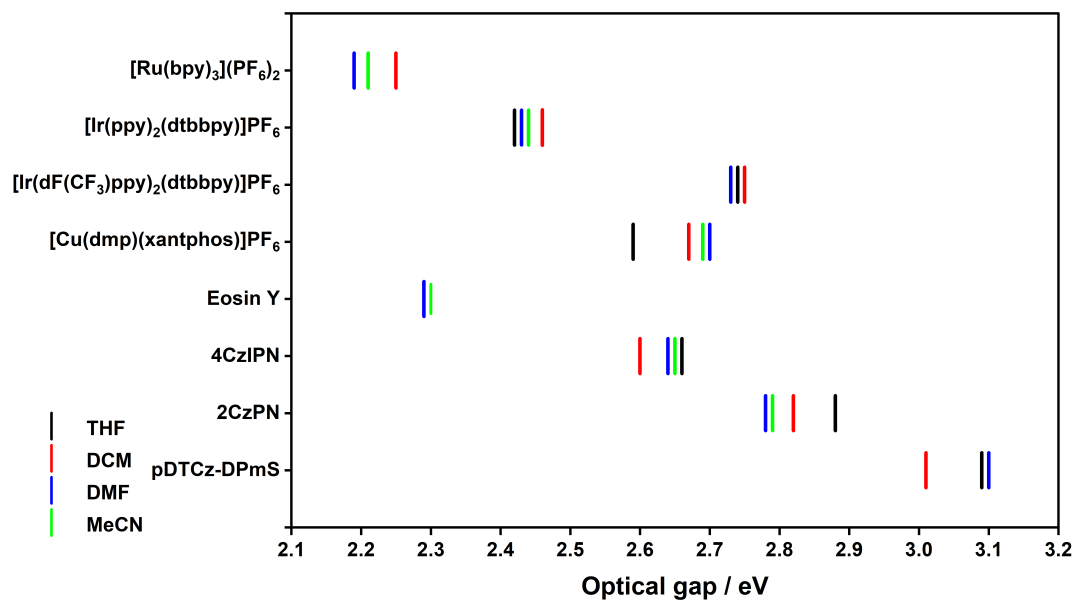
Figure **S43**. Variation of optical gap with solvent for the eight PCs.

Table **S16**. Experimental optical gaps and calculated S_1 and T_1 energies of the eight PCs in the four different solvents.[a]

		THF	DCM	DMF	MeCN
[Ru(bpy)₃]²⁺	$E_{0,0}(T_1)$ / eV		2.25	2.19	2.21
	S_1 / eV	2.63	2.64	2.63	2.63
	T_1 / eV	1.95	1.95	1.92	1.92
[Ir(ppy)₂(dtbbpy)]⁺	$E_{0,0}(T_1)$ / eV	2.42	2.46	2.43	2.44
	S_1 / eV	2.56	2.58	2.65	2.65
	T_1 / eV	2.13	2.13	2.15	2.15
[Ir(dF(CF₃)ppy)₂(dtbbpy)]⁺	$E_{0,0}(T_1)$ / eV	2.74	2.75	2.73	2.74
	S_1 / eV	2.99	3.00	3.06	3.06
	T_1 / eV	2.42	2.43	2.42	2.58
[Cu(dmp)(xantphos)]⁺	$E_{0,0}(S_1)$ / eV	2.59	2.67	2.70	2.69
	S_1 / eV	2.91	2.92	2.95	2.95
	T_1 / eV	1.72	1.80	1.79	1.79
Eosin Y	$E_{0,0}(S_1)$ / eV			2.29	2.30 [b]
	S_1 / eV	4.35	4.35	4.36	4.36
	T_1 / eV	3.07	3.07	3.06	3.06
4CzIPN	$E_{0,0}(S_1)$ / eV	2.66	2.60	2.64	2.65 (2.67) [c]
	S_1 / eV	2.67	2.67	2.68	2.68
	T_1 / eV	2.15	2.11	2.09	2.11
2CzPN	$E_{0,0}(S_1)$ / eV	2.88	2.82	2.78	2.79
	S_1 / eV	2.91	2.92	2.92	2.92
	T_1 / eV	2.18	2.18	2.14	2.14
pDTCz-DPmS	$E_{0,0}(S_1)$	3.09	3.01	3.10	
	S_1 / eV	3.51	3.51	3.52	3.52
	T_1 / eV	2.75	2.51	2.71	2.71

[a] The level of theory used was PBE0/6-31G**/GD3BJ for organic PCs and B3LYP/6-31+G**/SBKJC-VDZ-ECP/GD3BJ for organometallic PCs. S_1 energies were calculated at the TD-DFT level using a state specific solvent correction for the S_1 state[27] and a non-equilibrated solvent environment. T_1 energies were calculated at the vertical delta-SCF level using a fully equilibrated solvent environment. [b] $E_{0,0}$ determined by the average of the onsets of the absorption and emission spectra. [c] Value taken from Ref [42].

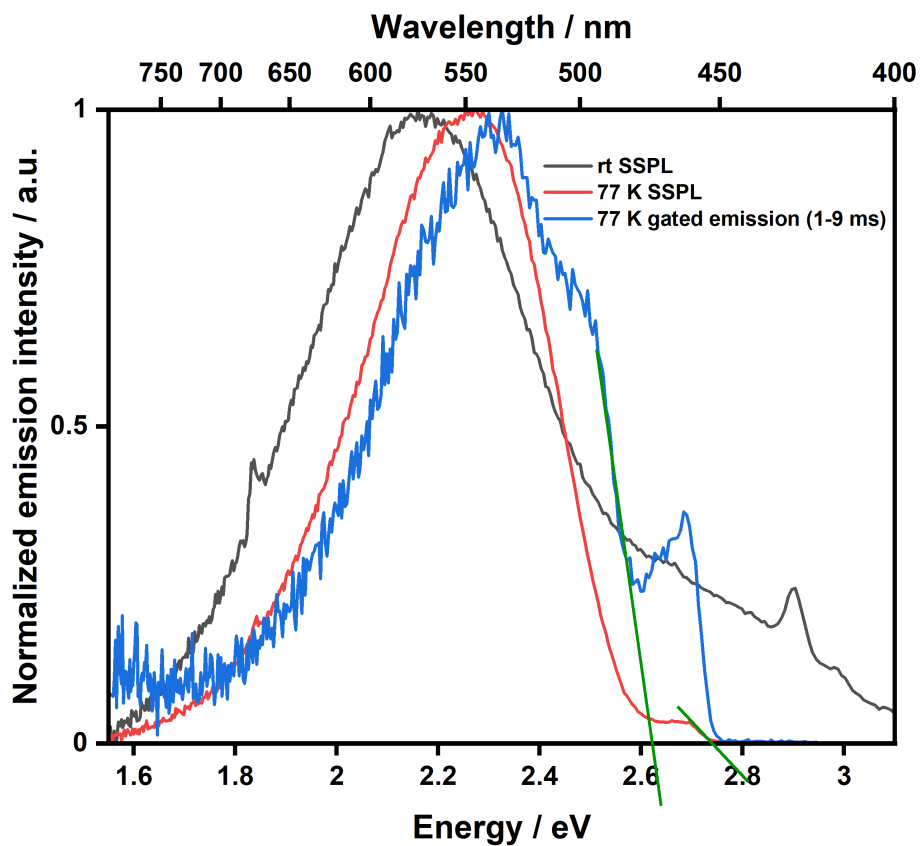**RT steady-state PL and 77 K emission spectra**

Figure **S44**. Steady-state emission spectra obtained for **[Cu(dmp)(xantphos)]PF₆** in BuCN at room temperature and 77 K, and gated emission spectrum at 77 K, employing a 1 - 9 ms time window. In all cases $\lambda_{exc} = 380$ nm.
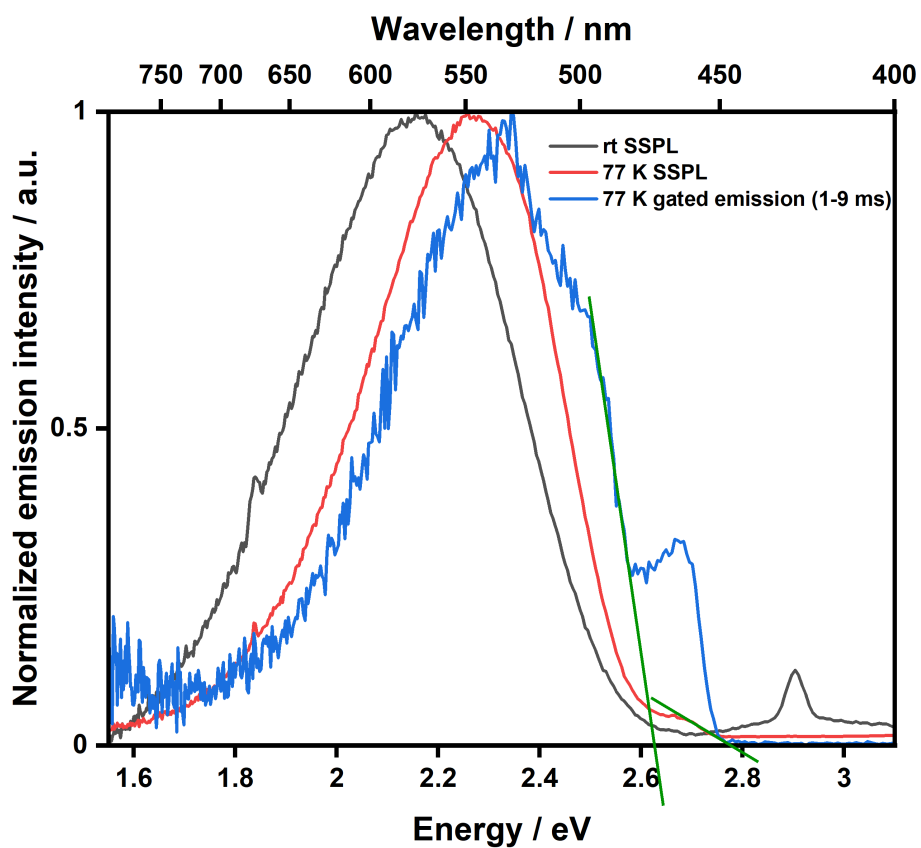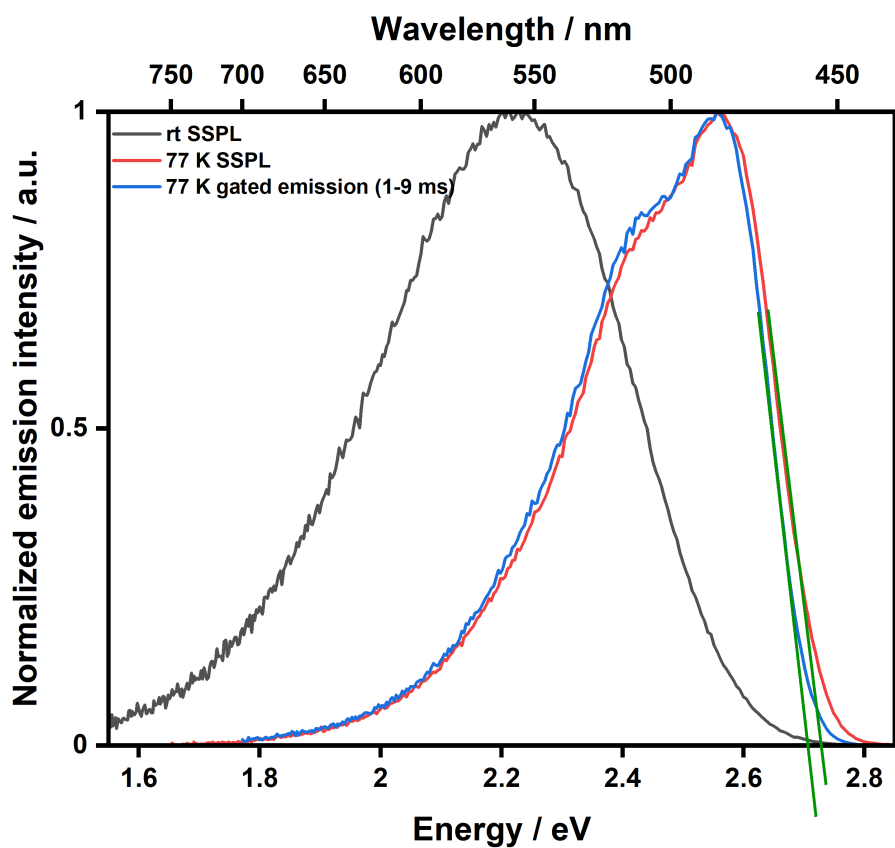
Figure **S45**. Steady-state emission spectra obtained for **[Cu(dmp)(xantphos)]PF₆** in 2-MeTHF at room temperature and 77 K, and gated emission spectrum at 77 K, employing a 1 - 9 ms time window. In all cases λ_{exc} = 380 nm.

Figure **S46**. Steady-state emission spectra obtained for **4CzIPN** in BuCN at room temperature and 77 K, and gated emission spectrum at 77 K, employing a 1 - 9 ms time window. In all cases $\lambda_{exc} = 420$ nm.
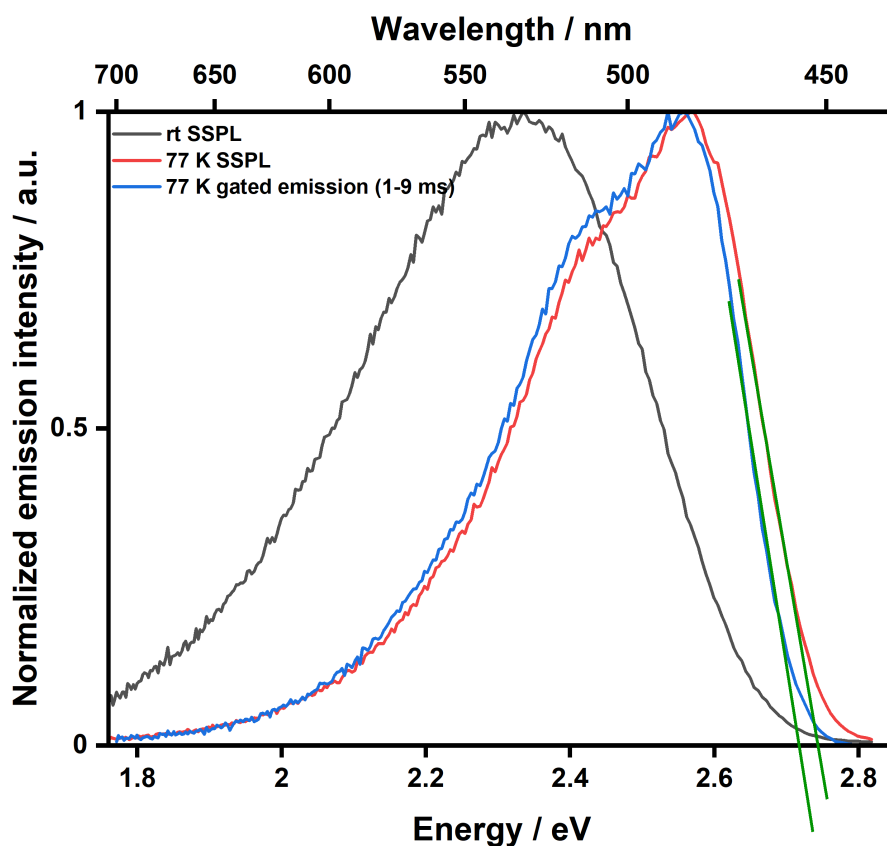
Figure S47. Steady-state emission spectra obtained for **4CzIPN** in 2-MeTHF at room temperature and 77 K, and gated emission spectrum at 77 K, employing a 1 - 9 ms time window. In all cases λ_{exc} = 420 nm.

Table S17. Energy values for the S_1 and T_1 states of **[Cu(dmp)(xantphos)]PF$_6$** and **4CzIPN**.[a]

	2-MeTHF			BuCN			Average
	S_1 / eV	T_1 / eV	ΔE_{ST} / eV	S_1 / eV	T_1 / eV	ΔE_{ST} / eV	ΔE_{ST} / eV
[Cu(dmp)(xantphos)]PF$_6$	2.79	2.62	0.17	2.75	2.61	0.14	0.16
4CzIPN	2.75	2.72	0.03	2.74	2.71	0.03	0.03

[a] S_1 energies estimated from the high-energy tangential onset from the 77 K steady-state emission spectra. T_1 energies estimated from the tangent from the 77 K gated emission spectra (employing 1 – 9 ms time window). $\Delta E_{ST} = T_1 - S_1$.
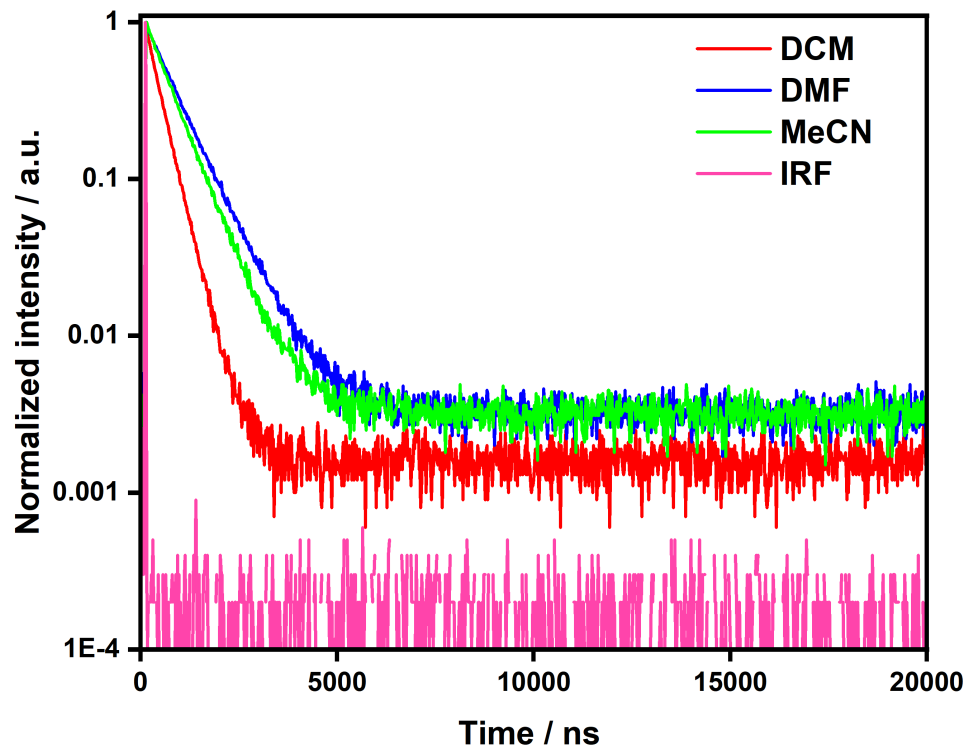
Time resolved emission spectra

Figure **S48**. Time-resolved PL decays of **[Ru(bpy)$_3$](PF$_6$)$_2$** recorded in various solvents under N$_2$ in 10^{-5} M solutions with λ_{exc} = 378 nm. No data obtained in THF due poor solubility.
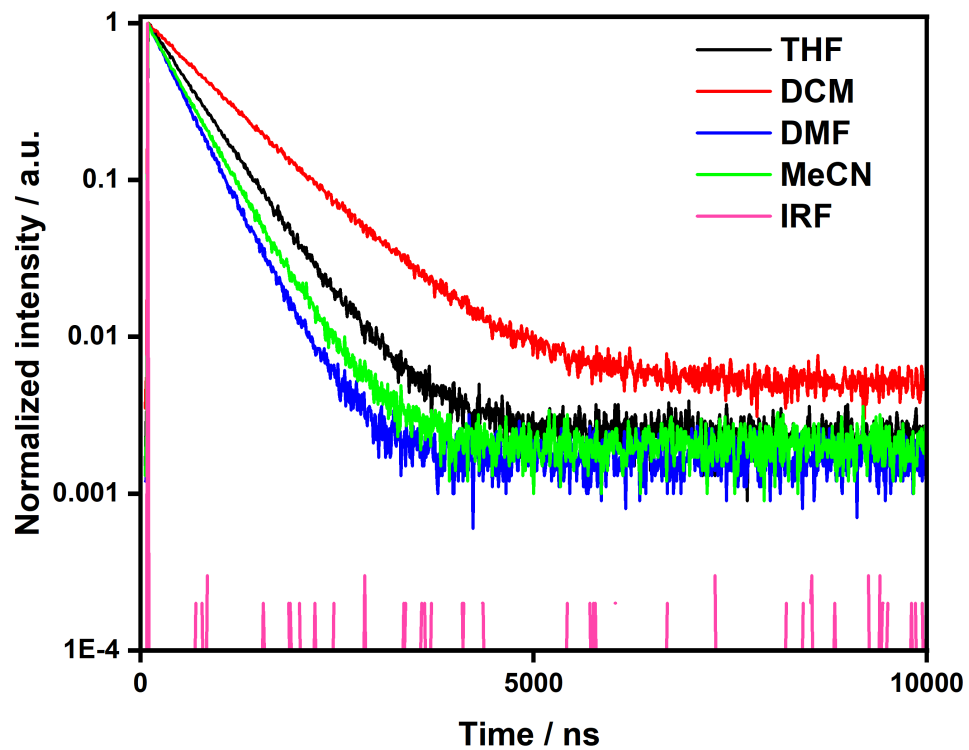
Figure **S49**. Time-resolved PL decays of **[Ir(ppy)₂(dtbbpy)]PF₆** recorded in various solvents under N_2 in 10^{-5} M solutions with $\lambda_{exc} = 378$ nm.
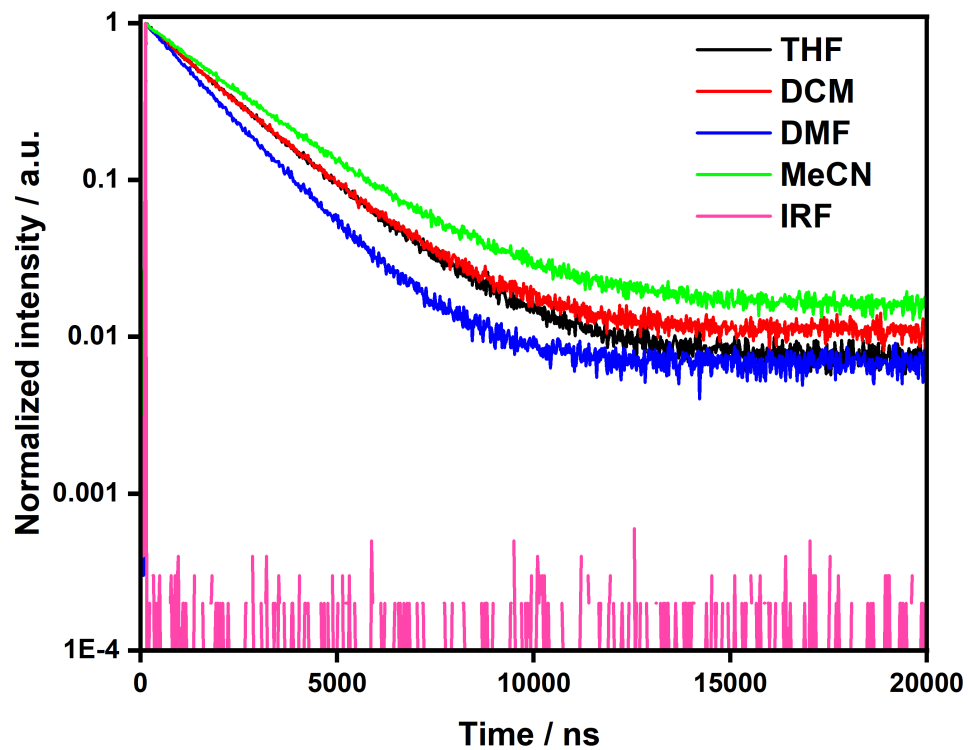
Figure **S50**. Time-resolved PL decays of **[Ir(dF(CF$_3$)ppy)$_2$(dtbbpy)]PF$_6$** recorded in various solvents under N$_2$ in 10^{-5} M solutions with λ_{exc} = 378 nm.
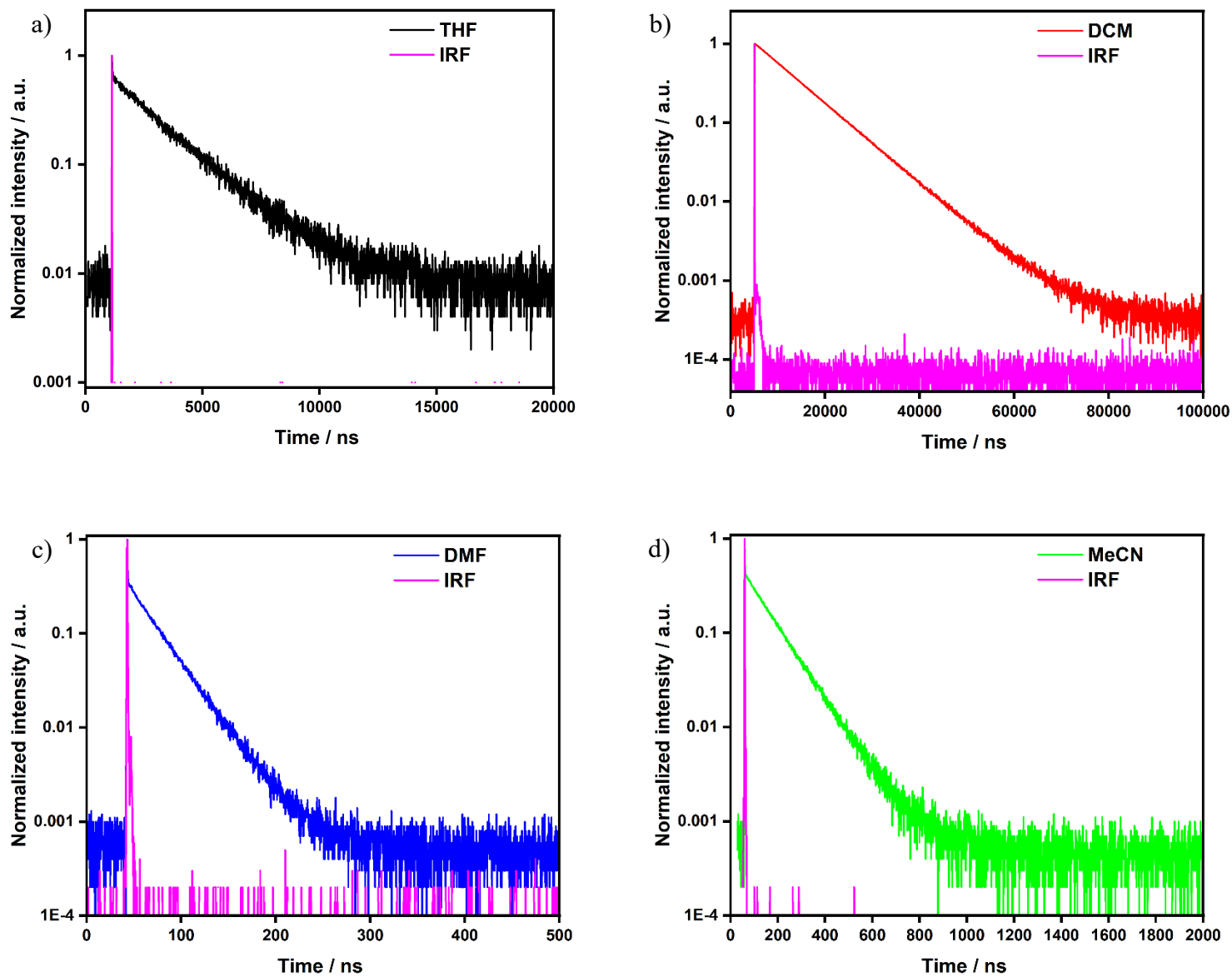
Figure **S51**. Time-resolved PL decays of **[Cu(dmp)(xantphos)]PF$_6$** recorded in a) THF, b) DCM, c) DMF and d) MeCN under N$_2$ in 10^{-5} M solutions with λ_{exc} = 378 nm. Due to different time windows being required for different solvents, multiple IRFs are given.
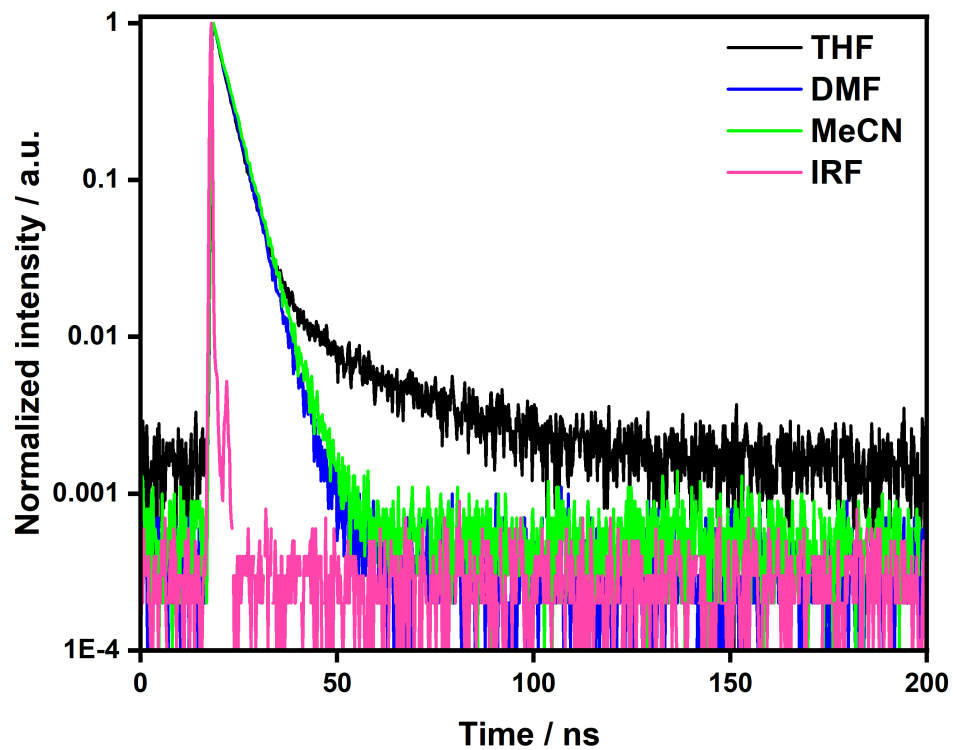
Figure **S52**. Time-resolved PL decays of **Eosin Y** recorded in various solvents under N_2 in 10^{-5} M solutions with $\lambda_{exc} = 378$ nm.
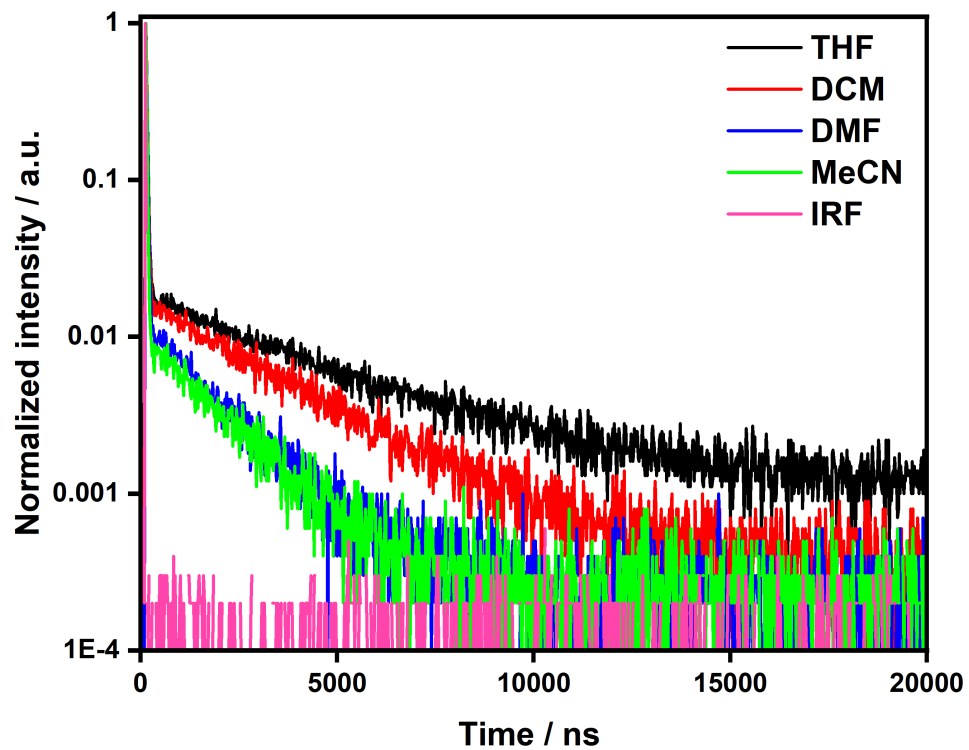
Figure **S53**. Time-resolved PL decays of **4CzIPN** recorded in various solvents under N_2 in 10^{-5} M solutions with $\lambda_{exc} = 378$ nm.

Table **S18**. Excited-state lifetimes of the PCs in the different solvents.[a]

	τ_{PL} / ns			
	THF	DCM	DMF	MeCN
[Ru(bpy)₃](PF₆)₂		390	784	665 (825)[b]
[Ir(ppy)₂(dtbbpy)]PF₆	582	896	430	488 (386)[c]
[Ir(dF(CF₃)ppy)₂(dtbbpy)]PF₆	2014	2007	1597	2311 (2300)[d]
[Cu(dmp)(xantphos)]PF₆	2234	8513 (1133)[g]	29.5	111
Eosin Y	τ_p: 3.64 τ_d: 23.4		τ_p: 4.06 τ_d: 25	τ_p: 4.27 (2.10)[e] τ_d: 10
4CzIPN	τ_p: 30 τ_d: 4010	τ_p: 24.3 τ_d: 2910	τ_p: 22 τ_d: 1640	τ_p: 13.5 (18.7)[f] τ_d: 1650 (1390)[f]

[a] Lifetimes determined under N_2 at room temperature using λ_{exc} = 378 nm. τ_p and τ_d refer to the prompt and delayed lifetimes, respectively. When no value is reported, this is due to poor solubility of the PC in that solvent. Values in parentheses indicate literature values and are referenced accordingly. [b] Value taken from Ref [44] using λ_{exc} = 450 or 500 nm laser. It is not clearly identified which excitation wavelength was used. [c] Value taken from Ref [46] using λ_{exc} = 341 nm. [d] Value taken from Ref [39] using λ_{exc} = 337 nm. [e] Value taken from Ref [48] using λ_{exc} = 475 nm and was obtained in MeOH. [f] Value taken from Ref [49] using λ_{exc} = 365 nm. [g] Value taken from Ref [50] using **[Cu(dmp)(xantphos)]BF₄** and using λ_{exc} = 375 nm.

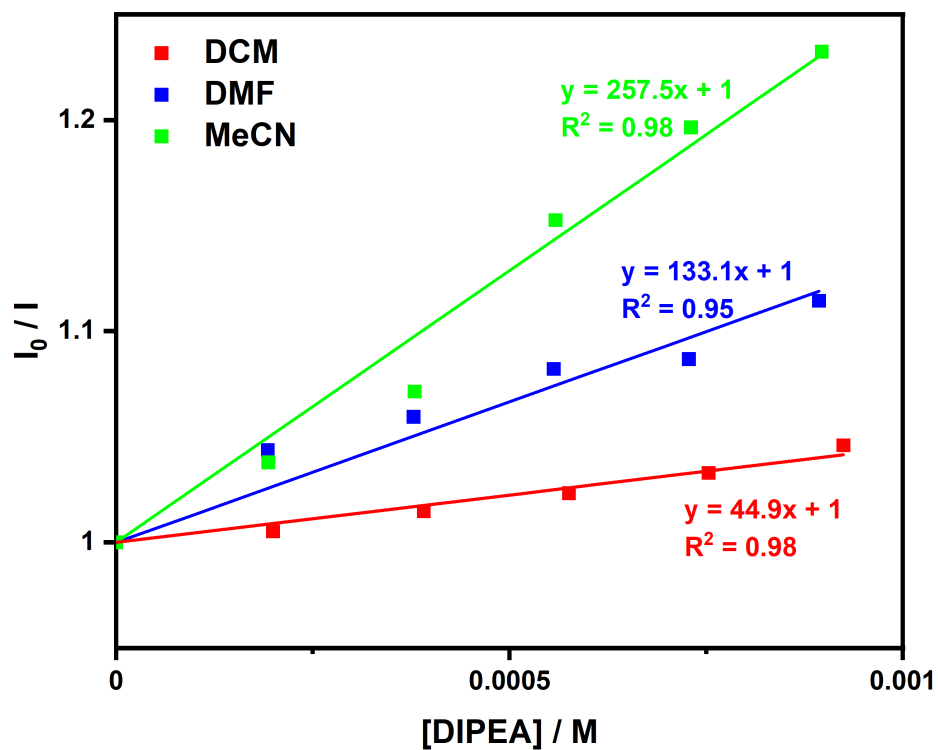**Stern-Volmer quenching studies**

Figure **S54**. Stern Volmer quenching plot for **[Ru(bpy)₃](PF₆)₂** in various solvents with DIPEA. No values obtained in THF due to poor solubility.
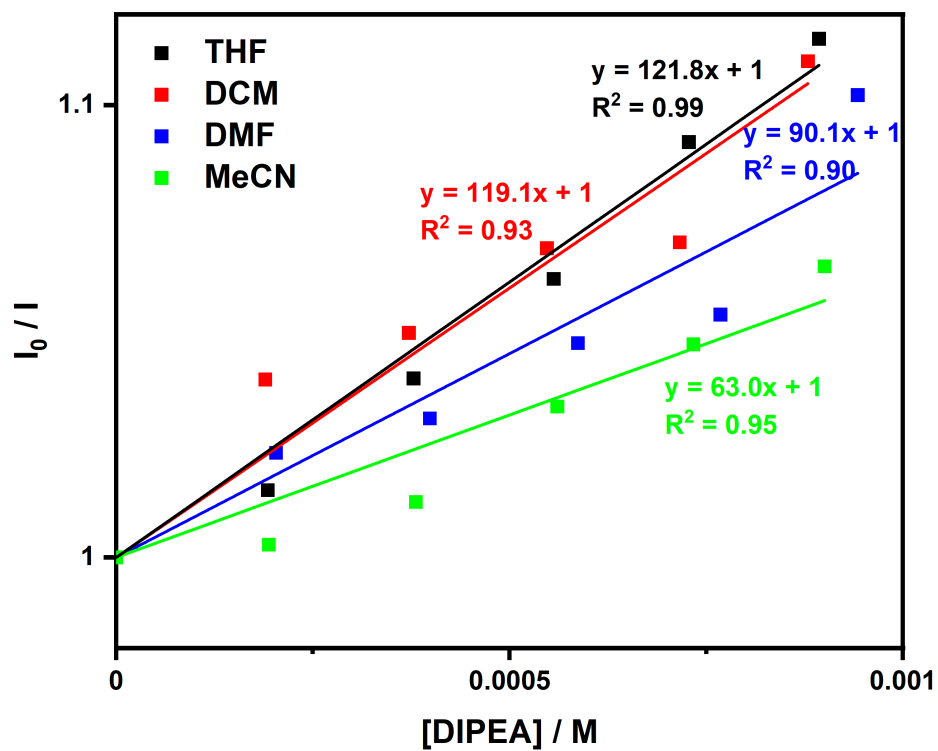
Figure **S55**. Stern Volmer quenching plot for **[Ir(ppy)₂(dtbbpy)]PF₆** in various solvents with DIPEA.
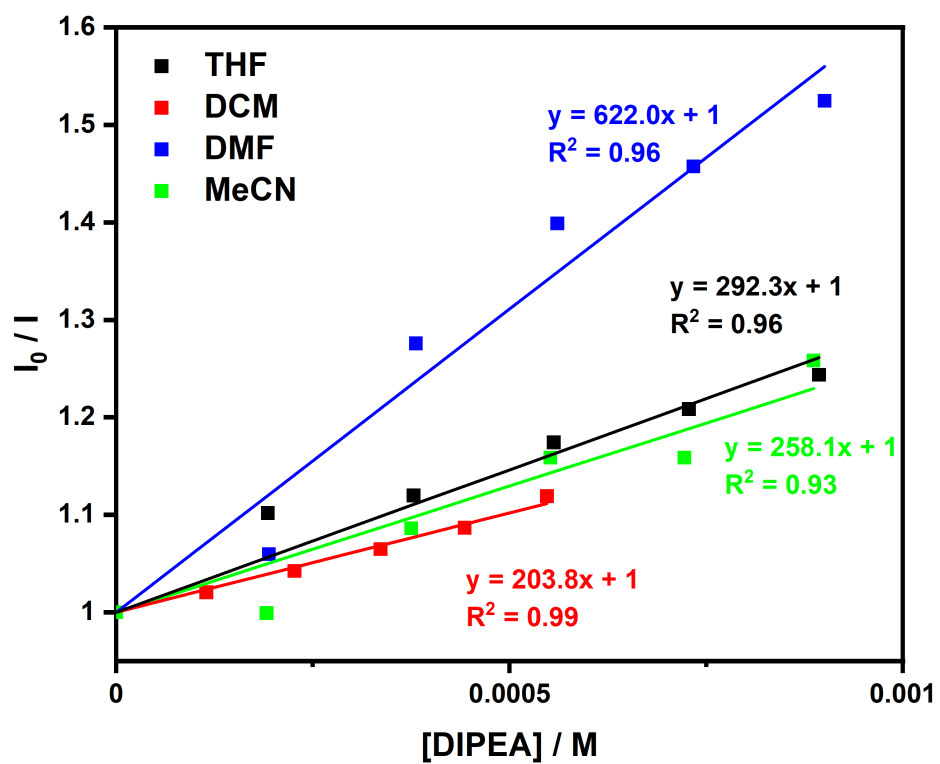
Figure **S56**. Stern Volmer quenching plot for **[Ir(dF(CF$_3$)ppy)$_2$(dtbbpy)]PF$_6$** in various solvents with DIPEA.
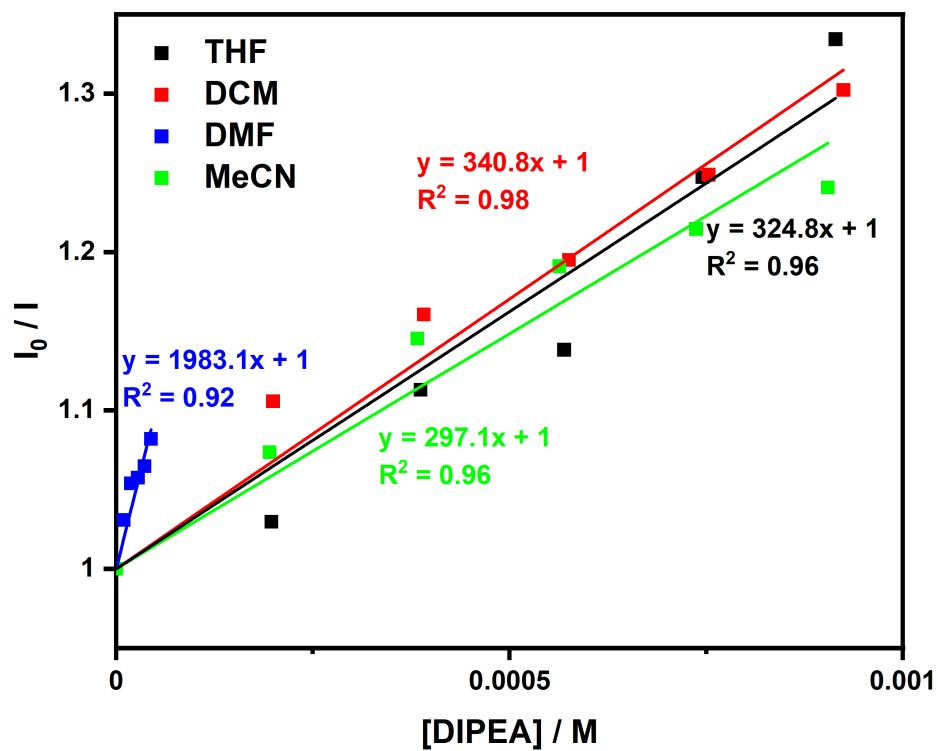
Figure **S57**. Stern Volmer quenching plot for **[Cu(dmp)(xantphos)]PF₆** in various solvents with DIPEA.

A lower concentration of DIPEA had to be used with **[Cu(dmp)(xantphos)]PF₆** in DMF to avoid observing a saturation of the quenching.
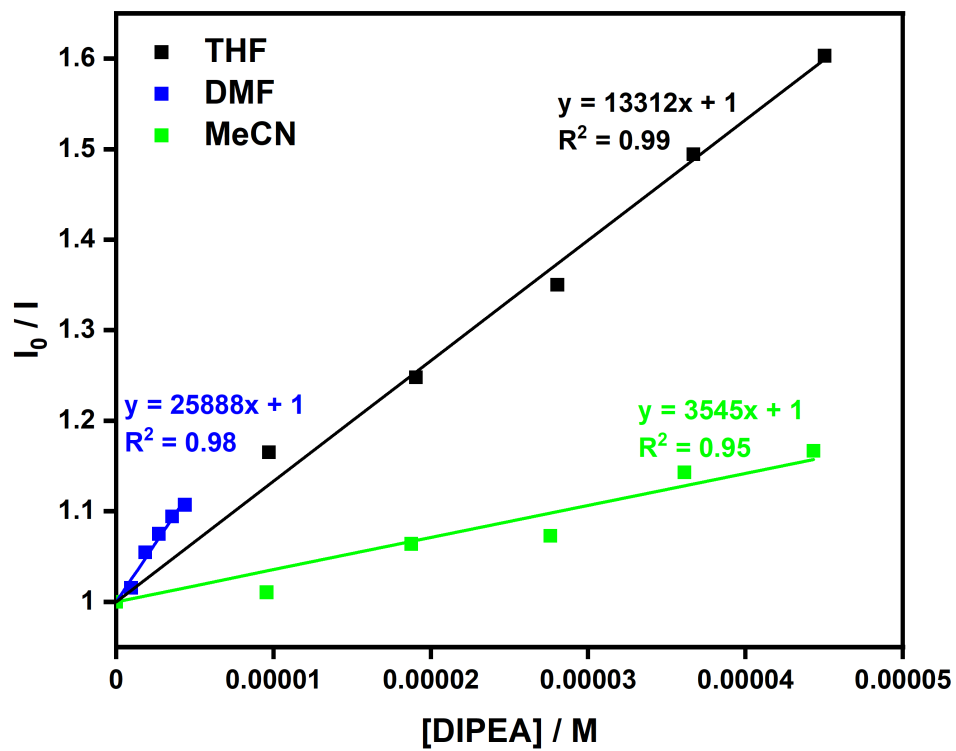
Figure **S58**. Stern Volmer quenching plot for **Eosin Y** in various solvents with DIPEA. No values obtained in DCM due to poor solubility.
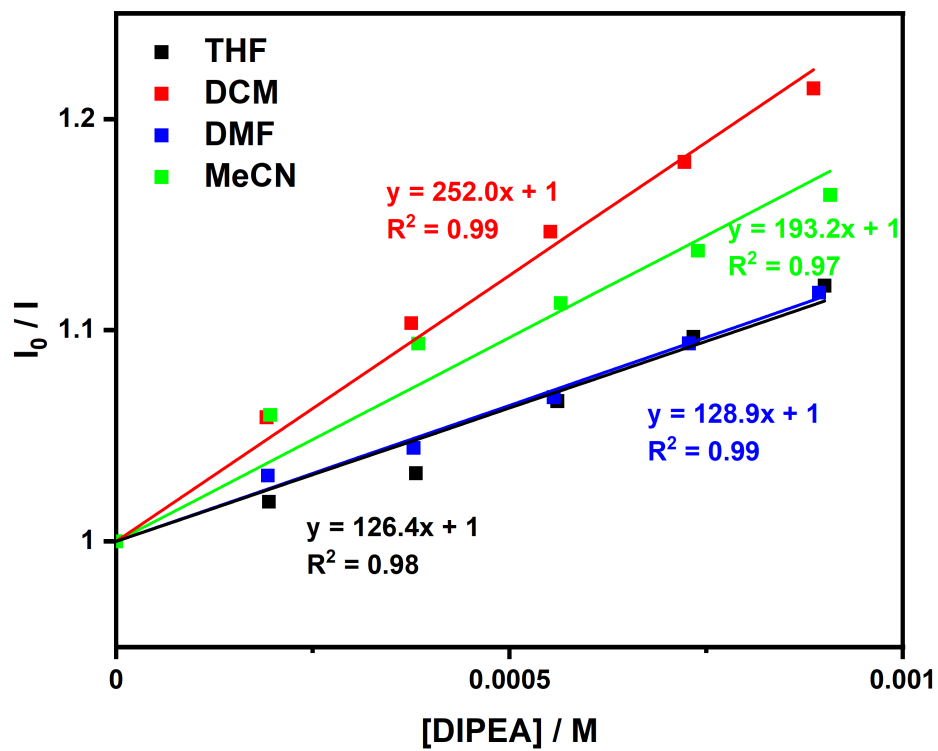
Figure **S59**. Stern Volmer quenching plot for **4CzIPN** in various solvents with DIPEA.

Table **S19**. Stern Volmer quenching constants for the PCs in various solvents using DIPEA as the quencher.[a]

	K_{SV}			
	THF	DCM	DMF	MeCN
[Ru(bpy)₃](PF₆)₂		44.9	133.1	257.5
[Ir(ppy)₂(dtbbpy)]PF₆	121.8	119.1	90.1	63.0
[Ir(dF(CF₃)ppy)₂(dtbbpy)]PF₆	292.3	203.8	622.0	258.1
[Cu(dmp)(xantphos)]PF₆	324.8	340.8	1983.1	297.1
Eosin Y	13312		25888	3545
4CzIPN	126.4	252.0	128.9	193.2

[a] Stern-Volmer quenching studies conducted under N_2. When no value is reported, this is due to poor solubility of the PC in that solvent.

Table **S20**. Quenching rates constants for the PCs in various solvents using DIPEA as the quencher.[a]

	k_q / 10^7 M^{-1} s^{-1}			
	THF	DCM	DMF	MeCN
[Ru(bpy)₃](PF₆)₂		11.5	17.0	38.7
[Ir(ppy)₂(dtbbpy)]PF₆	20.9	13.3	21.0	12.9
[Ir(dF(CF₃)ppy)₂(dtbbpy)]PF₆	14.5	10.2	38.9	11.2
[Cu(dmp)(xantphos)]PF₆	14.5	4.00	6720	268
Eosin Y	3.66×10^5 [b]		6.38×10^5 [b]	0.83×10^5 [b]
	0.569×10^5 [c]		1.04×10^5 [c]	0.355×10^5 [c]
4CzIPN	421 [b]	1040 [b]	586 [b]	1430 [b]
	3.15 [c]	8.66 [c]	7.86 [c]	11.7 [c]

[a] Stern-Volmer quenching studies conducted under N_2. When no value is reported, this is due to poor solubility of the PC in that solvent. [b] Determined using τ_p values given in Table **S18**. [c] Determined using τ_d values given in Table **S18**.
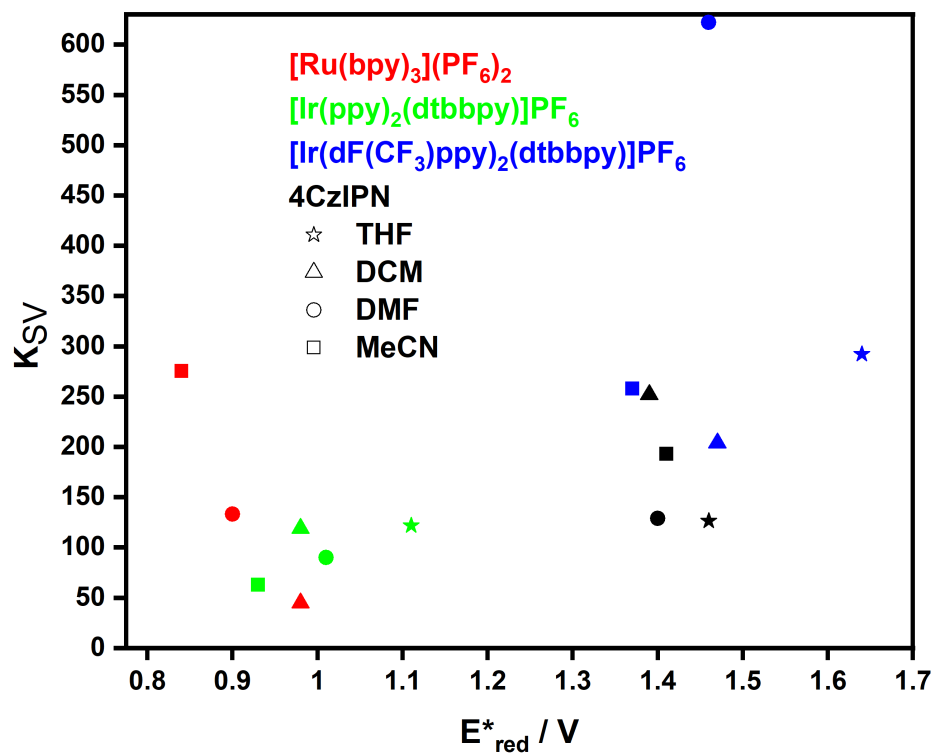
Figure S60. Comparison of the E*_{red} values with the Stern-Volmer constants obtained using DIPEA for some of the PCs. Star = THF, triangle = DCM, circle = DMF and square = MeCN.

Photostability studies

For the photostability studies, the reaction mixture was prepared according to the experimental procedure. Once prepared, a 20 μL (pinacol coupling, ATRA reaction, 2+2 cycloaddition), 15 μL (*E/Z* isomerisation) or 80 μL (Giese type addition) aliquot was removed from the reaction and diluted in 1 mL of the relevant solvent and a UV-vis absorption spectrum was obtained. The reaction mixture was irradiated in the photoreactor using the 456 nm or 390 nm Kessil lamp for 24 h, as dictated in the experimental procedure. Upon completion, a 20 μL (pinacol coupling, ATRA reaction, 2+2 cycloaddition), 15 μL (*E/Z* isomerisation) or 80 μL (Giese type addition) aliquot was taken, diluted in 1 mL with the relevant solvent and a UV-vis absorption spectrum was recorded. In all cases, the UV-vis absorption spectra are normalized with respect to the highest energy band unless otherwise noted.
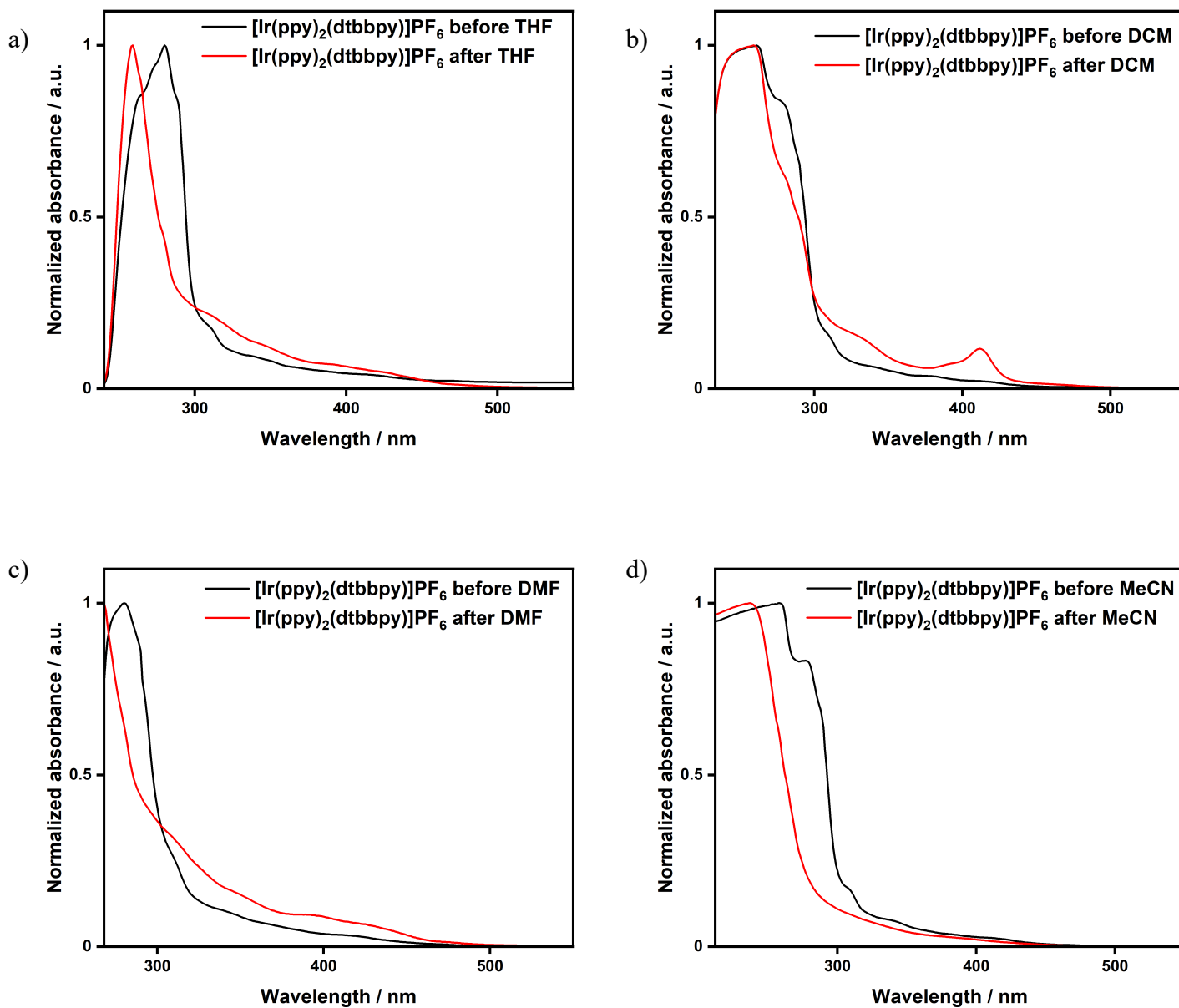
Pinacol coupling:

Figure **S61** . UV-vis absorption spectra before and after irradiation for the pinacol coupling using **[I(ppy)₂(dtbbpy)]PF₆** as the PC in a) THF, b) DCM, c) DMF and d) MeCN.

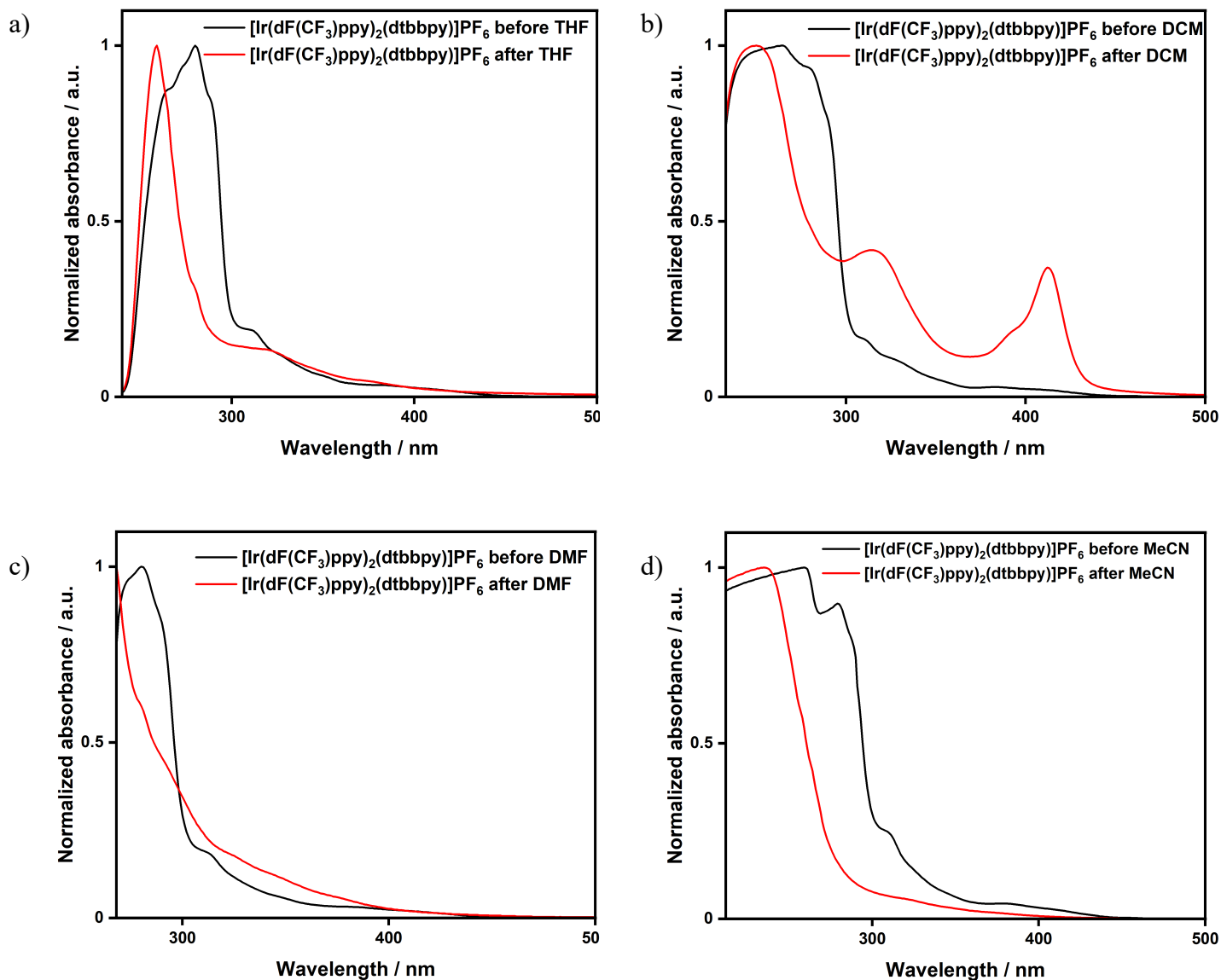Figure **S62**. UV-vis absorption spectra before and after irradiation for the pinacol coupling using **[Ir(dF(CF₃)ppy)₂(dtbbpy)]PF₆** as the PC in a) THF, b) DCM, c) DMF and d) MeCN.
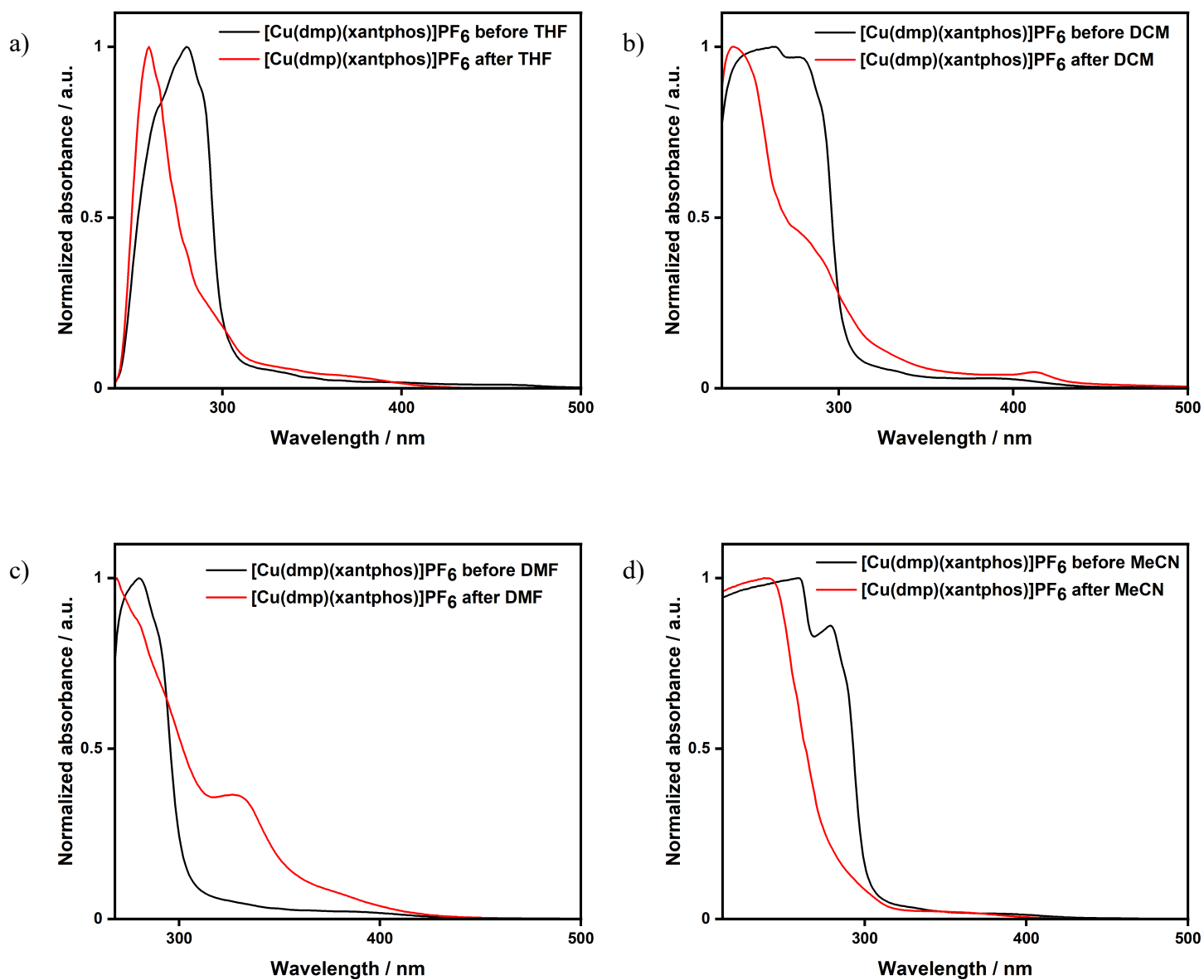
Figure **S63**. UV-vis absorption spectra before and after irradiation for the pinacol coupling using **[Cu(dmp)(xantphos)]PF₆** as the PC in a) THF, b) DCM, c) DMF and d) MeCN.

Figure **S*64***. UV-vis absorption spectra before and after irradiation for the pinacol coupling using **Eosin Y** as the PC in a) THF, b) DCM, c) DMF and d) MeCN.
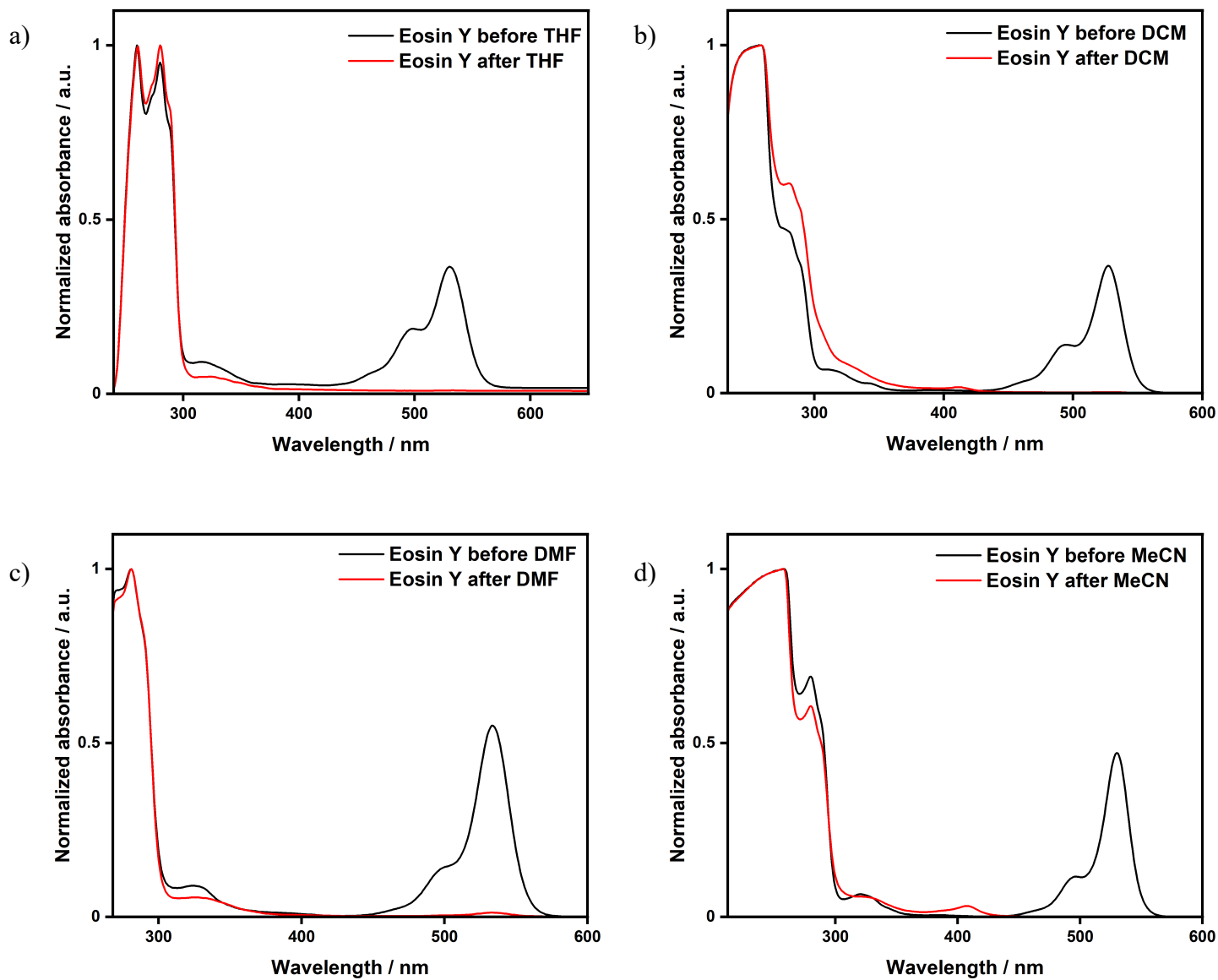
Figure **S65**. UV-vis absorption spectra before and after irradiation for the pinacol coupling using **4CzIPN** as the PC in a) THF, b) DCM, c) DMF and d) MeCN.

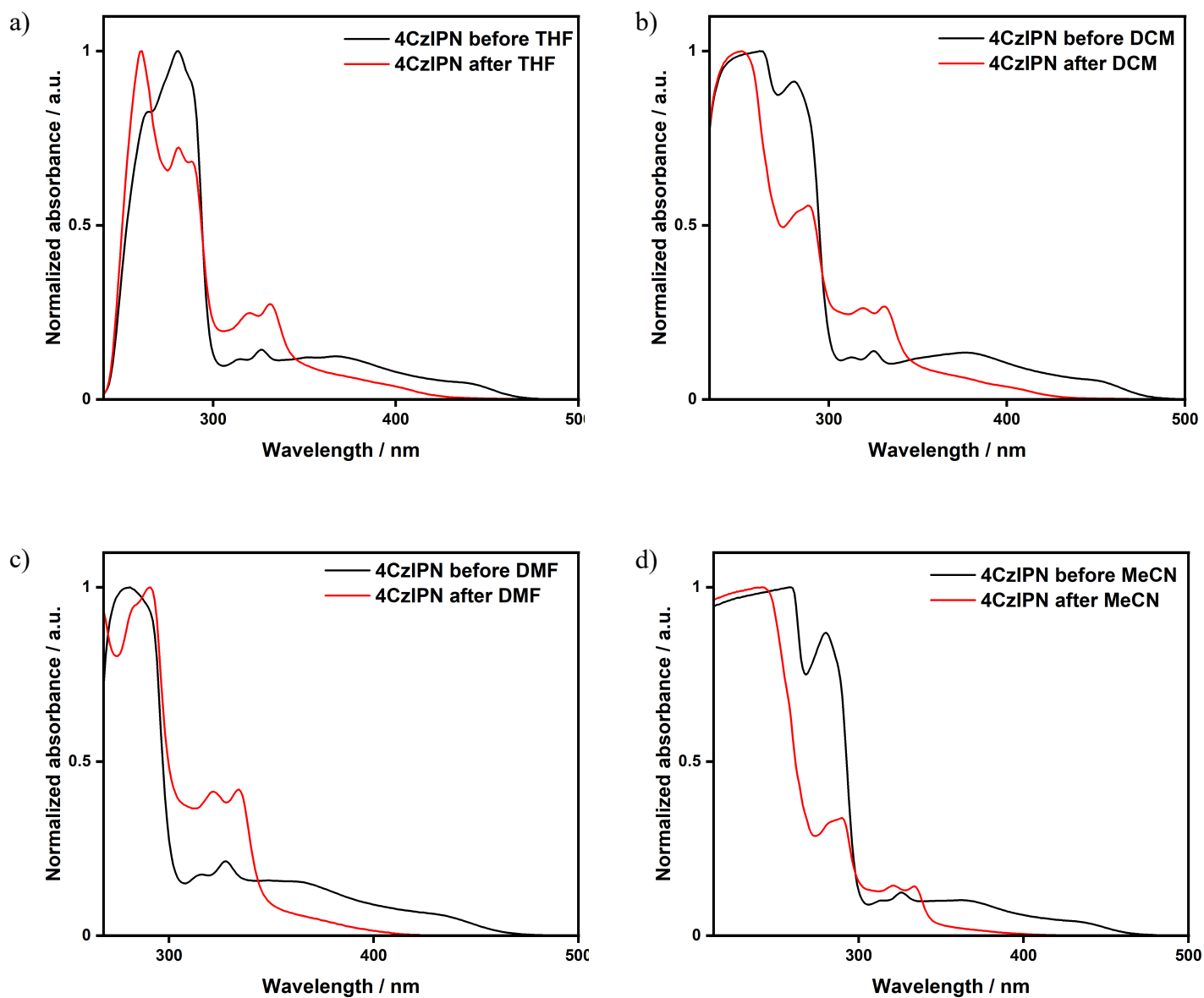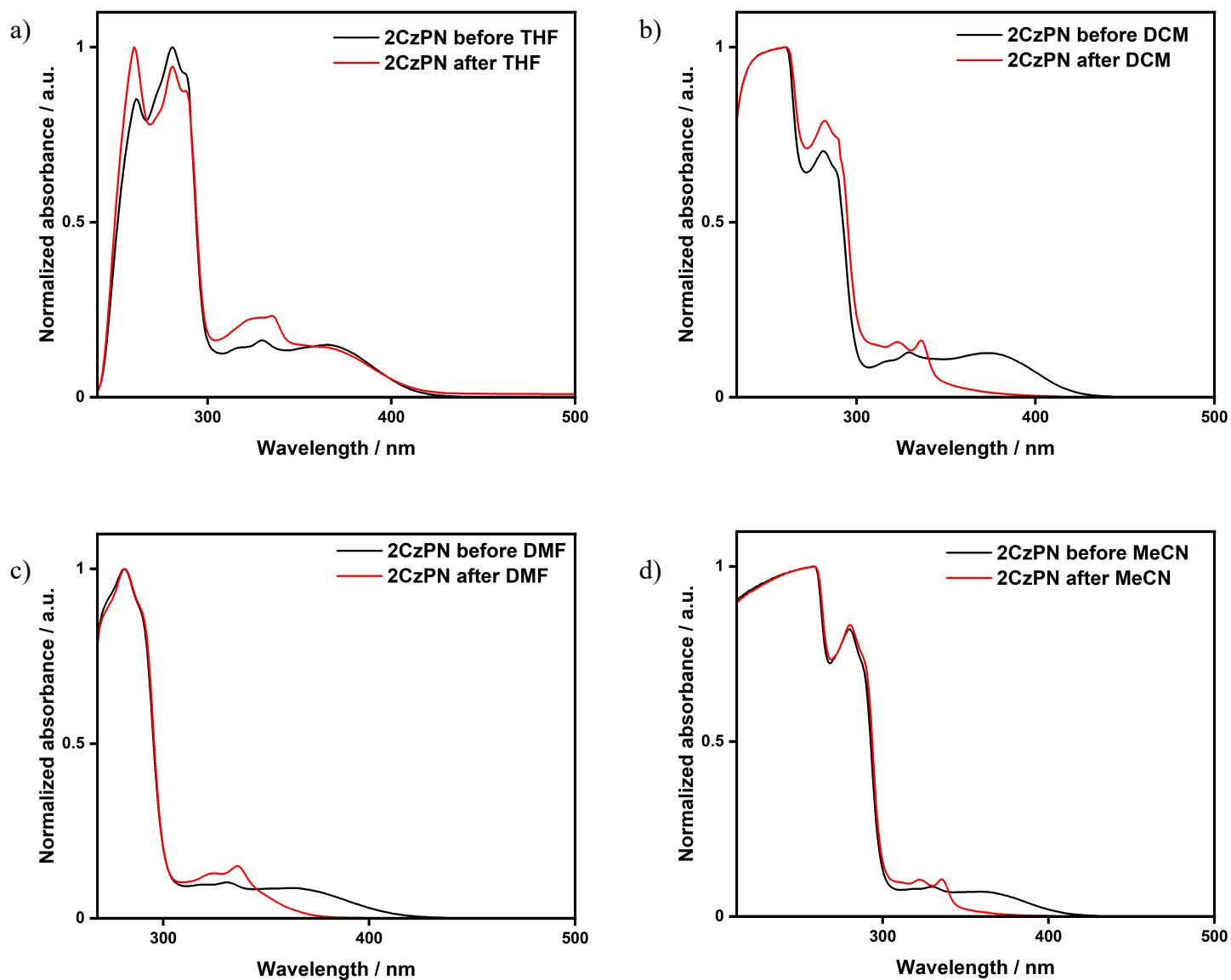Figure **S66**. UV-vis absorption spectra before and after irradiation for the pinacol coupling using **2CzPN** as the PC in a) THF, b) DCM, c) DMF and d) MeCN.

ATRA:
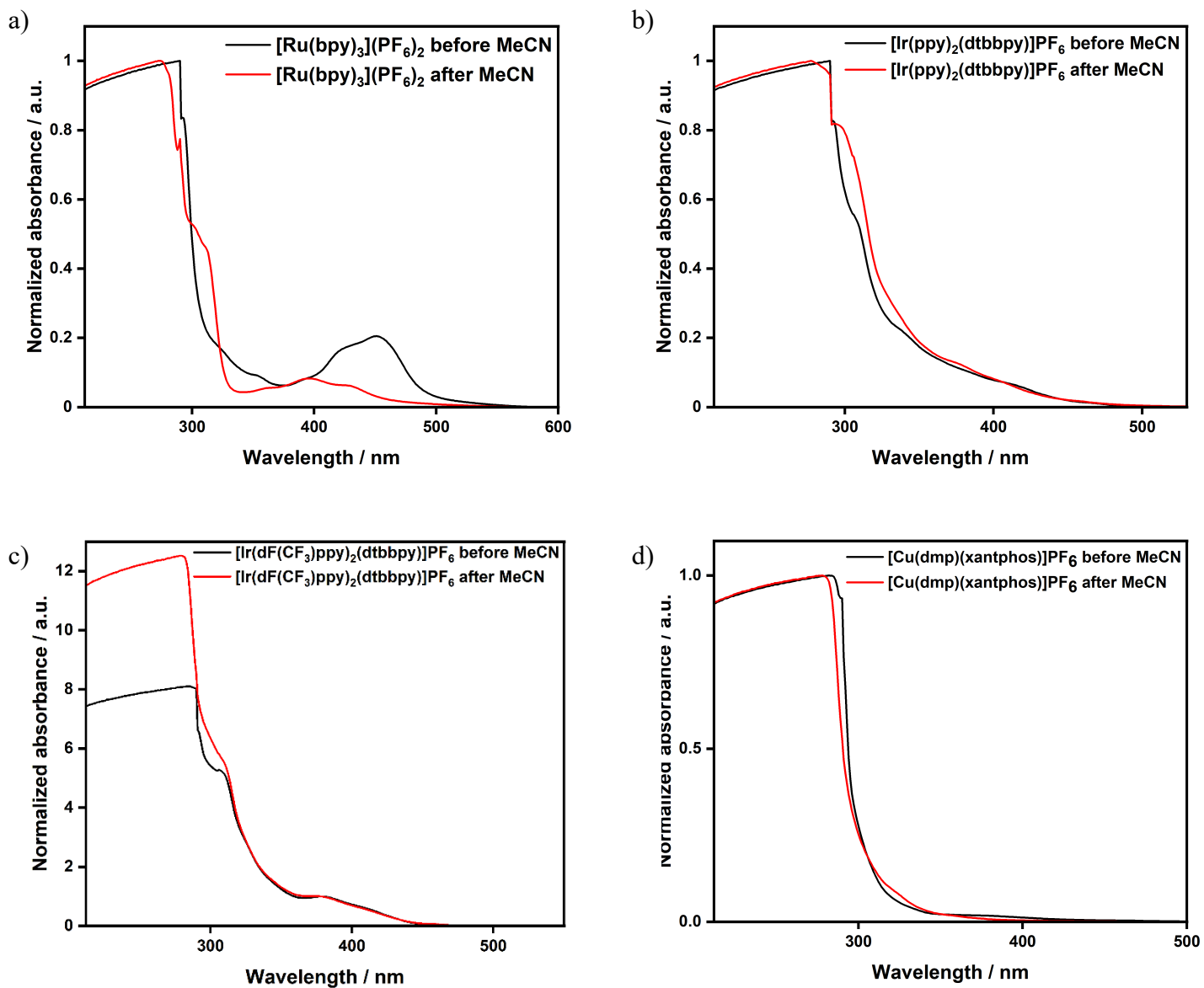
Figure **S67**. UV-vis absorption spectra before and after irradiation for the ATRA reaction using a) **[Ru(bpy)₃](PF₆)₂**, b) **[Ir(ppy)₂(dtbbpy)]PF₆**, c) **[Ir(dF(CF₃)ppy)₂(dtbbpy)]PF₆** and d) **[Cu(dmp)(xantphos)]PF₆** as the PC. Absorbance is normalized with respect to the peak at 378 nm for c).
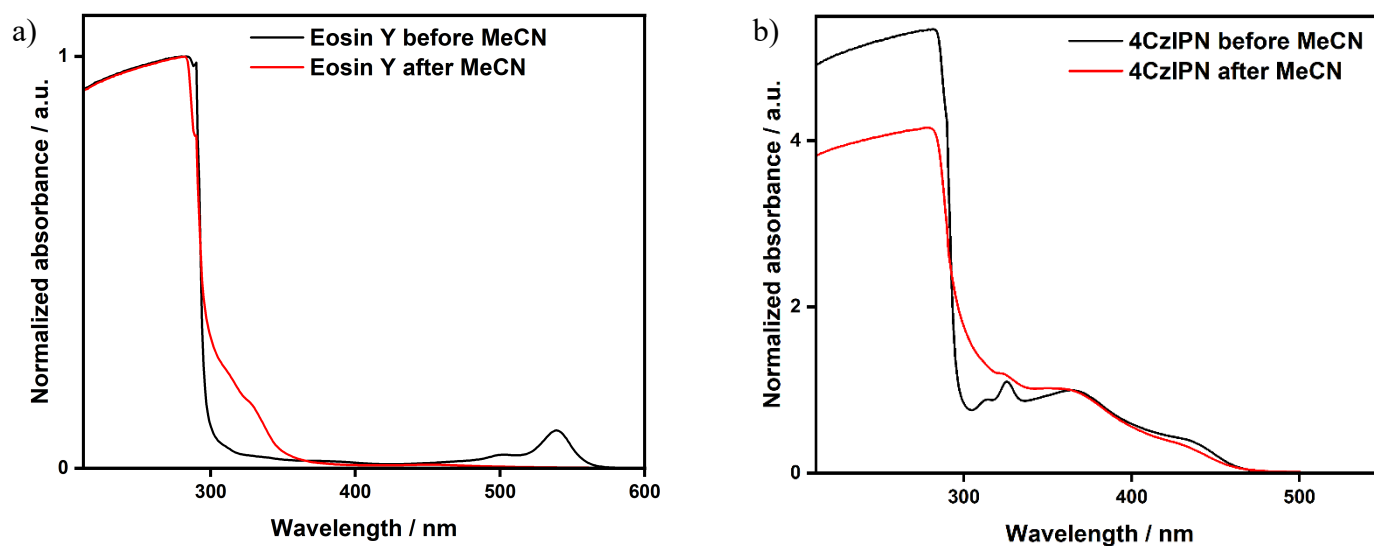
Figure **S68**. V-vis absorption spectra before and after irradiation for the ATRA reaction using a) **Eosin Y** and b) **4CzIPN** as the PC. Absorbance is normalized with respect to the peak at 364 nm for b).

Giese type addition:

Figure **S69**. UV-vis absorption spectra before and after irradiation for the Giese-type addition using a) **[Ru(bpy)₃](PF₆)₂**, b) **[Ir(dF(CF₃)ppy)₂(dtbbpy)]PF₆**, c) **[Cu(dmp)(xantphos)]PF₆** and d) **Eosin Y** as the PC. Absorbance is normalized with respect to the peak at 535 nm for d).
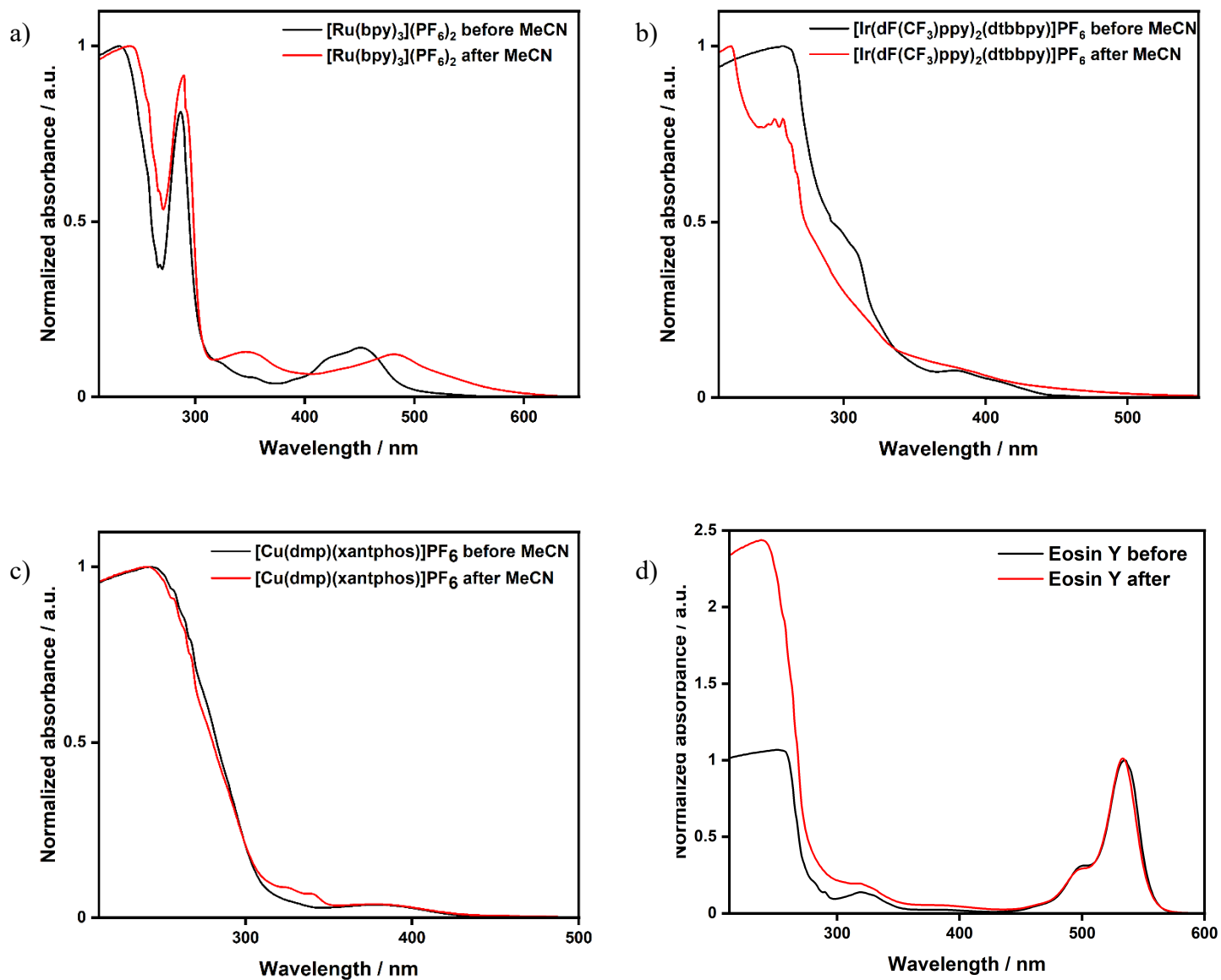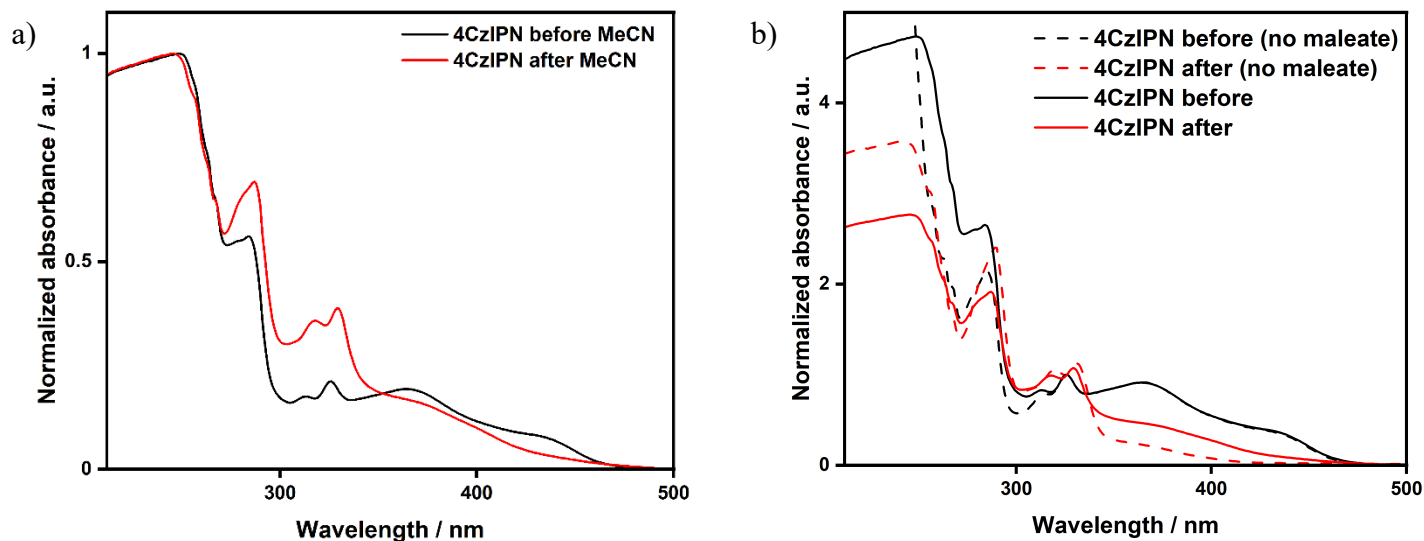
Figure **S70**. a) UV-vis absorption spectra before and after irradiation for the Giese-type addition using **4CzIPN** as the PC and b) the comparison to the UV-vis absorption spectra before and after irradiation for the Giese-type addition using **4CzIPN** as the PC in the absence of the diethyl maleate radical acceptor. In b), the UV-vis absorption spectra are all normalized with respect to the peak at 326 nm.

Figure **S69b** indicates that in the absence of a radical acceptor (diethyl maleate), the UV-vis absorption profile after irradiation using **4CzIPN** as the PC is significantly more blue-shifted. This is in accordance with literature studies that have shown that after decarboxylation, the alkyl radical generated from carboxylic acids (N-Cbz-Pro in this case), photosubstitutes one of the CN groups of **4CzIPN**.[51] In the presence of a radical acceptor (diethyl maleate in this case), less photosubstitution occurs, as reflected in the less blue-shifted UV-vis absorption profile after irradiation, since the alkyl radical can instead be trapped by the radical acceptor.
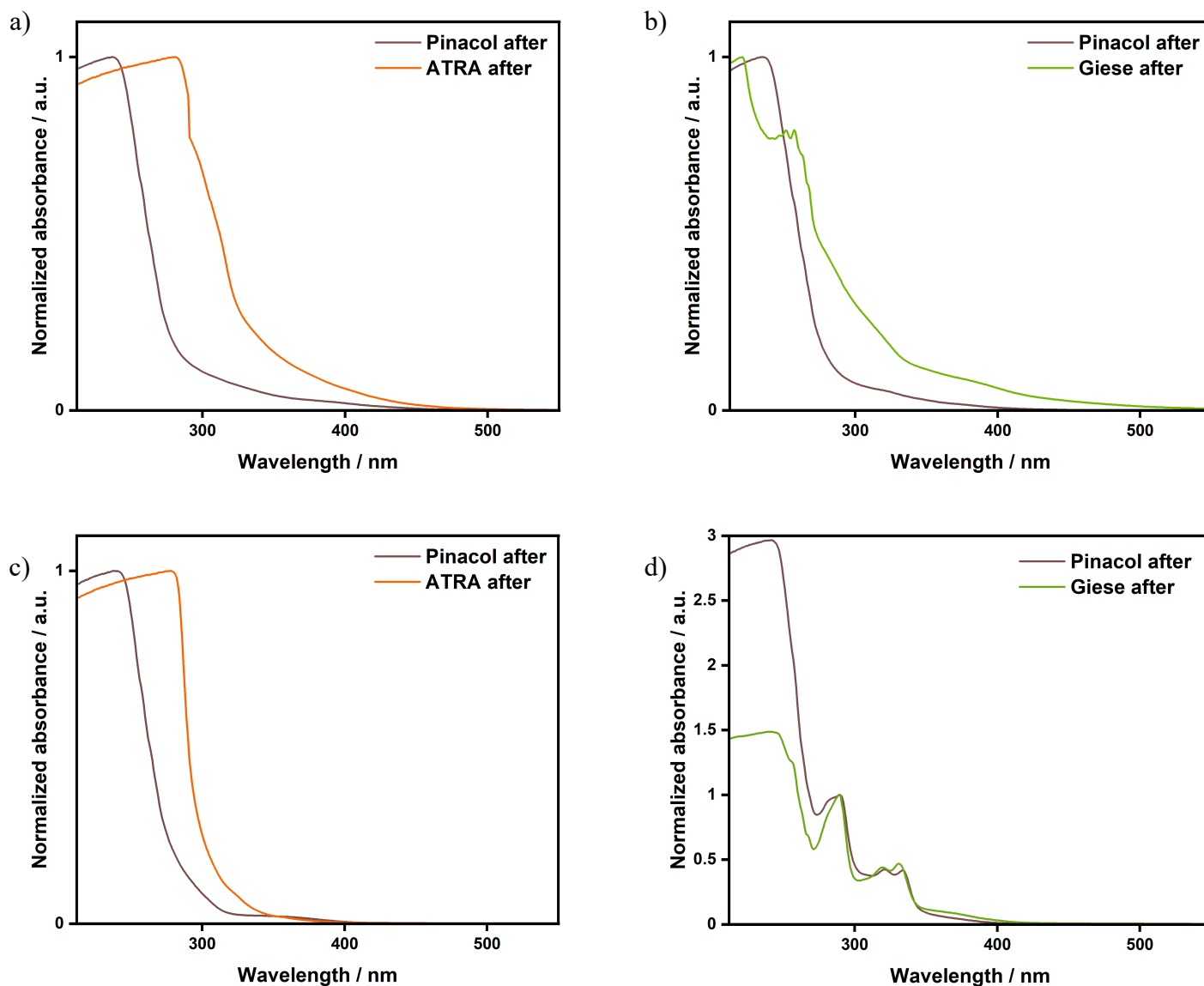
Figure **S71**. UV-vis absorption spectra after irradiation for the a combination of the pinacol coupling, ATRA or Giese-type addition in MeCN using a) **[Ir(ppy)$_2$(dtbbpy)]PF$_6$**, b) **[Ir(dF(CF$_3$)ppy)$_2$(dtbbpy)]PF$_6$**, c) **[Cu(dmp)(xantphos)]PF$_6$** and d) **4CzIPN** as the PC. Absorbance is normalized with respect to the peak at 290 nm for d).

E/Z isomerisation:

Figure **S72**. UV-vis absorption spectra before and after irradiation for the *E/Z* isomerization of stilbene using **[Ru(bpy)₃](PF₆)₂** as the PC in a) DCM, b) DCM (normalized with respect to the peak at 455 nm), c) DMF and d) MeCN. Due to poor solubility in THF, suitable UV-vis absorption spectra could not be obtained.
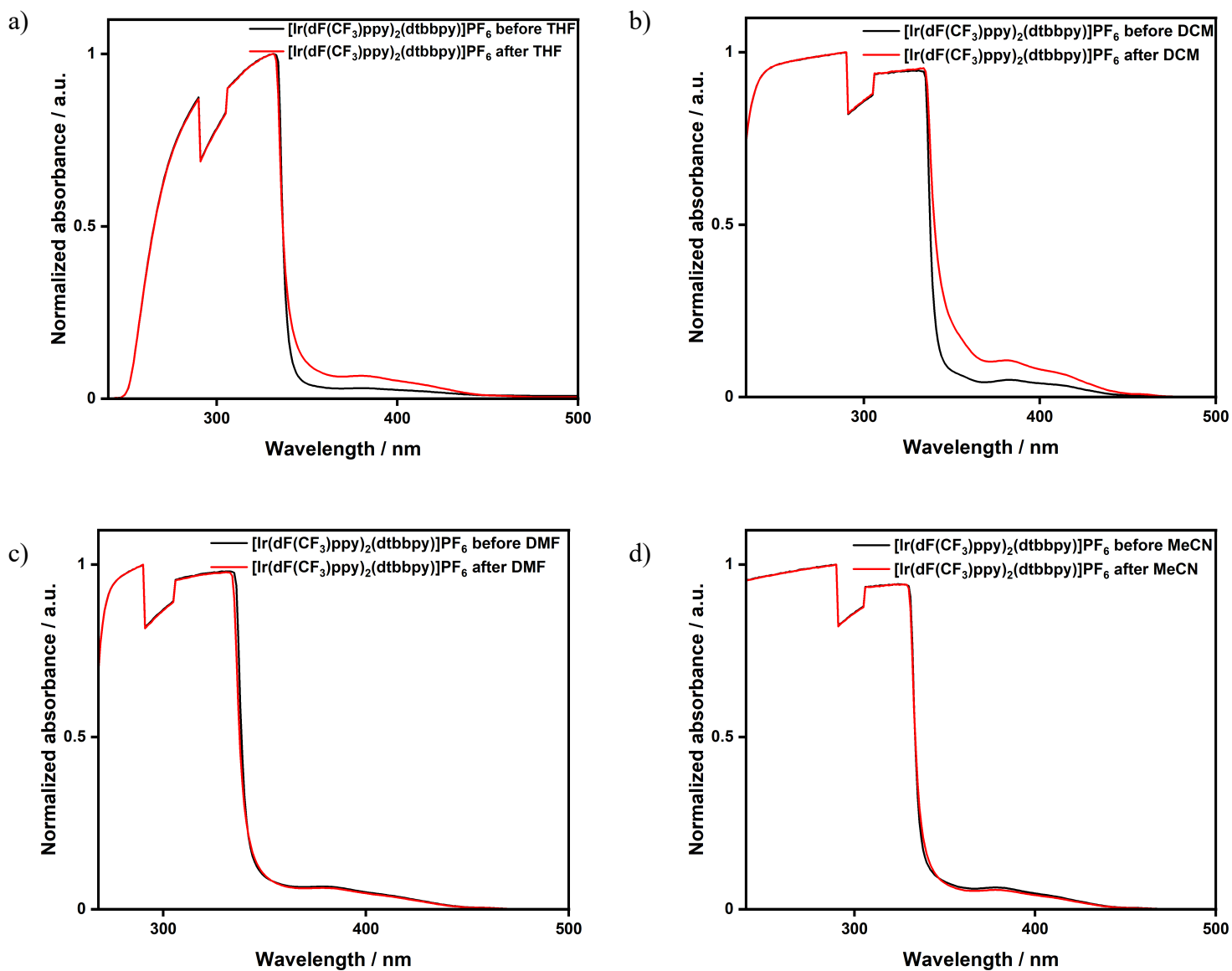
Figure **S73**. UV-vis absorption spectra before and after irradiation for the *E/Z* isomerization of stilbene using **[Ir(dF(CF₃)ppy)₂(dtbbpy)]PF₆** as the PC in a) THF, b) DCM, c) DMF and d) MeCN.
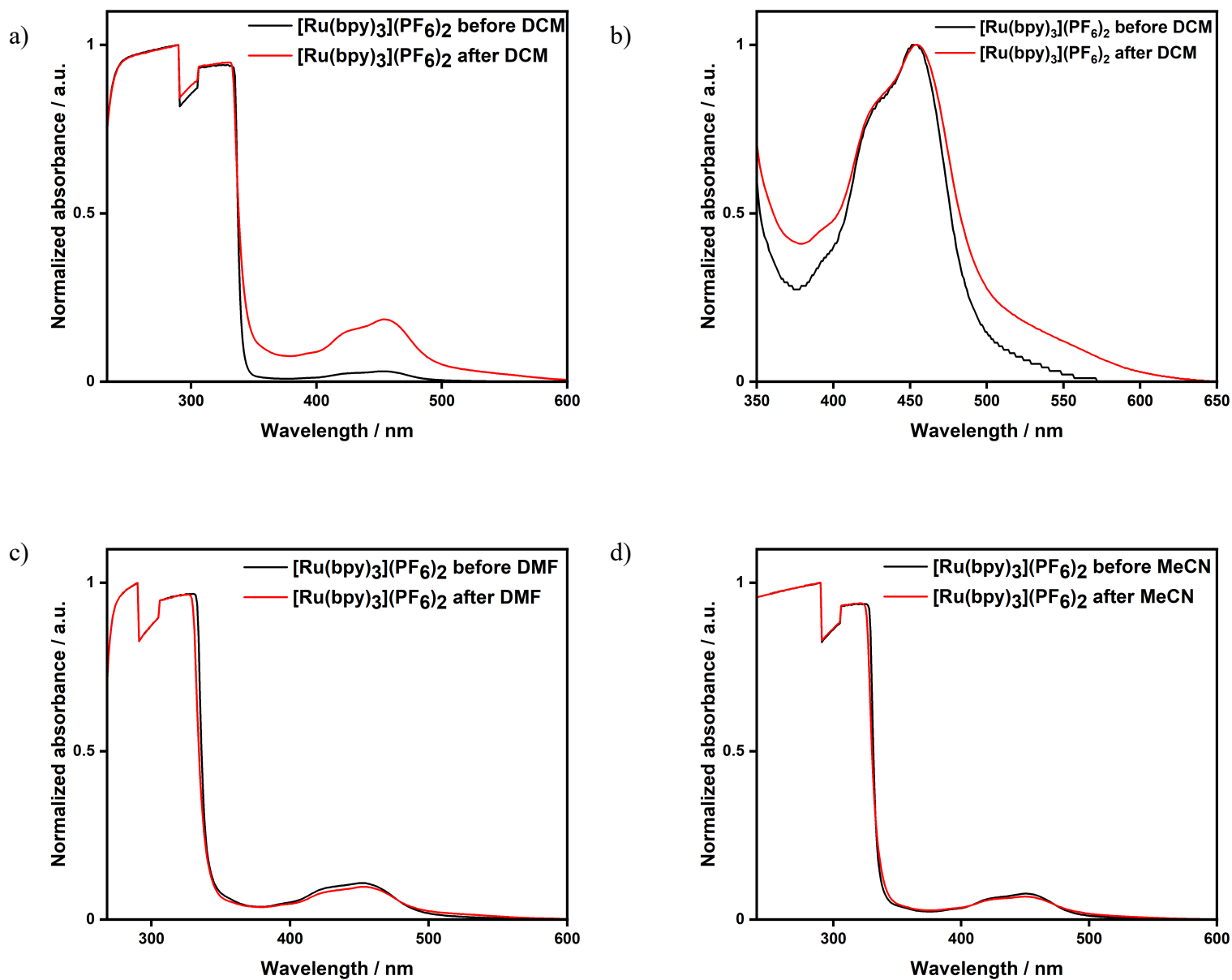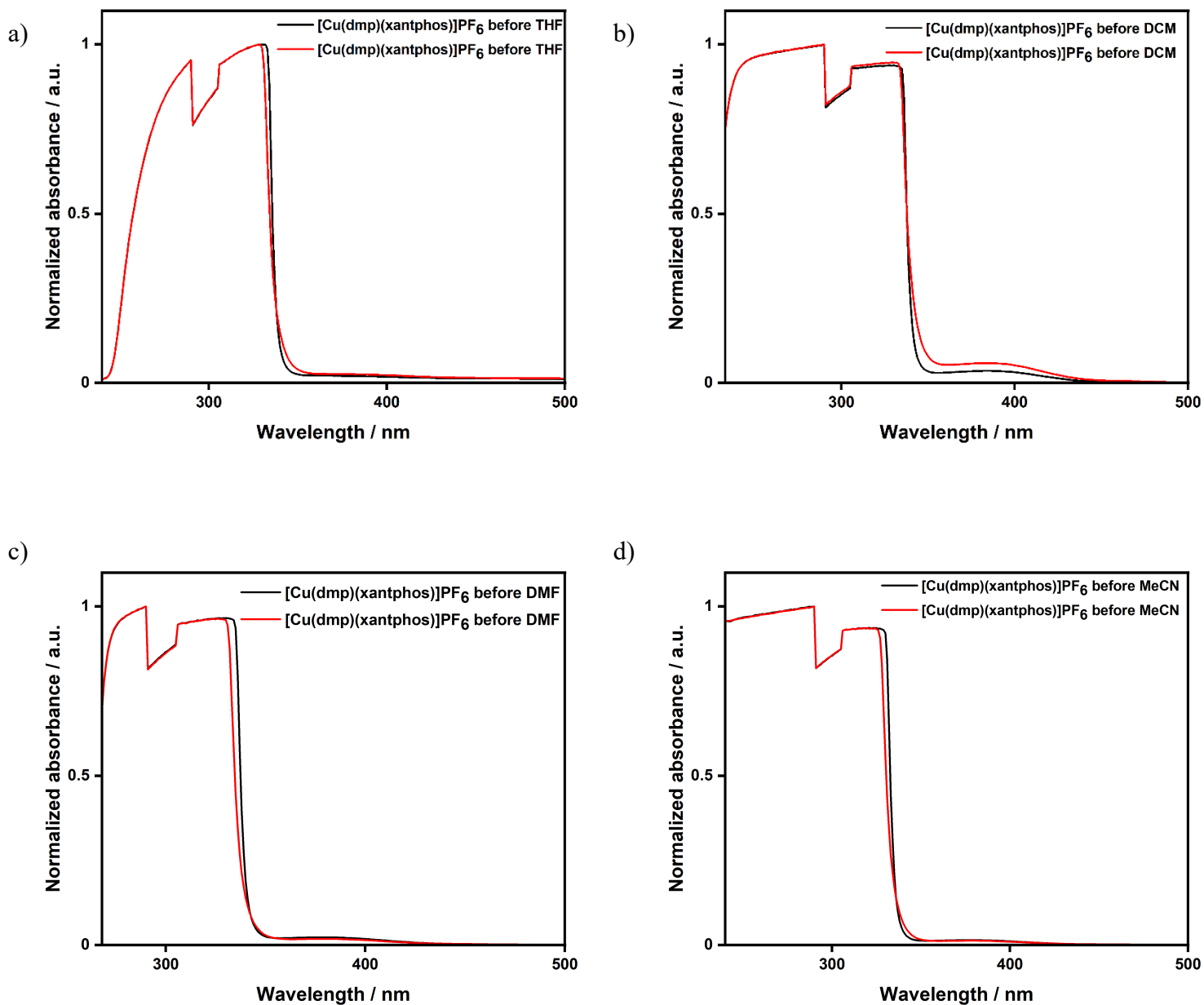
Figure **S74**. UV-vis absorption spectra before and after irradiation for the *E/Z* isomerization of stilbene using **[Cu(dmp)(xantphos)]PF₆** as the PC in a) THF, b) DCM, c) DMF and d) MeCN.
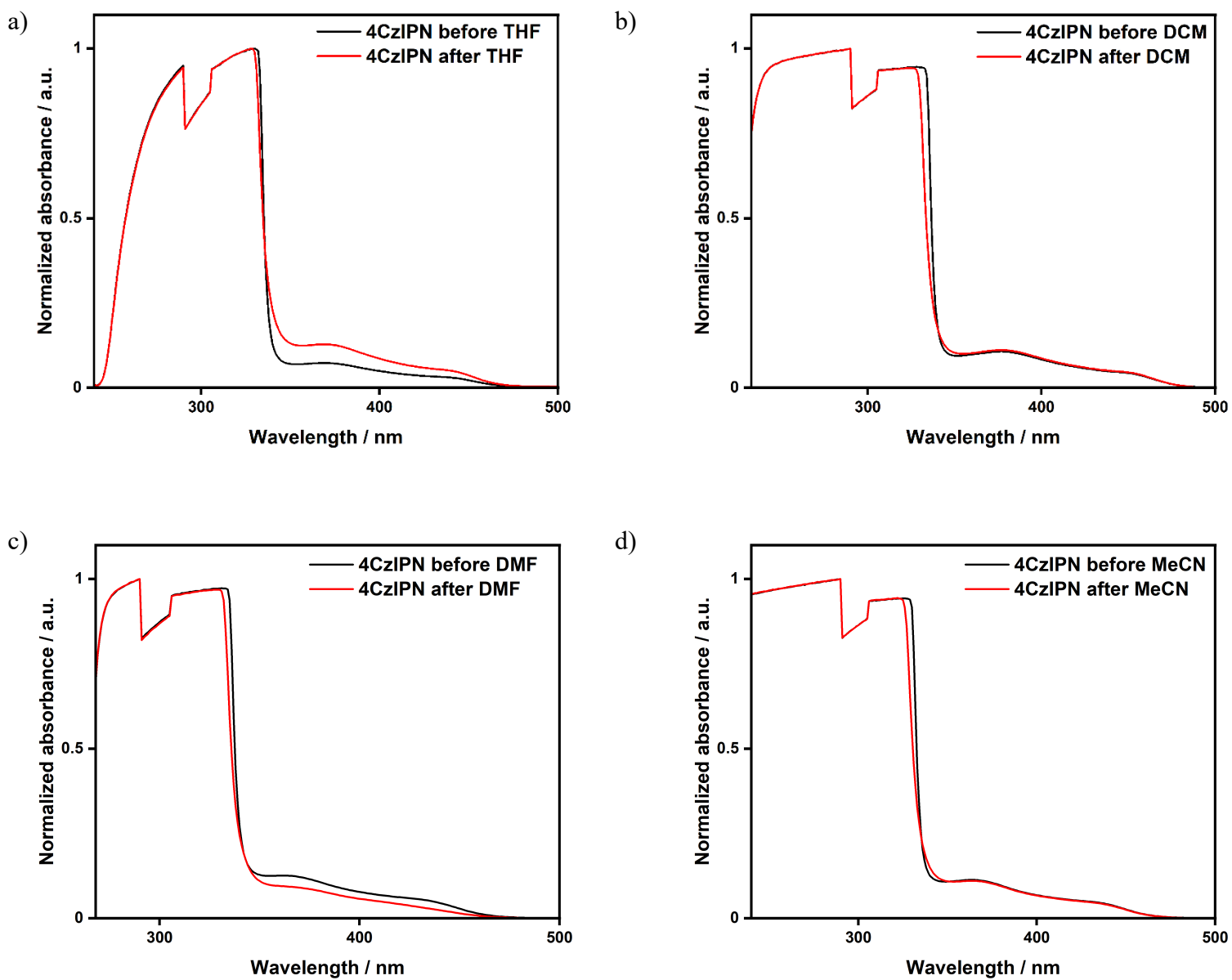
Figure **S75**. UV-vis absorption spectra before and after irradiation for the *E/Z* isomerization of stilbene using **4CzIPN** as the PC in a) THF, b) DCM, c) DMF and d) MeCN.
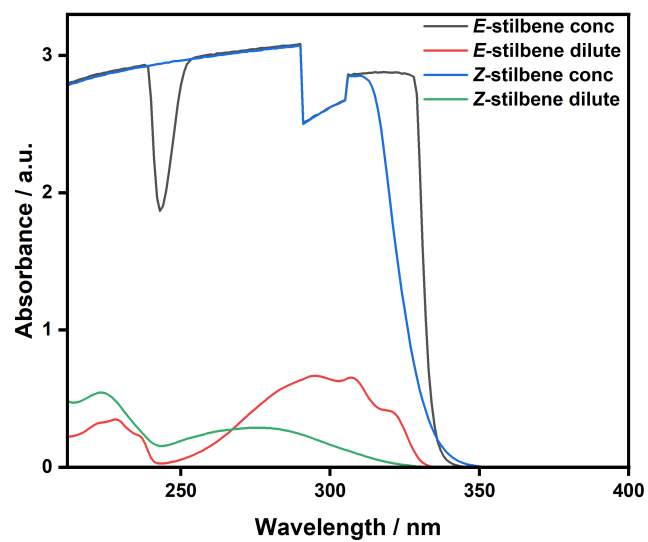
Figure **S76**. UV-vis absorption spectra of *E* and *Z* stilbene using a concentrated solution $(1 \times 10^{-3}$ M$)$ and dilute solution $(2 \times 10^{-5}$ M$)$ in MeCN.

[2+2] cycloaddition:
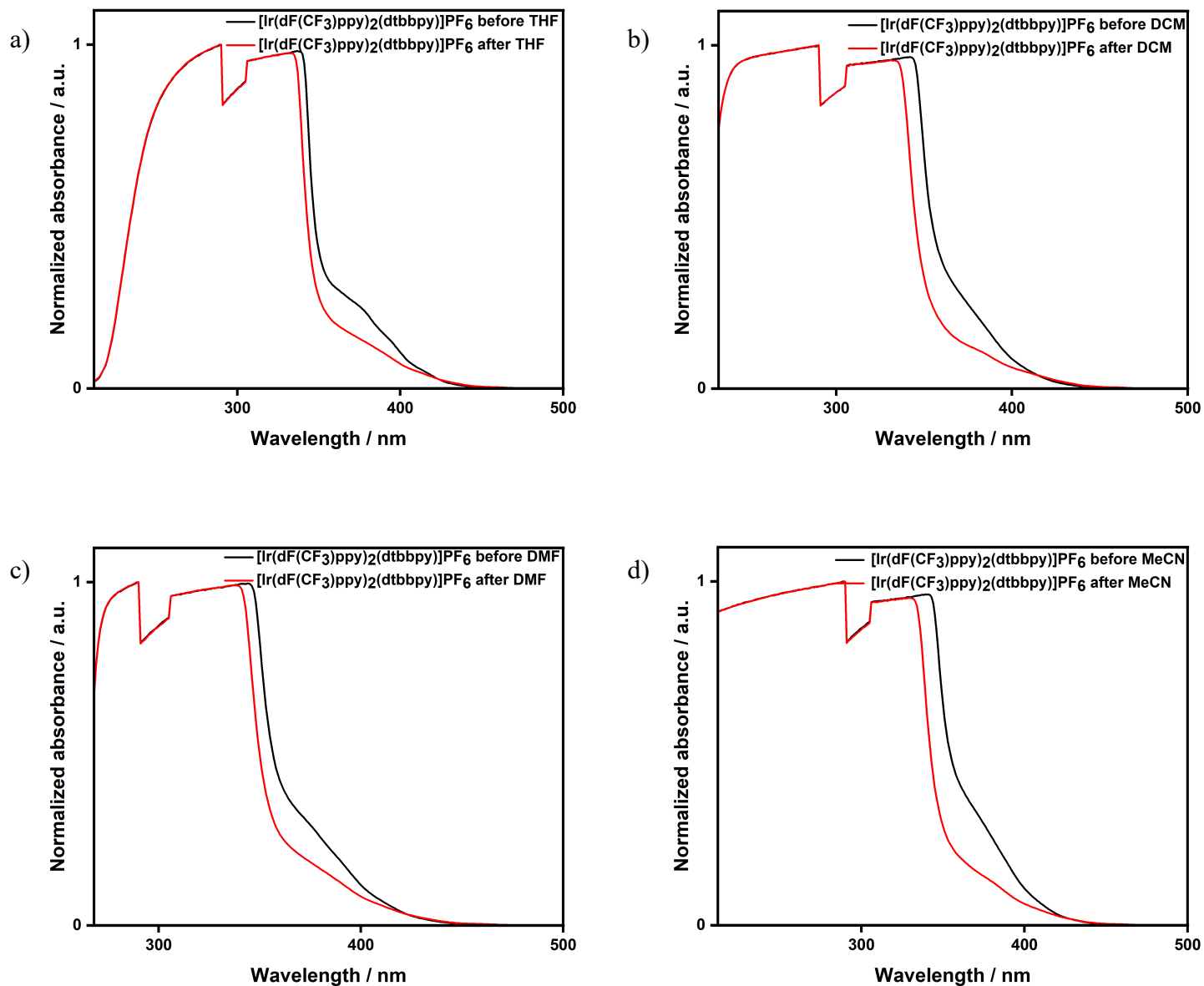
Figure **S77**. UV-vis absorption spectra before and after irradiation for the [2+2] cycloaddition of chalcone using **[Ir(dF(CF₃)ppy)₂(dtbbpy)]PF₆** as the PC in a) THF, b) DCM, c) DMF and d) MeCN.
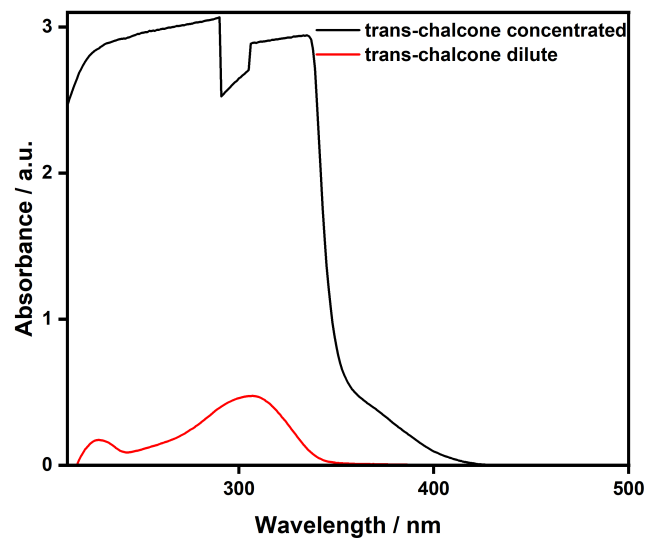
Figure **S78**. UV-vis absorption spectra of trans-chalcone using a concentrated solution (1 $\times$ 10^{-3} M) and dilute solution (2 $\times$ 10^{-5} M) in MeCN.

a) 2305121239-3-29-mab30.10.fid
MAB-IV17-40523 IrdF bpy instead of dtbbpy in CDCl3 || 19F Observe with 1H decoupling – Full Range SW 2

b) 2305121239-3-28-mab30.10.fid
MAB-IV17-40523 IrdF in CDCl3 || 19F Observe with 1H decoupling – Full Range SW 1
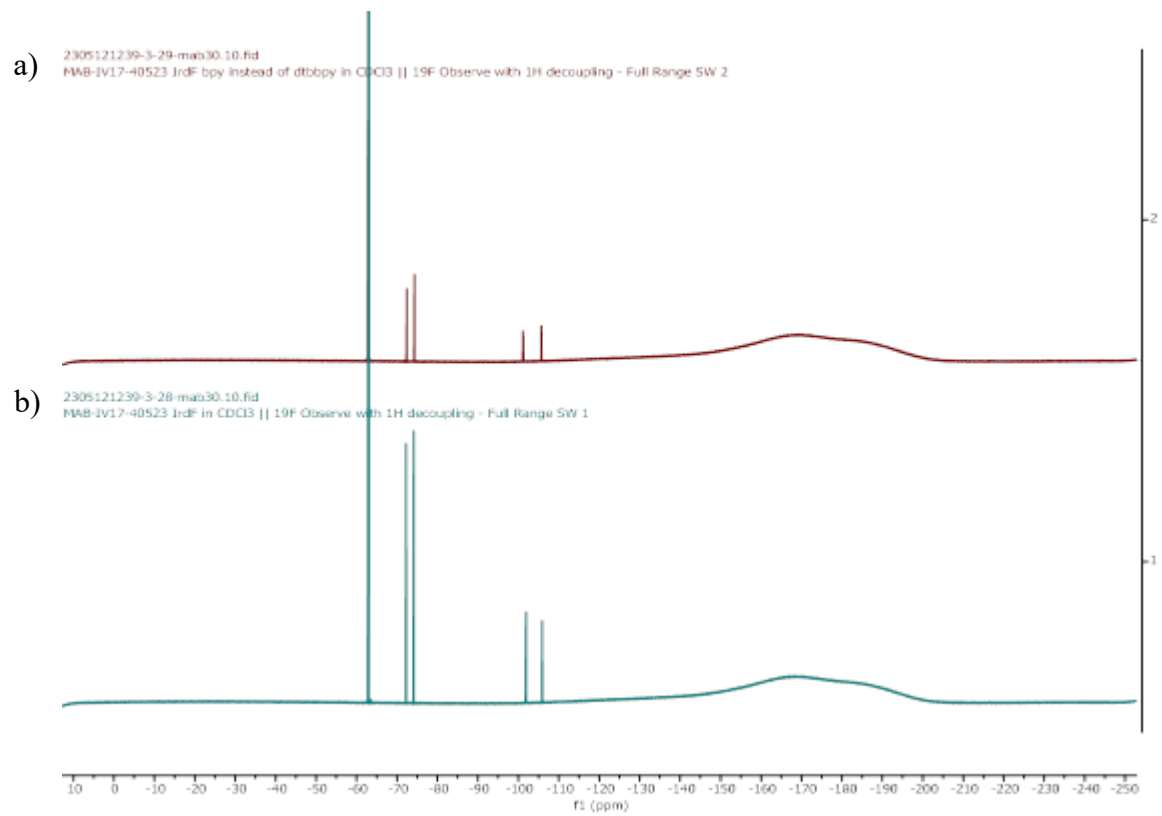
Figure **S79**. ^{19}F NMR of a) **[Ir(dF(CF$_3$)ppy)$_2$(bpy)]PF$_6$** and b) **[Ir(dF(CF$_3$)ppy)$_2$(dtbbpy)]PF$_6$** in CDCl$_3$.
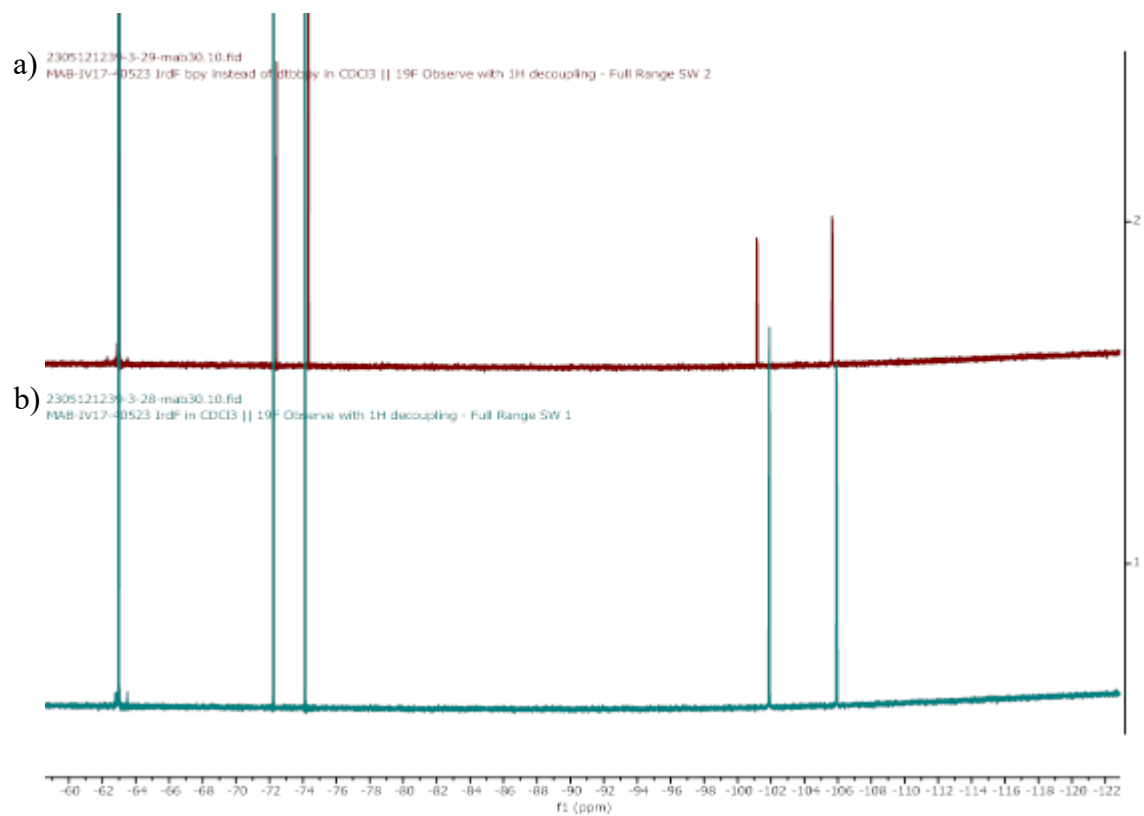
Figure **S80**. ^{19}F NMR of a) **[Ir(dF(CF$_3$)ppy)$_2$(bpy)]PF$_6$** and b) **[Ir(dF(CF$_3$)ppy)$_2$(dtbbpy)]PF$_6$** in CDCl$_3$ zoomed in.

Figure **S81**. ^{19}F NMR of the [2+2] cycloaddition of chalcone reaction mixtures after irradiation in a) THF, b) DCM, c) DMF and d) MeCN and e) the PC **[Ir(dF(CF₃)ppy)₂(dtbbpy)]PF₆** all in CDCl₃.
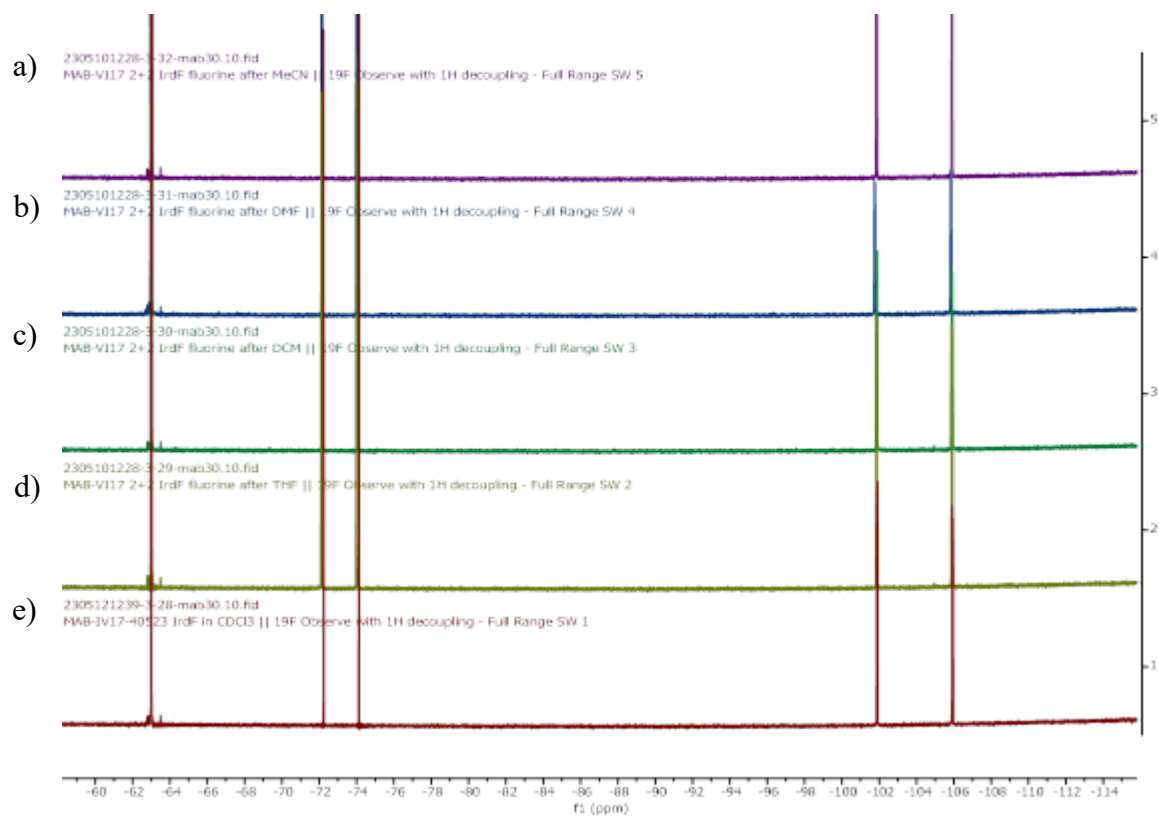
Figure **S82**. ^{19}F NMR of the [2+2] cycloaddition of chalcone reaction mixtures after irradiation in a) THF, b) DCM, c) DMF and d) MeCN and e) the PC **[Ir(dF(CF₃)ppy)₂(dtbbpy)]PF₆** all in CDCl₃ zoomed in.

Photocatalysis

Photocatalysis experiments were conducted using a custom-built photoreactor, as shown in Figure **S82**, allowing for up to 8 parallel photochemical reactions (7 mL) at a time. The photochemistry reaction chamber is filled with mirrors to evenly distribute light. The reactor is placed upon a magnetic stirrer plate allowing for reactions to be completed with stirring. Reactions are irradiated using Kessil PR160 and PR160L LED sources. For Kessil PR160-390 nm and PR160L-456 nm, the power consumption maximum is 52 W and 50 W, respectively, with the average intensity measured from 1 cm distance being 399 mW cm^{-2}. The intensity on each lamp is tuneable, with the maximum intensity selected for all photocatalytic reactions. A cooling fan is directed at the photoreactor to ensure the reaction mixture maintains at room temperature, which is further guaranteed by the presence of two fans on the photoreactor itself.

After the photoreactions were completed, the products were analysed by ^{1}H NMR spectroscopy using 1,3,5-trimethoxybenzene as an internal standard. All yields shown represent the mean yield from at least two reactions with the associated standard deviation.
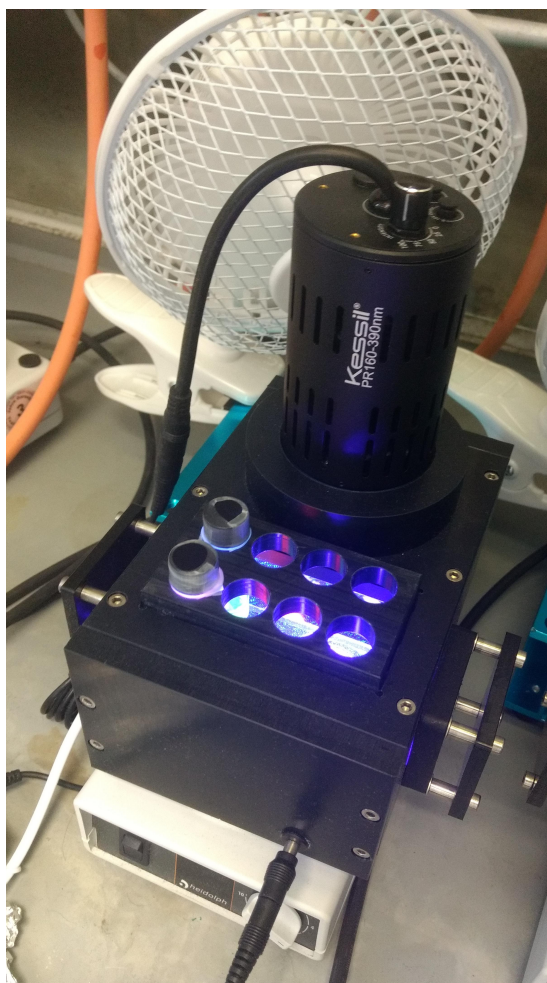
Figure **S83**. Experimental set-up for photocatalysis reactions.

Procedure for the pinacol coupling:
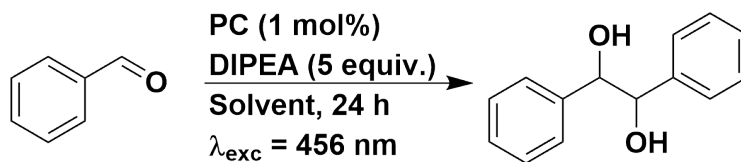
Figure **S84**. Reaction scheme for the pinacol coupling reaction.

To an oven-dried vial was added benzaldehyde (0.020 mL, 0.2 mmol, 1 equiv.), DIPEA (0.174 mL, 1 mmol, 5 equiv.) and photocatalyst (1 mol%, 0.002 mmol). The vial was purged with N_2 for 5 min and solvent (2.0 mL) was added before N_2 bubbling for 10 min. The solution was stirred at room temperature while being irradiated by Kessil lamp (λ_{exc} = 456 nm) for 2 or 24 hours. The solvent was removed under reduced pressure and the crude

reaction mixture was analysed by ^{1}H NMR spectroscopy using 1,3,5-trimethoxybenzene as an internal standard.

Table **S21**. ^{1}H NMR yields obtained for control reactions for the pinacol coupling.[a]

	^{1}H NMR yield / %			
	THF	DCM	DMF	MeCN
None	0	0	0	0
[Ir(ppy)₂(dtbbpy)]PF₆ [b]	2	0	0	0

[a] Yields determined by ^{1}H-NMR analysis of the crude reaction mixture using 1,3,5-trimethoxybenzene as the internal standard. Yields provided are the sum of the meso:dl isomers. The reaction was conducted for 24 h. [b] Reaction conducted in the absence of amine.

Procedure for the ATRA:
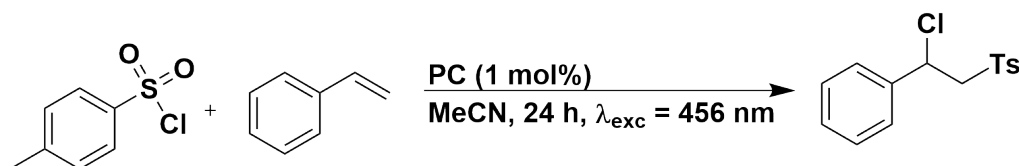
Figure **S85**. Reaction scheme for the ATRA reaction.

To an oven-dried vial was added *p*-toluenesulfonyl chloride (48 mg, 0.25 mmol, 1 equiv.) styrene (0.034 mL, 0.5 mmol, 1.2 equiv.) and photocatalyst (1 mol%, 0.0025 mmol). The vial was purged with N₂ for 5 min and dry MeCN (1.0 mL) was added before further N₂ purging for 10 min. The solution was stirred at room temperature while being irradiated by Kessil lamp (λ_{exc} = 456 nm) for 24 hours. The solvent was removed under reduced pressure and the crude reaction mixture was analysed by ^{1}H NMR spectroscopy using 1,3,5-trimethoxybenzene as an internal standard.

Table **S22**. ^{1}H NMR yields obtained the ATRA reaction.[a]

PC	^{1}H NMR yield / %
None	0
[Ru(bpy)₃](PF₆)₂	75 ± 5 (80)[b]
[Ir(ppy)₂(dtbbpy)]PF₆	74 ± 3
[Ir(dF(CF₃)ppy)₂(dtbbpy)]PF₆	3 ± 1 (7)[b]

[Cu(dmp)(xantphos)]PF$_6$	86 $\pm$ 4
Eosin Y	3 $\pm$ 2
4CzIPN	3 $\pm$ 0

[a] Yields determined by ^{1}H NMR analysis of the crude reaction mixture using 1,3,5-trimethoxybenzene as the internal standard. Yields in parentheses correspond to literature yields and are reference accordingly. Yield taken from Ref [52] obtained using 1 equiv. of styrene and 455 nm LEDs in MeCN.

Procedure for the Giese type addition:
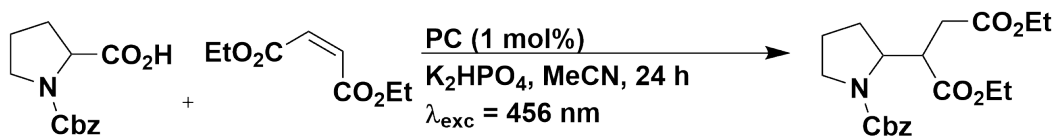
Figure **S86**. Reaction scheme for the Giese type addition reaction.

To an oven-dried vial was added N-Cbz-Pro (50 mg, 0.2 mmol, 1 equiv.), K$_2$HPO$_4$ (38 mg. 0.22 mmol, 1.1 equiv.), diethyl maleate (0.036 mL, 0.22 mmol, 1.1 equiv.) and photocatalyst (1 mol%, 0.002 mmol). The vial was purged with N$_2$ for 5 min and dry MeCN (4.0 mL) was added before further N$_2$ purging for 10 min. The solution was stirred at room temperature while being irradiated by Kessil lamp (λ_{exc} = 456 nm) for 24 hours. The solvent was removed under reduced pressure and the crude reaction mixture was analysed by ^{1}H NMR spectroscopy using 1,3,5-trimethoxybenzene as an internal standard.

Table **S23**. ^{1}H NMR yields obtained for the Giese type addition reaction.[a]

PC	^{1}H NMR yield / %
None	0
[Ru(bpy)$_3$](PF$_6$)$_2$	0 $\pm$ 0
[Ir(dF(CF$_3$)ppy)$_2$(dtbbpy)]PF$_6$	73 $\pm$ 5
[Cu(dmp)(xantphos)]PF$_6$	0 $\pm$ 0
Eosin Y	Trace
4CzIPN	77 $\pm$ 2 (80)[b]

[a] Yields determined by ^{1}H NMR analysis of the crude reaction mixture using 1,3,5-trimethoxybenzene as the internal standard. Yields in parentheses correspond to literature yields

and are reference accordingly. [b] Yield taken from Ref [42] obtained using 455 nm LEDs and is an isolated yield.

Procedure for the *E/Z* or *Z/E* isomerization of stilbene:

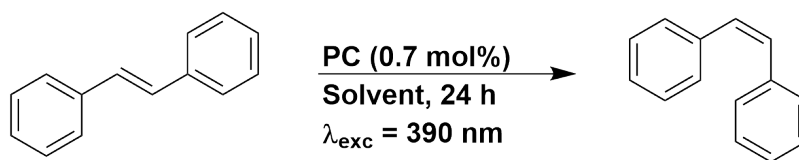Figure **S87**. Reaction scheme for the *E/Z* isomerisation of *E*-stilbene.
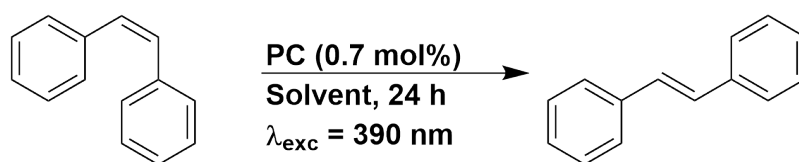
Figure **S88**. Reaction scheme for the *Z/E* isomerisation of *Z*-stilbene.

To an oven-dried vial was added *E*-stilbene (36 mg, 0.2 mmol, 1 equiv.) or *Z*-stilbene (36 μL, 0.2 mmol, 1 equiv.) and photocatalyst (0.7 mol%, 0.0014 mmol). The vial was purged with N_2 for 5 min and solvent (1.0 mL) was added before further N_2 purging for 10 min. The solution was stirred at room temperature while being irradiated by Kessil lamp (λ_{exc} = 390 nm) for 24 hours. The solvent was removed under reduced pressure and the crude reaction mixture was analysed by ^{1}H NMR spectroscopy using 1,3,5-trimethoxybenzene as an internal standard.

Table **S24**. ^{1}H NMR yields obtained for control reactions for the *E/Z* isomerisation of *E*-stilbene.[a]

	^{1}H NMR yield / %			
	THF	DCM	DMF	MeCN
No PC	3 ± 2	19 ± 4	8 ± 1	6 ± 1

[a] Yields determined by ^{1}H NMR analysis of the crude reaction mixture using 1,3,5-trimethoxybenzene as the internal standard.

Table **S25**. ^{1}H NMR yields obtained for the *Z/E* isomerisation of *Z*-stilbene.[a]

PC	^{1}H NMR yield / %
[Ru(bpy)₃](PF₆)₂	7 ± 1

S110

trimethoxybenzene as the internal standard.

Z-stilbene was formed by scaling up the aforementioned procedure. E-stilbene (504 mg, 2.8 mmol, 1 equiv.) and **[Ru(bpy)₃](PF₆)₂** (16.8 mg, 0.7 mol%, 0.02 mmol) were irradiated by Kessil lamp (λ_{exc} = 390 nm) in THF (14 mL) for 24 h. Upon completion, the solvent was removed under reduced pressure and purified by flash column chromatography on silica gel (100% hexane) to afford the product as a colourless oil (351 mg, 70%). **R$_f$**: 0.35 (hexane). **^{1}H NMR (400 MHz, CDCl₃)**, δ (ppm): 7.29-7.16 (m, 10H), 6.64 (s, 2H). The ^{1}H NMR spectrum is consistent with that in the literature.[53]

a)
2305151027-2-15-mab30.10.fid
MAB-VJ9 E stilbene || 1H Observe 2

b)
270741-2-22-mab30.10.fid
VJ9-250423 F1-9 || 1H Observe 1

Figure **S89**. ^{1}H NMR spectra of a) E-stilbene and b) Z-stilbene, both in CDCl₃.

S111

Procedure for [2+2] cycloaddition:

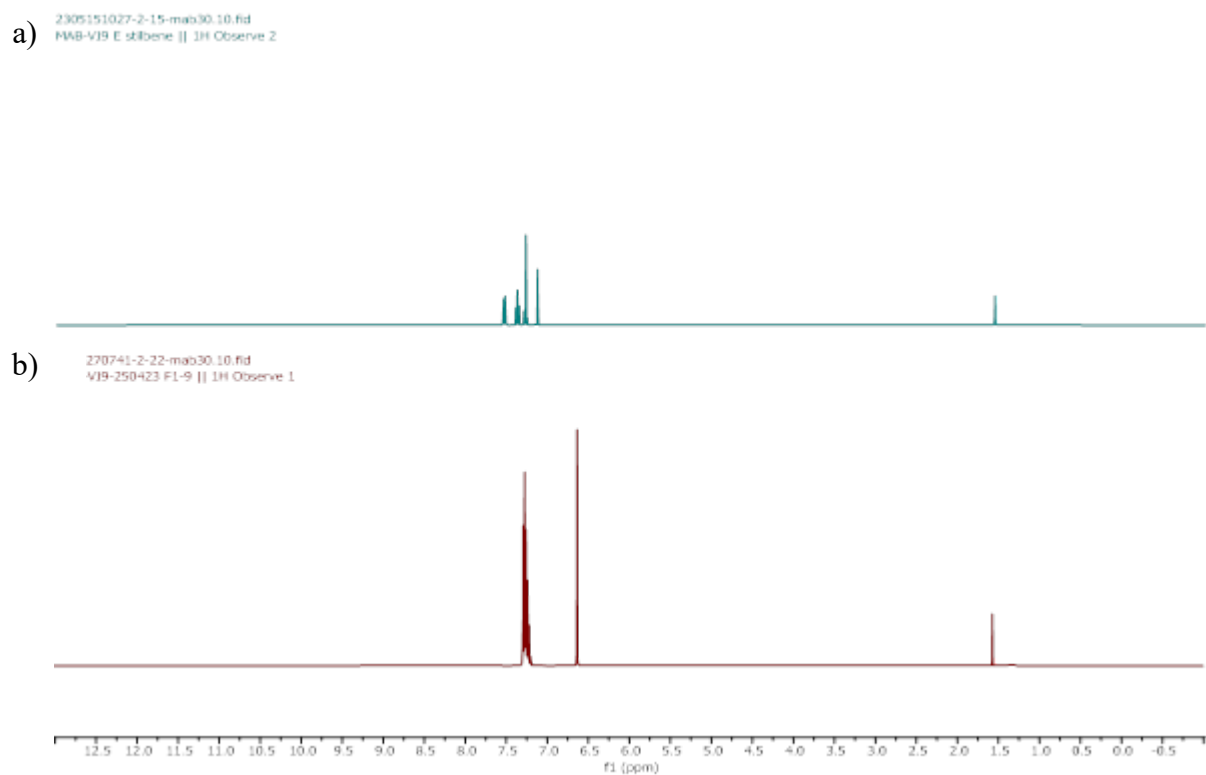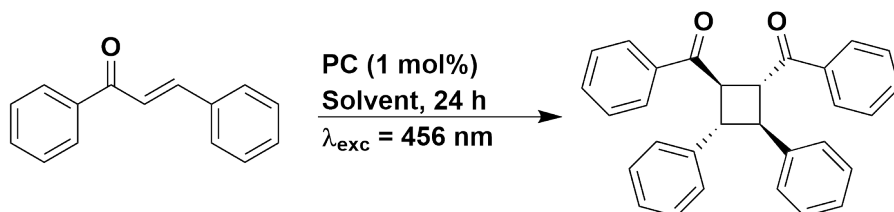
Figure **S90**. Reaction scheme for the [2+2] cycloaddition reaction.

To an oven-dried vial was added *trans*-chalcone (42 mg, 0.2 mmol, 1 equiv.) and photocatalyst (1 mol%, 0.002 mmol). The vial was purged with N_2 for 5 min and solvent (2.0 mL) was added before further N_2 purging for 10 min. The solution was stirred at room temperature while being irradiated by Kessil lamp ($\lambda_{exc} = 456$ nm) for 24 hours. The solvent was removed under reduced pressure and the crude reaction mixture was analysed by ^{1}H NMR spectroscopy using 1,3,5-trimethoxybenzene as an internal standard.

Table **S26**. ^{1}H NMR yields obtained for [2+2] cycloaddition reaction.[a]

	^{1}H NMR yield / %			
	THF	DCM	DMF	MeCN
No PC	2	1	1	1
[Ir(dF(CF₃)ppy)₂(dtbbpy)]PF₆	40 ± 4	37 ± 2	22 ± 2	31 ± 3

[a] Yields determined by ^{1}H NMR analysis of the crude reaction mixture using 1,3,5-trimethoxybenzene as the internal standard.

NMR spectra

Figure **S91**. [^1]H NMR spectra of *Z*-stilbene in CDCl$_3$.

References

1   C. Hu and Y. Chen, *Org. Chem. Front.*, 2015, **2**, 1352–1355.
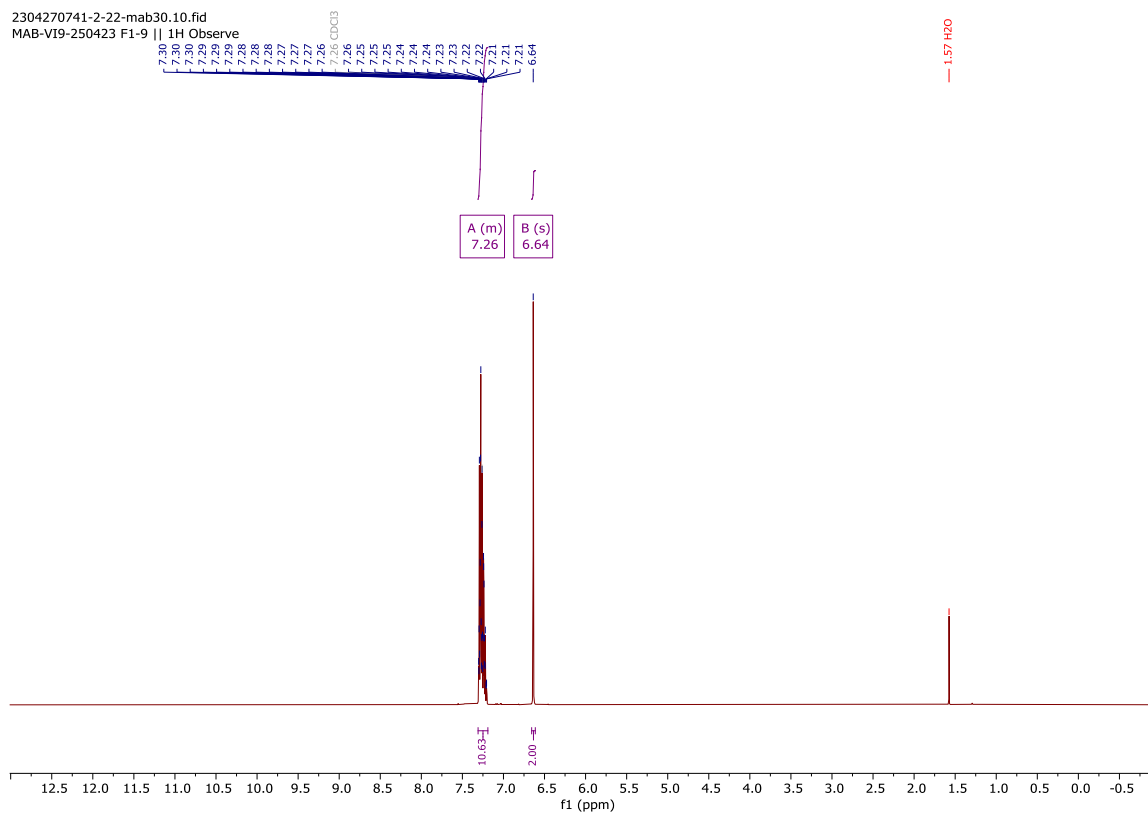
2   S. Kim, J. Rojas-Martin and F. D. Toste, *Chem. Sci.*, 2016, **7**, 85–88.

3   D. Vasu, A. L. Fuentes de Arriba, J. A. Leitch, A. De Gombert and D. J. Dixon, *Chem. Sci.*, 2019, **10**, 3401–3407.

4   C. Minozzi, A. Caron, J. C. Grenier-Petel, J. Santandrea and S. K. Collins, *Angew. Chemie Int. Ed.*, 2018, **57**, 5477–5481.

5   M. K. Etherington, N. A. Kukhta, H. F. Higginbotham, A. Danos, A. N. Bismillah, D. R. Graves, P. R. McGonigal, N. Haase, A. Morherr, A. S. Batsanov, C. Pflumm, V. Bhalla, M. R. Bryce and A. P. Monkman, *J. Phys. Chem. C*, 2019, **123**, 11109–11117.

6   M. Y. Wong, S. Krotkus, G. Copley, W. Li, C. Murawski, D. Hall, G. J. Hedley, M. Jaricot, D. B. Cordes, A. M. Z. Slawin, Y. Olivier, D. Beljonne, L. Muccioli, M. Moral, M. C. Gather, I. D. W. Samuel and E. Zysman-colman, *ACS Appl. Mater. Interfaces*, 2018, **10**, 33360–33372.

7   M. A. Bryden, F. Millward, T. Matulaitis, D. Chen, M. Villa, A. Fermi, S. Cetin, P. Ceroni and E. Zysman-Colman, *J. Org. Chem.*, 2023, **88**, 6364–6373.

8   N. K. Katakam, C. W. Seifert, J. D'Auria and G. Li, *Heterocycles*, 2019, **99**, 604–613.

9   N. G. Connelly and W. E. Geiger, *Chem. Rev.*, 1996, **96**, 877–910.

10   V. V. Pavlishchuk and A. W. Addison, *Inorganica Chim. Acta*, 2000, **298**, 97–102.

11   R. Bauernschmitt and R. Ahlrichs, *Chem. Phys. Lett.*, 1996, **256**, 454–464.

12   C. Adamo and V. Barone, *J. Chem. Phys.*, 1999, **110**, 6158–6170.

13   S. Grimme, S. Ehrlich and L. Goerigk, *J. Comput. Chem.*, 2011, **32**, 1456–1465.

14   M. J. Frisch, J. A. Pople and J. S. Binkley, *J. Chem. Phys.*, 1984, **80**, 3265–3269.

15   R. Ditchfield, W. J. Hehre and J. A. Pople, *J. Chem. Phys.*, 1971, **54**, 720–723.

16   W. J. Hehre, K. Ditchfield and J. A. Pople, *J. Chem. Phys.*, 1972, **56**, 2257–2261.

17   A. D. Becke, *J. Chem. Phys.*, 1993, **98**, 5648–5652.

18   W. J. Stevens, M. Krauss, H. Basch and P. G. Jasien, *Can. J. Chem.* , 1992, **70**, 612–630.

19   D. Feller, *J. Comput. Chem.*, 1996, **17**, 1571–1586.

20   B. P. Pritchard, D. Altarawy, B. Didier, T. D. Gibson and T. L. Windus, *J. Chem. Inf. Model.*, 2019, **59**, 4814–4820.

21   K. L. Schuchardt, B. T. Didier, T. Elsethagen, L. Sun, V. Gurumoorthi, J. Chase, J. Li and T. L. Windus, *J. Chem. Inf. Model.*, 2007, **47**, 1045–1052.

22   T. Clark, J. Chandrasekhar, G. W. Spitznagel and P. V. R. Schleyer, *J. Comput. Chem.*, 1983, **4**, 294–301.

23   F. Trani, G. Scalmani, G. Zheng, I. Carnimeo, M. J. Frisch and V. Barone, *J. Chem. Theory Comput.*, 2011, **7**, 3304–3313.

24   S. Miertus and J. Tomasi, *Chem. Physic*, 1982, **65**, 239–245.

25   S. Miertus, E. Scrocco and J. Tomasi, *Chem. Phys.*, 1981, **55**, 117–129.

26   J. L. Pascual-ahuir, E. Silla and I. Tuñon, *J. Comput. Chem.*, 1994, **15**, 1127–1138.

27   M. Caricato, B. Mennucci, J. Tomasi, F. Ingrosso, R. Cammi, S. Corni and G. Scalmani, *J. Chem. Phys.*, 2006, **124**, 124520.

28   M. J. Frisch, G. W. Trucks, H. B. Schlegel, G. E. Scuseria, M. A. Robb, J. R. Cheeseman, G. Scalmani, V. Barone, G. A. Peterssom, H. Nakatsuji, X. Li, M. Caricato, A. V Marenich, J. Bloino, B. G. Janesko, R. Gomperts, B. Mennucci, H. P. Hratchian, J. V Ortiz, A. F. Izmaylov, J. L. Sonnenberg, D. Williams-Young, F.

Ding, F. Lipparini, F. Egidi, J. Goings, B. Peng, A. Petrone, T. Henderson, D. Ranasinghe, V. G. Zakrzewski, J. Gao, N. Rega, G. Zheng, W. Liang, M. Hada, M. Ehara, K. Toyota, R. Fukuda, J. Hasegawa, M. Ishida, T. Nakajima, Y. Honda, O. Kitao, H. Nakai, T. Vreven, K. Throssell, J. A. Montgomery Jr, J. E. Peralta, F. Ogliaro, M. J. Bearpark, J. J. Heyd, E. N. Brothers, K. N. Kudin, V. N. Staroverov, T. A. Keith, R. Kobayashi, J. Normand, K. Raghavachari, A. P. Rendell, J. C. Burant, S. S. Iyengar, J. Tomasi, M. Cossi, J. M. Millam, M. Klene, C. Adamo, R. Cammi, J. W. Ochterski, R. L. Martin, K. Morokuma, O. Farkas, J. B. Foresman and D. J. Fox, 2019.

29   N. M. O'Boyle, A. L. Tenderholt and K. M. Langner, *J. Comput. Chem.*, 2008, **29**, 839–845.

30   W. Humphrey, A. Dalke and K. Schulten, *J. Mol. Graph.*, 1996, **14**, 33–38.

31   J. E. Stone, University of Missouri-Rolla, 1998.

32   J. D. Hunter, *Comput. Sci. Eng.*, 2007, **9**, 90–95.

33   N. M. O'Boyle, C. Morley and G. R. Hutchison, *Chem. Cent. J.*, , DOI:10.1186/1752-153X-2-5.

34   N. M. O'Boyle, M. Banck, C. A. James, C. Morley, T. Vandermeersch and G. R. Hutchison, *J. Cheminform.*, 2011, **3**, 239–245.

35   W. R. Browne, N. M. O. Boyle, J. J. Mc Garvey and J. G. Vos, *Chem. Soc. Rev.*, 2005, **34**, 641–663.

36   S. Lenoid, 2005–2020.

37   R. Dennington, T. A. Keith and J. M. Millam, 2009.

38   A. Juris and V. Balzani, *Helv. Chim. Acta*, 1981, **64**, 2175–2182.

39   M. S. Lowry, J. I. Goldsmith, J. D. Slinker, R. Rohl, R. A. Pascal, G. G. Malliaras and S. Bernhard, *Chem. Mater.*, 2005, **17**, 5712–5719.

40 Y. Zhang, M. Heberle, M. Wächtler, M. Karnahl and B. Dietzek, *RSC Adv.*, 2016, **6**, 105801–105805.

41 D. P. Hari and B. Ko, *Chem. Commun.*, 2014, **50**, 6688–6699.

42 E. Speckmeier, T. G. Fischer and K. Zeitler, *J. Am. Chem. Soc.*, 2018, **140**, 15353–15365.

43 J. Luo and J. Zhang, *ACS Catal.*, 2016, **6**, 873–877.

44 R. M. O'Donnell, P. G. Johansson, M. Abrahamsson and G. J. Meyer, *Inorg. Chem.*, 2013, **52**, 6839–6848.

45 R. Ishimatsu, S. Matsunami, T. Kasahara, J. Mizuno, T. Edura, C. Adachi, K. Nakano and T. Imato, *Angew. Chemie Int. Ed.*, 2014, **53**, 6993–6996.

46 S. Ladouceur, D. Fortin and E. Zysman-Colman, *Inorg. Chem.*, 2011, **50**, 11514–11526.

47 E. M. Arbeloa, C. M. Previtali and S. G. Bertolotti, *ChemPhysChem*, 2018, **19**, 934–942.

48 X. Zhang, I. Zhang and L. Liu, *Photochem. Photobiol.*, 2010, **86**, 492–498.

49 R. Ishimatsu, S. Matsunami, K. Shizu, C. Adachi, K. Nakano and T. Imato, *J. Phys. Chem. A*, 2013, **117**, 5607–5612.

50 J. Sosoe, C. Cruché, É. Morin and S. K. Collins, *Can. J. Chem.*, 2020, **98**, 461–465.

51 S. Grotjahn and B. König, *Org Lett*, 2021, **23**, 3146–3150.

52 A. Hossain, S. Engl, E. Lutsker and O. Reiser, *ACS Catal.*, 2019, **9**, 1103–1109.

53 C. Belger, N. M. Neisius and B. Plietker, *Chem. Eur. J.*, 2010, **16**, 12214–12220.